

Journal Pre-proof

Data-driven approach to learning optimal forms of constitutive relations in models describing Lithium plating in battery cells

Avesta Ahmadi, Kevin J. Sanders, Gillian R. Goward, Bartosz Protas



PII: S0098-1354(25)00256-X

DOI: <https://doi.org/10.1016/j.compchemeng.2025.109252>

Reference: CACE 109252

To appear in: *Computers and Chemical Engineering*

Received date: 11 January 2025

Revised date: 17 June 2025

Accepted date: 18 June 2025

Please cite this article as: A. Ahmadi, K.J. Sanders, G.R. Goward et al., Data-driven approach to learning optimal forms of constitutive relations in models describing Lithium plating in battery cells. *Computers and Chemical Engineering* (2025), doi: <https://doi.org/10.1016/j.compchemeng.2025.109252>.

This is a PDF file of an article that has undergone enhancements after acceptance, such as the addition of a cover page and metadata, and formatting for readability, but it is not yet the definitive version of record. This version will undergo additional copyediting, typesetting and review before it is published in its final form, but we are providing this version to give early visibility of the article. Please note that, during the production process, errors may be discovered which could affect the content, and all legal disclaimers that apply to the journal pertain.

© 2025 Published by Elsevier Ltd.

Highlights:

- Lithium plating as a primary degradation mechanism in Li-ion cells.
- Physical modeling and data-driven model calibration.
- Inverse modeling and adjoint-based gradient descent technique.
- Asymptotic reduction to simplify the DFN model.
- Optimal reconstruction of constitutive relations as function of two state variables.

Data-Driven Approach to Learning Optimal Forms of Constitutive Relations in Models Describing Lithium Plating in Battery Cells

Avesta Ahmadi^a, Kevin J. Sanders^b, Gillian R. Goward^b, Bartosz Protas^{c,*}

^aSchool of Computational Science & Engineering, McMaster University, Hamilton, L8S 4K1, Ontario, Canada

^bDepartment of Chemistry & Chemical Biology, McMaster University, Hamilton, L8S 4M1, Ontario, Canada

^cDepartment of Mathematics & Statistics, McMaster University, Hamilton, L8S 4K1, Ontario, Canada

Abstract

In this study we construct a data-driven model describing Lithium plating in a battery cell, which is a key process contributing to degradation of such cells. Starting from the fundamental Doyle-Fuller-Newman (DFN) model, we use asymptotic reduction and spatial averaging techniques to derive a simplified representation to track the temporal evolution of two key concentrations in the system, namely, the total intercalated Lithium on the negative electrode particles and total plated Lithium. This model depends on an a priori unknown constitutive relation representing the plating dynamics of the cell as a function of the state variables. An optimal form of this constitutive relation is then deduced from experimental measurements of the time-dependent concentrations of different Lithium phases acquired through Nuclear Magnetic Resonance spectroscopy. This is done by solving an inverse problem in which this constitutive relation is found subject to minimum assumptions as a minimizer of a suitable constrained optimization problem where the discrepancy between the model predictions and experimental data is minimized. This optimization problem is solved using a state-of-the-art adjoint-based technique. In contrast to some of the earlier approaches to modeling Lithium plating, the proposed model is able to predict non-trivial evolution of the concentrations in the relaxation regime when no current is applied to the cell. When equipped with an optimal constitutive relation, the model provides accurate predictions of the time evolution of both intercalated and plated Lithium across a wide range of charging/discharging rates. It can therefore serve as a useful tool for prediction and control of degradation mechanism in battery cells.

Keywords: Lithium Plating, Reaction Rates, Inverse Modeling, Constitutive Relations, Optimization

1. Introduction

In recent years, due to the growing demand for green energy and the phasing out of fossil fuels in pursuit of a more sustainable future, rechargeable batteries have assumed a prominent role in the transition to green technologies. Lithium-ion (Li-ion) batteries, among the most promising energy storage solutions, have found extensive applications in portable electronic devices, electric vehicles, and grid storage. With the increasing need for clean energy storage technologies, addressing

*Corresponding author

Email address: bprotas@mcmaster.ca (Bartosz Protas)

challenges related to the performance and reliability of Li-ion batteries has become crucial. To understand, analyze, mitigate, and control the impact of degradation mechanisms within a cell, sophisticated experimental and computational techniques are essential. Current research aims to contribute to the understanding and prediction of one of the primary degradation mechanisms in Li-ion batteries, commonly known as Lithium plating (Li-plating).

A Li-ion cell is composed of four components, the negative electrode (anode), the positive electrode (cathode), a porous separator, and a liquid electrolyte, with Li^+ ions being the main constituent of the cell. Intercalation of Li ions on the negative electrode solid phase during the charge process, and their subsequent deintercalation during the discharge process, are the desired mechanisms in the operation of the cell. However, these processes are typically impaired by various degradation mechanisms, such as Solid-Electrolyte Interphase (SEI) growth, Li-plating, and binder decomposition. These degradation mechanisms can result in three distinct degradation modes, namely, the loss of cycleable Lithium, loss of active materials, and loss of electrolyte, as noted in different studies ([Birkl et al., 2017](#); [Edge et al., 2021](#); [Lin et al., 2021](#)). A primary challenge associated with silicon anodes is their substantial volume change during charge/discharge cycles, a characteristic that enhances their energy density due to the presence of free sites for Lithium ions to intercalate. However, the continuous volume fluctuations might lead to the formation of secondary films on the anode surface, increasing the chance of Li-plating, and thereby depleting cycleable Lithium and contributing to the capacity fade of the cell over time.

Li-plating is a critical degradation mechanism that becomes more pronounced under harsh charging conditions ([Zhang et al., 2022](#)). It is accelerated when metallic Lithium forms during the charging process under conditions such as high charging rates, overcharging at high states-of-charge, and charging at low temperatures. These conditions introduce greater kinetic overpotential and higher diffusion rate of Li ions within the electrolyte than the rate of Li ions diffusing into the SEI layer, resulting in an excess of Lithium ions saturating on the anode surface ([Lin et al., 2021](#)). The Li-plating process can be either reversible or irreversible. The reverse process, known as Lithium stripping, occurs when metallic Lithium maintains electrical contact with the anode, allowing for the release of an electron and the deposition of Li ions back into the electrolyte. The irreversible Lithium, referred to as “dead Lithium”, can accumulate during fast charging ([Bugga and Smart, 2010](#)) and has the potential to rupture the separator due to the growth of Lithium dendrites ([Santhanagopalan et al., 2009](#)) or contribute to secondary SEI growth on its surface ([Fang et al., 2022](#)).

Quantifying plated Lithium in Li-ion batteries has been a long-standing challenge in battery studies, with the task of distinguishing between the SEI and metallic Lithium being especially complicated. Different experimental techniques could be used for the detection of metallic Lithium in the cell ([Lin et al., 2021](#); [Paul et al., 2021](#); [Tian et al., 2021](#)). In the current study, in order to better understand the Li-plating phenomena, we leverage experimental data obtained from a novel Li-NMR spectroscopy technique introduced and developed by [Sanders et al. \(2023\)](#). [Fang et al. \(2022\)](#) have also used a similar approach for quantification of metallic Lithium using the Li-NMR technique as an *operando* approach.

In an effort to quantify Lithium plating in the cell and eliminate the need for experimentation in an online application of cells or battery packs, we aim to model the growth and decay of plated Lithium using mathematical and computational tools. We seek to track the evolution of different phases of Lithium in operando under diverse charge/discharge protocols, and techniques of asymptotic analysis will first be used to develop simplified models based on the physical principles. Then,

state-of-the-art computational tools will be employed to calibrate these models, optimizing their alignment with experimental data. In particular, the technique of inverse modeling will be utilized for this purpose (Daniels et al., 2023; Escalante et al., 2020; Sethurajan et al., 2019, 2015), where optimal forms of electrochemical parameters and constitutive relations in the model are inferred from experimental data by solving suitable optimization problems. In relying on the calculus of variations, the proposed approach represents an alternative with respect to machine learning techniques which have recently gained popularity in estimating battery dynamics (Bhadiraju et al., 2023). Machine learning techniques often suffer from the lack of interpretability due to their reliance on black-box function approximation methods. Given that the primary objective of this research is to develop predictive models with physical interpretability, we choose to employ physics-based modeling approaches. Our model is calibrated using adjoint-based optimization techniques which generally yield point estimates. Alternatively, the Bayesian framework could in principle be used to infer probability distributions of the quantities of interest, thereby capturing their uncertainty. However, as discussed below, our model includes unknown constitutive relations, resulting in an infinite-dimensional inverse problem. This makes Bayesian approaches impractical for our purposes, given the difficulty in efficiently exploring high-dimensional parameter spaces. Therefore, the combination of physical modeling and adjoint-based optimization techniques represents the most appropriate methodology for our problem, balancing interpretability with computational efficiency. The resulting calibrated model holds promise for online applications, enabling real-time monitoring, recommending optimal charge/discharge protocols, and ultimately enhancing cell performance while mitigating degradation in the long run.

The paper is organized as follows: details of the experimental data are presented in Section 2; then in Section 3 we introduce the mathematical modeling framework for this problem and develop a dynamical system governing the evolution of lumped concentrations of different phases of Lithium in the cell; in Section 4 we introduce the inverse modeling framework and the computational tools used for calibrating the dynamical system; Section 5 presents the results of this analysis and compares them to the experimental data; finally, the summary of the work and the conclusions are deferred to Section 6. Some more technical material is collected in appendices.

2. Experimental Data

To calibrate the mathematical models for subsequent prediction and control, one requires experimental data tailored for this purpose. The experimental data utilized in this study was collected using the *operando* Li-NMR spectroscopy technique, as introduced in a prior publication by Sanders et al. (2023). This technique enables the identification and quantification of various Lithium phases within the anode while the cell is in operation, as depicted in Figure 1.

The anode material used for these experiments is silicon, recognized as one of the most promising materials due to its high energy density. The cathode material employed is NMC622 ($\text{LiNi}_{0.6}\text{Mn}_{0.2}\text{Co}_{0.2}\text{O}_2$). The test protocol of each experiment comprises a constant-current (CC) charge followed by constant-voltage (CV) discharge, and open-circuit resting (OCV) phases. The charge rates for the CC phase are C/3 (3-hour charge), C/2 (2-hour charge), 1C (1-hour charge), 2C (30-minute charge), and 3C (20-minute charge); the discharge rate for the CC phase remains constant at C/3 (3-hour discharge) for all cycles. Here, 'C' denotes the capacity of the cell. Note that, for simplicity of notation, the cycles C/3 and C/2 are hereafter denoted C3 and C2, respectively. The voltage of the cell ranges from 2.5V to 4.2V, with the lower value representing the full

discharge of the cell, while the higher value corresponds to the fully charged state. The OCV segment after charge and discharge is set for the duration of one hour. *Operando* NMR measurements were conducted at intervals of 5 minutes for the C3 cycle, 3 minutes for the C2 and 1C cycles, and 1.5 minutes for the 2C and 3C cycles. The evolution of various Lithium phases from Li-NMR experiments, alongside their operational current profile and the cell's terminal voltage, is depicted in Figure 1.

Several peaks are modeled when fitting NMR spectra to quantify different phases of Lithium, including

1. Lithium in the electrolyte or the SEI,
2. Lithium in dilute Li_xSi where $x < 2.0$ in a locally-ordered environment (referred to as dilute Li),
3. Lithium in concentrated Li_xSi where $x > 2.0$ in a locally-ordered environment (referred to as concentrated Li),
4. Li_xSi in a disordered environment (referred to as disordered Li), and
5. dendritic and plated Lithium.

These different phases of Lithium are manifested through distinct chemical shifts in the *operando* NMR data. It is worth noting that all dendritic Lithium formed is irreversible, while plated Lithium may exhibit reversible or irreversible behavior. As depicted in Figure 1, the evolution of different phases at constant rates demonstrates a nonlinear behavior during cell operation. Also, the dendritic Lithium content does not appear in all cycles, but only in the ones with higher C-rates. In other words, in the cycles with lower C-rates, the formation of dendritic Lithium is smaller than the sensitivity of the measurement device.

In order to preprocess the experimental data depicted in Figure 1 and format it for further analysis, the Lithium in the anode solid phase (dilute Li, concentrated Li, and disordered Li) is combined to form the solid phase with the concentration denoted $\tilde{C}_1(t)$. Similarly, addition of plated and dendritic Li content in the cell forms the Li phase corresponding to side reactions with the concentration $\tilde{C}_2(t)$. Note that the subscripts 1 and 2 refer to the intercalated Lithium and Lithium involved in side-reactions, respectively; a notation that is consistent with the mathematical model in Section 3.4. These concentrations are normalized and their evolution for each cycle are shown in Figure 2. As can be observed in Figure 1, the total Li content in the cell does not add up to a constant and is changing with the cell operation, due to several factors. First, the Li content in the positive electrode of the cell is not accounted for in the Li-NMR measurements. Second, the presence of noise in Li-NMR measurements is another source of deviation from the conservation of Lithium, cf. Section 3.2. It is also notable that two forms of dynamics are evident in the cell: the excitation dynamics and the relaxation dynamics. The excitation dynamics is the response of the system to an external current and is the dominant regime in the dynamics in the cell. The relaxation dynamics represents the evolution of the system while the cell is at rest in the absence of an external current. We note that the change in the dynamics due to excitation is larger than the change due to relaxation and this fact will be used in mathematical modeling, cf. Section 3.

The data for each experiment is split into three regimes: the charging regime, the OCV regime, and the discharge regime. We will use the following notation for the amalgamated data $\mathcal{D}_t = \bigoplus_i \mathcal{D}_i, i \in \{\text{C3}, \text{C2}, \text{1C}, \text{2C}, \text{3C}\}$, where \mathcal{D}_i refers to the total concentration data available for the cycle with rate i , and \bigoplus denotes the concatenation operator. Each cycle consists of three regimes: $\mathcal{D}_i = \bigoplus_j \mathcal{D}_i^j, j \in \{\text{ch}, \text{ocv}, \text{dch}\}$, where $\{\text{ch}, \text{ocv}, \text{dch}\}$ refer to charge, OCV, and discharge regimes of the cell testing protocols, respectively. Different segments of \mathcal{D}_t will be used for analysis.

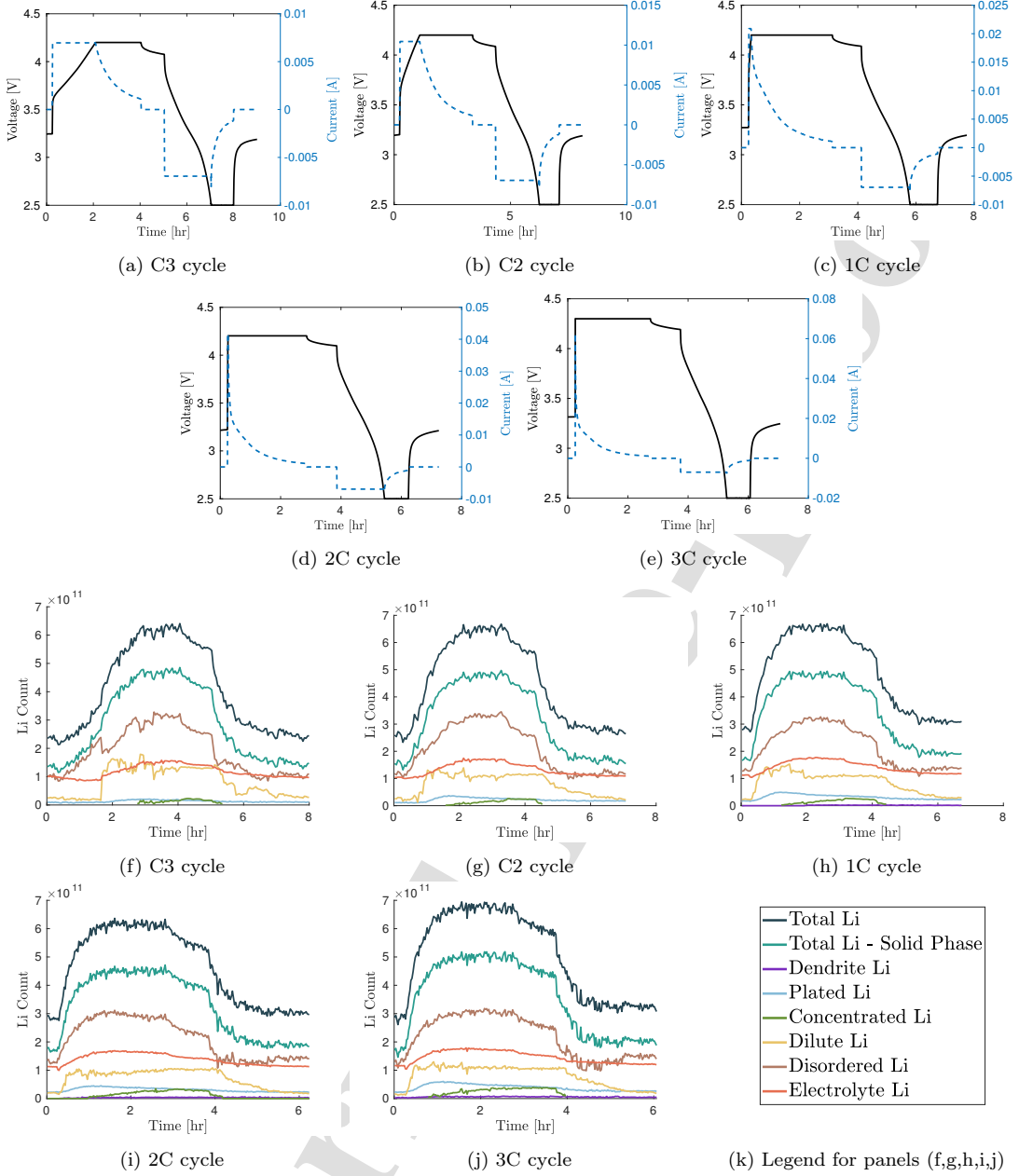


Figure 1: Terminal voltage and current applied to the cell (a,b,c,d,e), and evolution of the Li content in time in different phases obtained via the Li-NMR spectroscopy method (f,g,h,i,j) using different test protocols of the cell. Panel (k) is the legend for panels (f,g,h,i,j).

3. Physical Modeling

Mathematical modeling plays a pivotal role in comprehending the intricate physical processes taking place within a battery cell, exploring degradation mechanisms and their determining factors, and crafting effective mitigation and control strategies for the challenges encountered in large-scale

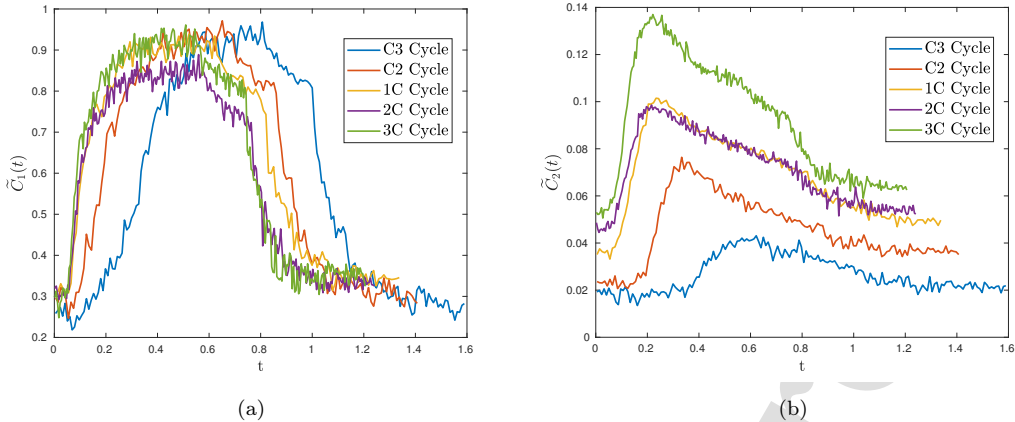


Figure 2: Evolution of Li content in time in the negative electrode solid phase corresponding to intercalated Li (a) and plated Li (b) for different C-rates. Note that the variables are normalized.

applications of Li-ion batteries. Various approaches can be employed for mathematical modeling, with two primary paradigms being physics-based modeling and data-driven machine learning. In this study, we aim to navigate the border between these two paradigms, with more emphasis placed on physics-based modeling of cells. This approach involves utilizing fundamental physical principles to construct a mathematical framework that represents the behavior of the cell and leveraging data-driven strategies for calibration. The ultimate objective is to predict the Li-plating dynamics of the cell using experimental data obtained from Li-NMR spectroscopy. The use of Li-NMR spectroscopy data in the modeling process highlights the integration of experimental data into the physics-based framework. This coupling of experimental observations with theoretical modeling can yield highly informative and predictive models for understanding and mitigating the critical issue of Li-plating in Li-ion batteries.

The operation of a Li-ion cell involves a multitude of physical and chemical processes occurring at different spatial and temporal scales. Multiscale models are used to connect the macroscale properties of the cell (cell voltage and current density) to its microscale properties (e.g. Lithium plating and dendrite growth) (Lee et al., 2021). One of the most widely accepted physics-based modeling approaches for Li-ion cells is rooted in the porous electrode theory initially introduced by Newman and Balsara (2021). In these models, the cell is treated as a continuous medium operating on larger temporal and spatial scales compared to discrete particle-level models that necessitate fine-scale resolution. Such continuum modeling relies on conservation laws for Lithium ions and counter-ions in the electrolyte, as well as the conservation of Lithium ions and electrons in the solid phase of the electrodes. The process of Lithium intercalation and deintercalation primarily takes place on the surface of the anode particles and is considered as an interfacial phenomenon. Solid-phase diffusion of Lithium ions within the anode can be modeled using linear diffusion equations, nonlinear diffusion equations (Escalante et al., 2020; O’Kane et al., 2022), or based on the Cahn-Hilliard theory of phase transition dynamics (Escalante et al., 2020; Guo et al., 2016). In the electrolyte, charge transport can be described using the dilute or concentrated electrolyte theories.

The review by Planella et al. (2022) explores various modeling approaches for Li-ion cells and introduces a systematic reductive framework, referred to as "asymptotic reduction", to simplify complex mathematical models using physical assumptions. The microscale and homogenized mod-

els require significant computational resources and are not well-suited for online estimation and control. They can be reduced to the well-known Doyle-Fuller-Newman (DFN) model (Fuller et al., 1994) by assuming a simpler geometry for all electrode particles. It simplifies the representation of electrode particles by assuming them to be spherical. Consequently, it solves the solid-state diffusion equations in the 1D radial coordinate, rather than attempting to capture the intricate 3D microstructure of the electrode particles. Similarly, the electrolyte equations are solved in a 1D planar geometry. This simplification results in a model that can be conceptually described as 1D+1D, hence it is also referred to as "pseudo-two-dimensional" (P2D). This model is renowned for its computational efficiency while retaining the capability to capture the internal dynamics and behavior of Li-ion cells. Aiming for enhanced computational efficiency, reduced-order models have been introduced as alternatives to the comprehensive DFN models. Two notable reduced-order models are the Single-Particle (SP) model, originally introduced by Atlung et al. (1979) and also referred to as SPM, and the Single-Particle Model with Electrolyte (SPMe), developed by Prada et al. (2012). The SPM and SPMe can be derived through asymptotic reductions of the DFN model (Marquis et al., 2019; Planella and Widanage, 2023; Richardson et al., 2020). The fundamental assumption is that the spherical electrode particles, as considered in the DFN model, are indistinguishable which allows these particles to be effectively represented by a single averaged or representative particle. Certain physical assumptions underlying these reduced models will affect their range of validity. According to Planella and Widanage (2023), the SP model is valid for small overpotentials and weak side reactions, and these two assumptions hold for low to moderate charge rates but will break down at high rates.

The objective of this research is to develop a simple model that can effectively capture the spatially-averaged dynamics of a Li-ion cell, and our approach is inspired by the SP model with side reactions (SPMe+SR) recently introduced by Planella and Widanage (2023); there are also close connections to a recent study by Sahu and Foster (2023). Taking the SPMe+SR model, which is a system of coupled partial differential equations (PDEs), as a starting point, we apply asymptotic reduction and averaging techniques to derive a suitable model in the form of a system of ordinary differential equations (ODEs) that describes the evolution of key space-averaged concentrations within the cell with certain parameters and functions calibrated using experimental data. In order to address certain limitations of the SPMe+SR model, some of the underlying assumptions have to be modified. We begin by introducing the DFN model in a dimensionless form in Section 3.1, then apply an asymptotic reduction in Section 3.2 before finally introducing our dynamical system in Section 3.4. Key differences between our model and those from earlier studies are highlighted in Section 3.3.

3.1. DFN Model

It is important to note that while the cathode component of the cell is initially considered, the final model (presented in Section 3.4) eliminates the need for solving for the positive electrode components, as the experimental data does not contain information from the positive electrode domain. In our model, only the Li-plating side reaction is taken into account and we disregard other side reactions in the cell (e.g., SEI growth). We also disregard the resistance of the film formed on the surface of the anode particle due to side reactions as well as the porosity change of the anode particles in time. Also, the volume change of anode particles (which could be significant in silicon anodes) is not explicitly considered, however, the concentration-dependent constitutive relations can implicitly take this effect into account, as described in Section 3.4.

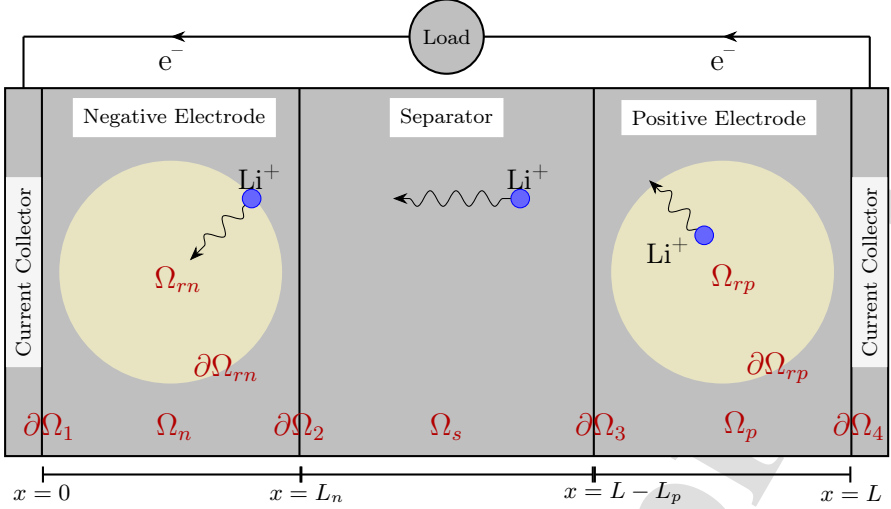


Figure 3: Schematic of a Li-ion cell in the charging state. Li ions deintercalate from the positive electrode surface, migrate toward the negative electrode through the electrolyte, and intercalate into negative particles. Electrons will migrate through the external circuit toward the negative electrode. Different parts of the domain of the model are marked in red.

The model domain consists of the negative electrode (Ω_n), the separator (Ω_s), and the positive electrode (Ω_p), where $\Omega = \Omega_n \cup \Omega_s \cup \Omega_p$. It is depicted in Figure 3, where the 1D macroscale coordinate is indicated on the horizontal axis with $\Omega_n = [0, L_n]$, $\Omega_s = [L_n, L - L_p]$ and $\Omega_p = [L - L_p, L]$, in which $L_n, L_p > 0$ are the widths of the negative electrode and positive electrode, respectively. In contrast, the microscale dimension is described using the spherical coordinates with $r \in \Omega_{rn} = [0, R_n]$ for the negative particle and $r \in \Omega_{rp} = [0, R_p]$ for the positive particle, where R_n and R_p represent the radii of the spherical negative and positive particles, respectively. Hereafter, symbols with a hat ($\hat{\cdot}$) are dimensionless variables, symbols in bold represent vector quantities whereas symbols with a bar ($\bar{\cdot}$) refer to quantities averaged over their spatial domain. The subscripts n , e , and p refer to the negative electrode solid phase, the electrolyte phase, and the positive electrode solid phase, respectively.

The DFN model is well established (Fuller et al., 1994) and a discussion of its different components is deferred to Appendix A. In order to facilitate asymptotic reduction, relations (A.1)–(A.7) are nondimensionalized using the dimensionless variables introduced in Appendix B, which yields

the following dimensionless system

$$\frac{\partial \hat{J}_n}{\partial \hat{x}} = -a_n L \hat{J}_{n,tot}, \quad \text{on } 0 \leq \hat{x} \leq l_n, \quad (1a)$$

$$\hat{J}_n = -\lambda \Xi_n \frac{\partial \hat{\phi}_n}{\partial \hat{x}}, \quad \text{on } 0 \leq \hat{x} \leq l_n, \quad (1b)$$

$$\mathcal{K}_n \frac{\partial \hat{C}_n}{\partial \hat{t}} = \frac{1}{\hat{r}^2} \frac{\partial}{\partial \hat{r}} \left(\hat{r}^2 \hat{D}_n \frac{\partial \hat{C}_n}{\partial \hat{r}} \right), \quad \text{on } 0 \leq \hat{r} \leq \hat{r}_n, \quad (1c)$$

$$\frac{\partial \hat{J}_p}{\partial \hat{x}} = -a_p L \hat{J}_{p,tot}, \quad \text{on } 1 - l_p \leq \hat{x} \leq 1, \quad (1d)$$

$$\hat{J}_p = -\lambda \Xi_p \frac{\partial \hat{\phi}_p}{\partial \hat{x}}, \quad \text{on } 1 - l_p \leq \hat{x} \leq 1, \quad (1e)$$

$$\mathcal{K}_p \frac{\partial \hat{C}_p}{\partial \hat{t}} = \frac{1}{\hat{r}^2} \frac{\partial}{\partial \hat{r}} \left(\hat{r}^2 \hat{D}_p \frac{\partial \hat{C}_p}{\partial \hat{r}} \right), \quad \text{on } 0 \leq \hat{r} \leq \hat{r}_p, \quad (1f)$$

$$\frac{\partial \hat{J}_e}{\partial \hat{x}} = a L \hat{J}_{tot}, \quad \text{on } 0 \leq \hat{x} \leq 1, \quad (1g)$$

$$\hat{J}_e = -\Xi_e \sigma_e B(x) \left[\frac{\partial \hat{\phi}_e}{\partial \hat{x}} - 2(1-t^+) \frac{\partial \log \hat{C}_e}{\partial \hat{x}} \right], \quad \text{on } 0 \leq \hat{x} \leq 1, \quad (1h)$$

$$\frac{\mathcal{K}_e}{\gamma_e} \frac{\partial(\epsilon \hat{C}_e)}{\partial t} = -\frac{1}{\gamma_e} \frac{\partial \hat{N}_e}{\partial \hat{x}} + a L \mathcal{K}_e \hat{J}_{tot}, \quad \text{on } 0 \leq \hat{x} \leq 1, \quad (1i)$$

$$\hat{N}_e = -\hat{D}_e B(x) \frac{\partial \hat{C}_e}{\partial \hat{x}} + t^+ \mathcal{K}_e \gamma_e \hat{J}_e, \quad \text{on } 0 \leq \hat{x} \leq 1, \quad (1j)$$

$$\hat{J}_{n,int} = \hat{j}_{int} [\exp(\alpha_{a,int} \hat{\eta}_{int}) - \exp(-\alpha_{c,int} \hat{\eta}_{int})], \quad (1k)$$

$$\hat{J}_{n,sr} = \hat{j}_{sr} [\exp(\alpha_{a,sr} \hat{\eta}_{sr}) - \exp(-\alpha_{c,sr} \hat{\eta}_{sr})], \quad (1l)$$

$$\hat{\eta}_{int} = \lambda [\hat{\phi}_n - \hat{U}_n] - \hat{\phi}_e, \quad \text{at } \hat{r} = \hat{r}_n, \quad (1m)$$

$$\hat{\eta}_{sr} = \lambda [\hat{\phi}_n - \hat{U}_{sr}] - \hat{\phi}_e, \quad \text{at } \hat{r} = \hat{r}_n, \quad (1n)$$

with the following dimensionless boundary and initial conditions

$$\frac{\partial \hat{C}_n}{\partial \hat{r}} = 0, \quad \text{at } \hat{r} = 0, \quad (2a)$$

$$-\hat{D}_n \frac{\partial \hat{C}_n}{\partial \hat{r}} = \mathcal{K}_n \gamma_n \hat{J}_{n,tot}, \quad \text{at } \hat{r} = \hat{r}_n, \quad (2b)$$

$$\frac{\partial \hat{C}_p}{\partial \hat{r}} = 0, \quad \text{at } \hat{r} = 0, \quad (2c)$$

$$-\hat{D}_p \frac{\partial \hat{C}_p}{\partial \hat{r}} = \mathcal{K}_p \gamma_p \hat{J}_{p,tot}, \quad \text{at } \hat{r} = \hat{r}_p, \quad (2d)$$

$$\hat{J}_n = \hat{J}_{app}, \quad \hat{J}_e = 0, \quad \hat{N}_e = 0, \quad \hat{\phi}_e = 0, \quad \text{at } \hat{x} = 0, \quad (2e)$$

$$\hat{J}_n = 0, \quad \hat{J}_e = \hat{J}_{app}, \quad \text{at } \hat{x} = l_n, \quad (2f)$$

$$\hat{J}_p = 0 \quad \hat{J}_e = \hat{J}_{app}, \quad \text{at } \hat{x} = l - l_p, \quad (2g)$$

$$\hat{J}_p = \hat{J}_{app}, \quad \hat{J}_e = 0, \quad \hat{N}_e = 0, \quad \hat{\phi}_e = 0, \quad \text{at } \hat{x} = l, \quad (2h)$$

$$\hat{C}_e = 1 \quad \hat{C}_n = \hat{C}_{n_i}, \quad \hat{C}_p = \hat{C}_{p_i}, \quad \text{at } \hat{t} = 0. \quad (2i)$$

Equations (1a), (1b), (1d) and (1e) represent the conservation of charge in the solid phase, whereas (1c) and (1f) represent the transport of Li ions in the solid phase. Equations (1g)–(1j) represent the conservation of charge in the electrolyte phase, and (1k)–(1n) represent the interfacial dynamics. In system (1)–(2), the variables are dimensionless, with ϕ representing the electrostatic potential in the solid phase, J the current density in different phases, J_{tot} the total current flux density at the solid-electrolyte interface due to intercalation and side reactions, J_{app} representing the current density applied to the cell, and C the Li concentration in the different phases. The definition and normalization of each variable is provided in [Appendix A](#) and [Appendix B](#). To simplify the notation in the analysis below, hereafter we opt to drop the hat sign from the dimensionless variables. In the next section, asymptotic reduction and averaging techniques will be used to reduce the full model (1)–(2) to a simpler space-independent ODE system, where the evolution of some key averaged concentrations are tracked.

3.2. Asymptotic Reduction and Averaging

In the current study the objective is to develop a simplified dynamical model in the form of the system of ODEs, capable of tracking the evolution of key concentrations in the cell. There are two important techniques used in this analysis that help in simplifying system (1)–(2). The first one is asymptotic reduction which assumes that a certain parameter in the system takes a limiting value (either large or small), and the dynamics of the system is investigated in the vicinity of that limiting value by expanding each dependent variable in a Taylor series with respect to that parameter. Asymptotic reduction of the DFN model to the SP model has been considered by various authors ([Marquis et al., 2019](#); [Planella and Widanage, 2023](#); [Richardson et al., 2020](#)), where different assumptions were employed in each case to reduce the DFN model to a SP model. [Marquis et al. \(2019\)](#) derives an asymptotic reduction of the DFN model to find a simplified SPM with electrolyte. This new model is shown to diverge from the DFN model for charging rates greater than 1C. [Richardson et al. \(2020\)](#) extends this work with a different assumption for performing the asymptotic reduction, to generate a simple SP model that can perform better under higher charging rates. [Planella and Widanage \(2023\)](#) extend this work to account for side reactions in the cell, a

study that inspired the current investigation. However, certain assumptions in our work are different from those invoked by Brosa Planella et al. Note that only the relevant equations in the system of equations (1) will be used in this analysis. In particular, electrolyte equations are not a matter of interest in this work and will not be used in this asymptotic analysis.

The second technique used in this analysis is the averaging of equations over their corresponding spatial domains in order to eliminate spatial dependency. Some quantities in the DFN model, e.g., concentrations, depend on both time and space (note that in the DFN model "space" means both the microscale variable r and the macroscale variable x), in contrast to our experimental data which is resolved only in time. Hence, averaging space-dependent quantities over their domains will eliminate the spatial dependency, and we will be left with a time-dependent model describing the evolution of lumped quantities. The aforementioned two techniques are used in conjunction. First, we start with the following assumptions needed for this analysis.

Assumptions.

- A1: The parameter λ is large enough so that the Taylor expansion of state variables in the vicinity of small λ^{-1} remains a valid approximation. Note that the parameter λ is defined as the ratio of the typical potential in the electrodes to the thermal voltage of the cell (see [Appendix B](#)). At room temperature the thermal voltage is approximately $25mV$, and represents the characteristic scale of the overpotential at the interface in the BV relation. When the scale of the potential in the electrode is large (in the order of magnitude of 1 Volt), the parameter λ remains large enough for the asymptotic analysis. This assumption refers to the physical case of small deviations from the equilibrium potential (small overpotentials), when the typical voltage in the electrodes is much larger than the thermal voltage. In this setting, the BV relations can be linearized.
- A2: The cathodic and anodic charge transfer coefficients for an interfacial reaction, cf. (1k)–(1l), are assumed to add up to one, namely, $\alpha_a + \alpha_c = 1$.
- A3: Side reactions in the cell are weak and in the order of λ^{-1} relative to the main intercalation/deintercalation reactions. This assumption allows us to capture the side reaction dynamics as corrections to the main reactions, as explained below.
- A4: The equilibrium potentials of the intercalation and side reactions are dependent on the concentration of the intercalated Lithium and of the Lithium participating in the side reactions, respectively. The sensitivity of these equilibrium potentials to changes in concentrations is small, thus, these nonlinear relationships can be linearized in the neighborhood of certain reference concentration values. Note that concentrations might exhibit large variations while the cell is in operation, however, if the sensitivity of the equilibrium potential to concentrations is small, this simplification remains valid.

A key assumption of the SP model states that all electrode particles behave the same, hence, one representative particle is sufficient to represent the microscale dynamics of the cell. This assumption will be re-derived as part of the asymptotic analysis.

Relaxation and Excitation Dynamics. Before delving into the asymptotic analysis of the DFN model, we discuss the fundamental sources of dynamics within the cell. Its primary driver is the excitation induced by the applied current. When the cell is brought to rest or an open-circuit

state after an excitation period (charge/discharge), the system continues to evolve until it reaches an equilibrium state corresponding to the specific state-of-charge of the cell. The intensity of this phenomenon varies across different chemistries (Ovejas and Cuadras, 2019). Consequently, we can distinguish two main regimes in the operation of the cell: excitation, representing the main process, and relaxation of the cell in the absence of an external influence; both will be captured by our mathematical model.

Expansion of Variables. In order to perform the asymptotic reduction, according to assumption A1, we expand each of the dependent variables in system (1)-(2) in the vicinity of $\lambda^{-1} \approx 0$. The expansion of variables in powers of λ^{-1} takes the form

$$\phi_n = \phi_{n,0} + \lambda^{-1}\phi_{n,1} + \dots,$$

where the subscripts 0 and 1 refer to the leading-order and first-order approximations, respectively. All other dependent variables in system (1)-(2) are expanded in a similar manner. These expansions are then substituted into this system to derive the leading-order and first-order approximations of the equations. Details of the different steps of the asymptotic reduction are presented in Appendix C.

Dynamical Model. Following the steps outlined in Appendix C, the time evolution of the two key averaged concentrations in the cell can be computed as

$$\begin{aligned} \frac{d\bar{C}_n}{dt} &= \frac{\gamma_n}{r_n} \left(\frac{J_{app}}{a_n L l_n} + \bar{J}_n^\ddagger - \lambda^{-1} \bar{J}_{sr} \right), \\ \frac{d\bar{C}_{sr,1}}{dt} &= \frac{\gamma_n}{r_n} \bar{J}_{sr}, \end{aligned} \quad (3)$$

where \bar{J}_n^\ddagger and \bar{J}_{sr} are obtained from (C.10) and (C.12), respectively, \bar{C}_n is the Li concentration in the negative electrode solid phase averaged over the domain, and $\bar{C}_{sr,1}$ is the first-order approximation of the concentration of Li involved in the side reactions averaged over the domain, J_{app} is the density of the current applied to the cell, \bar{J}_n^\ddagger represents the density of the intercalation current due to the relaxation dynamics on the anode surface averaged over the domain, and \bar{J}_{sr} represents the side reaction current density on the anode surface averaged over the domain. All other variables are introduced in Appendix A and Appendix B. Before moving on to the formulation of the inverse problem in Section 4, we need to prepare the ground by making the following comments about (3).

- As discussed in Appendix A.5, upon consideration of the relations governing the intercalation and plating current densities in the BV equation (A.8), it becomes apparent that these equations are both dependent on the concentrations of the intercalated Li and Li in side reactions, namely, $j_{sr,0} = j_{sr,0}(\bar{C}_n, \bar{C}_{sr})$ and $j_{int,0} = j_{int,0}(\bar{C}_n, \bar{C}_{sr})$, and the overpotential η . In our SP modeling framework, the need for solving for the potential profile and the overpotential is eliminated using equation (C.7). The dependence of the exchange current densities on concentrations is unknown, and needs to be determined using data-driven calibration strategies, cf. Section 4. As both exchange current densities are concentration dependent, we close the model by introducing the constitutive relation $\omega = \omega(\bar{C}_n, \bar{C}_{sr}) = \frac{j_{sr,0}}{j_{int,0}}$ describing the competition between the side reaction and intercalation exchange current densities. This relation controls how the total current density is split between side reaction and intercalation at each particular state of the cell.

- The concentrations C_n and C_{sr} introduced in the asymptotic analysis are expanded up to the first-order in λ^{-1} . Knowing that side reactions are not observed at the leading-order, $\bar{C}_{sr,0} = 0$, we conclude that $\bar{C}_{sr} = \bar{C}_{sr,1}$. The concentration of the intercalated Lithium can then be expressed as $\bar{C}_n = \bar{C}_{n,0} + \lambda^{-1}\bar{C}_{n,1}$. Note that when we expand \bar{C}_{sr} in (3), only the first-order approximation of concentration $\bar{C}_{n,1}$ appears in the expressions (with the leading term $\bar{C}_{n,0}$ absent). In this case we make the assumption that $\bar{C}_{n,1} = \zeta\bar{C}_n$ in order to close the mathematical model, where ζ is a scalar parameter, $0 < \zeta \ll 1$. We note that this assumption represents a simplification introduced to close the model as the parameter ζ could in reality be concentration-dependent.
- The exchange current density in the cell is defined as the interfacial current density while the cell is in an equilibrium state, for both the forward and the backward interfacial reactions. The symbol $j_{int,0}$ refers to the leading-order (assuming no side reactions) interfacial current density for Li intercalation or deintercalation on the negative particle surface at equilibrium. While the cell is in an equilibrium state, the dynamics is driven by two physical mechanisms acting at the electrode-electrolyte interface. The leading one is the Li intercalation/deintercalation at a specific rate ($j_{int,0}$). The second mechanism is the side reactions occurring at the interface and represented by the first-order correction terms. This mechanism can be regarded as the interaction between the intercalated Li and plated Li. In mathematical terms, $j_{int,1}$ represents the rate at which the intercalated Li is contributing to the growth of the plated Li phase, and vice versa, whereas $j_{sr,0}$ represents the rate at which the plated Li is contributing to the growth of intercalated Li. This interaction can be viewed as the forward/backward reactions between the two phases. As the local concentrations in each phase must remain stationary at equilibrium, we conclude that $j_{int,1} = j_{sr,0}$. We denote this exchange current density j_{sr} and remark that it is a function of the concentrations, $j_{sr} = j_{sr}(\bar{C}_n, \bar{C}_{sr})$.

Taking into account these considerations, and substituting (C.10) and (C.12) into the system of equations (3), we finally get

$$\begin{aligned} \frac{d\bar{C}_n}{dt} &= \underbrace{\frac{\gamma_n}{r_n a_n L l_n} [1 - \lambda^{-1}\omega] J_{app}}_{\text{Excitation Dynamics}} + \underbrace{\frac{\gamma_n}{r_n} j_{sr} [U_{sr,0} - U_{n,0}] - \frac{\gamma_n}{r_n} j_{sr} U'_n \bar{C}_n + \frac{\gamma_n}{r_n} \lambda^{-1} j_{sr} U'_{sr} \bar{C}_{sr}}_{\text{Relaxation Dynamics}}, \\ \frac{d\bar{C}_{sr}}{dt} &= \underbrace{\frac{\gamma_n}{r_n a_n L l_n} \omega J_{app}}_{\text{Excitation Dynamics}} + \underbrace{\frac{\gamma_n}{r_n} j_{sr} U'_n \zeta \bar{C}_n - \frac{\gamma_n}{r_n} j_{sr} U'_{sr} \bar{C}_{sr}}_{\text{Relaxation Dynamics}}, \end{aligned} \quad (4)$$

where $U_{sr,0}$ and $U_{n,0}$ are scalar reference potentials. The first term on the right-hand-side of each equation represents the excitation dynamics of the cell. The remaining terms are linear in concentrations and represent the relaxation dynamics of the cell. Thus, this simplified model is capable of accounting for both regimes. This concludes the derivation of the ODE model.

3.3. Comparison to the SPMe+SR Model

The presented modeling framework is inspired by the SPMe+SR model of Planella and Widanage (2023). However, certain assumptions in our approach differ from their work to better suit our specific configuration, particularly, as regards tracking time-dependent concentrations without spatial resolution. Inspection of the SPMe+SR model reveals that it has the following limitations.

1. A one-sided BV relation is used for modeling plating in the cell, with one exponential term in the corresponding expression. As the exponential term is always positive, the current density of Li plating at the solid-electrolyte interface is always negative. This implies that the model is only capable of predicting Li plating (and not stripping). As noted by [Sahu and Foster \(2023\)](#), a two-sided BV relation must be used to account for both plating and stripping in the cell. In our framework, we have used a two-sided BV relation in (1) to prevent this issue.
2. Once averaged over the spatial domain, the model fails to take into account the relaxation dynamics for the positive electrode, as evidenced by Equations (23)-(25) by [Planella and Widanage \(2023\)](#), and its dynamics is solely driven by excitation.
3. On the negative electrode the terms corresponding to relaxation dynamics of plated Li and intercalated Li possess opposite signs (once the cell is set to rest), meaning that intercalated Li phase and plated Li phase will converge to an equilibrium state in different directions. If Li in the intercalated phase becomes intercalated (deintercalated) in the relaxation regime, the Li in plated phase gets stripped (plated). This contradicts the evidence from experimental data, cf. Section 2, showing that the deintercalation process is accompanied by the stripping process in the relaxation regime.

These inconsistencies in the SPMe+SR model stem from two key factors, namely,

1. The one-sided BV relation prevents the model from predicting Li stripping, as discussed earlier. The solution to this issue is to use a two-sided BV relation as in (1).
2. The relaxation dynamics of the SPMe+SR model is not consistent with the dynamics of the cell due to the underlying assumptions of the asymptotic reduction framework by [Planella and Widanage \(2023\)](#).

In order to address the second issue (the inconsistency in relaxation dynamics), we need to understand the source of this inconsistency in the SPMe+SR model. Referring to this model, if we assume there is no side reaction in the cell, the interfacial current density for the side reaction becomes zero, and hence, the intercalated Li dynamics will only be driven by excitation. In other words, the relaxation dynamics of Li in negative electrode particles is only accounted for when a side reaction is present, and it is indeed in the reverse direction to the side reaction. In simpler terms, the relaxation dynamics of Li in the negative electrode is dependant on the side reaction dynamics and this dependence is also observed for the Li dynamics in the positive electrode (no side reaction on the positive electrode results in no relaxation dynamics for Li in the positive electrode). This dependence of the relaxation dynamics on the presence of a side reaction is the source of the inconsistency which arises due to the fact that the relaxation dynamics is not accounted for in the leading-order terms of the interfacial current density (recall that leading-order terms refer to vanishing side reaction, cf. Assumption A3). Specifically, [Planella and Widanage \(2023\)](#) assume that $\phi_{n,0} = U_n|_{C_{n,0}}$. Consequently, the second term on the right-hand side of Equation (C.6) vanishes, recovering the underlying assumption of the SP model that all particles exhibit uniform behavior in space (as $\phi_{n,0}$ is spatially uniform). Below we elucidate how this assumption leads to loss of relaxation dynamics at the leading order.

In our modeling framework, we decompose the intercalation process at the leading-order into two components, capturing both the excitation and relaxation dynamics of the cell. This formulation ensures that both dynamics are present in the space-averaged model, and that the relaxation dynamics is independent of the presence of side reactions in the cell. We highlight that failure to include relaxation dynamics terms would result in the space-averaged model to exhibit non-trivial

behavior only when a current is applied to the cell. To achieve that, we relax the assumption that $\phi_{n,0} = U_n|_{C_{n,0}}$, and introduce the relaxation dynamics as the second term on the right-hand side in (C.6). In order to recover the inherent assumption of the SP model regarding the uniformity of particles in space, we introduce the assumption $\phi_{n,0} = U_{sr}|_{C_{sr,0}}$, as detailed in (C.9). While one might argue that this assumption neglects the relaxation dynamics of the side reaction, it is important to consider the relative magnitudes of the plated Li concentrations compared to the intercalated Li concentrations. The relaxation dynamics is primarily driven by the intercalation process rather than by the side reaction. Consequently, this assumption remains valid and allows us to close the mathematical model. We also note that the aforementioned assumptions imply that the relaxation dynamics of Li in the negative electrode is driven by the difference between the equilibrium potentials of the intercalated Li and plated Li.

By comparing our model to the one introduced by Sahu and Foster (2023), we remark that they introduced a Heaviside step function in the definition of the Li plating dynamics with the intention to ensure that Li stripping process is stopped once the concentration of the plated Li becomes zero. Our mathematical model does not take this into account, however, it could be easily included to ensure proper operation of the model at all concentrations. As we will see in Section 5.2, the results of fitting the model to experimental data demonstrate the desired behavior, meaning no stripping occurs below zero concentration. Thus, in the interest of simplicity, we have decided not to include the Heaviside function in our model.

3.4. Linearizing Relaxation Dynamics

For simplicity, from now on, we will be using C_1 and C_2 to denote \bar{C}_n and \bar{C}_{sr} , respectively. Aggregating all constants, the ODE system (4) becomes

$$\begin{aligned}\frac{dC_1}{dt} &= \alpha [1 - \lambda^{-1}\omega(C_1, C_2)] J_{app} + \beta_1 j_{sr}(C_1, C_2) + \beta_2 j_{sr}(C_1, C_2)C_1 + \beta_3 \lambda^{-1} j_{sr}(C_1, C_2)C_2, \\ \frac{dC_2}{dt} &= \alpha\omega(C_1, C_2)J_{app} + \beta_4 j_{sr}(C_1, C_2)C_1 - \beta_3 j_{sr}(C_1, C_2)C_2,\end{aligned}\quad (5)$$

where $j_{sr} = j_{sr}(C_1, C_2)$, $\omega = \omega(C_1, C_2)$, $\alpha \in \mathbb{R}$, and $\beta_i \in \mathbb{R}$, $i = 1, \dots, 4$. As discussed in Section 4, the system of equations (5) has several unknown parameters (five scalar quantities and two functions) complicated to study. Also, both the relaxation and the excitation dynamics components of the mathematical model are nonlinear, adding to the complexity of the inverse problem. As they both depend on the exchange current densities, one would need to solve the inverse problem by matching the model output against the experimental data for the entire charge/discharge cycle, fitting all unknown parameters and constitutive relation simultaneously. The resulting infinite-dimensional optimization problem would be therefore very difficult to solve. One simplifying assumption can break this problem down into two simpler sub-problems. When the cell is excited, specifically through high charge/discharge rates, the contribution of the excitation dynamics is much larger than the relaxation dynamics portion. Thus, the problem can be segmented into two parts as follows: (i) first solve the inverse problem for the relaxation dynamics when the excitation is zero (eliminating the excitation part from the equations), and then (ii) solve the inverse problem for the full model when the cell is excited (with the relaxation part calibrated in step (i)). This formulation will break the inverse problem into two separate sub-problems, each involving a smaller number of unknown parameters, hence decreasing the overall computational complexity. However, this approach has one caveat, namely, the part representing the relaxation dynamics is also a function of the exchange current density (which in turn is a function of concentration). Calibrating the

relaxation dynamics first requires finding an optimal form of the constitutive relation $j_{sr}(C_1, C_2)$, which will then be used for the excitation dynamics. However, we know that the excitation dynamics plays a dominant role in determining the behavior of the system, and hence, the constitutive relation needs to be determined from the excitation dynamics. This brings us to another simplifying observation, namely, when the cell is not excited, changes in concentrations are assumed small in comparison to when the cell is excited. This means that the concentrations will exhibit small changes with respect to some reference state, and accordingly, the change in the exchange current density j_{sr} is also negligible. Therefore, the second assumption is to linearize the relaxation dynamics part around a reference state of the cell. We thus define $C_1 = \widehat{C}_1 + C'_1$, $C_2 = \widehat{C}_2 + C'_2$, and linearize the constitutive relation as $j_{sr} \approx \widehat{j}_{sr}(\widehat{C}_1, \widehat{C}_2) + \frac{\partial j_{sr}}{\partial C_1} \Big|_{\widehat{C}_1} (C_1 - \widehat{C}_1) + \frac{\partial j_{sr}}{\partial C_2} \Big|_{\widehat{C}_2} (C_2 - \widehat{C}_2)$. Note that \widehat{C}_1 and \widehat{C}_2 denote a reference state of concentrations and deviations C'_1 and C'_2 from this reference state are small. We substitute these equations into the relaxation portion of equation (5), aggregate all constants and after eliminating high-order terms, we get

$$\begin{aligned} \frac{dC_1}{dt} &= \beta_1 + \beta_2 C_1 + \lambda^{-1} \beta_3 C_2, \\ \frac{dC_2}{dt} &= \beta_4 C_1 - \beta_3 C_2, \end{aligned} \quad (6)$$

for the relaxation dynamics of the cell (the constants are again β_i , $i = 1, 2, 3, 4$, however, their values are different than before). Therefore, with this linearization, the full model takes the form (in vector notation)

$$\begin{aligned} \frac{d}{dt} \mathbf{C}(t) &= \mathbf{AC}(t) + \mathbf{B} + \mathbf{F}(J_{app}(t)), \\ \mathbf{C}(t) &= \begin{bmatrix} C_1(t) \\ C_2(t) \end{bmatrix}, \quad \mathbf{B} = \begin{bmatrix} \beta_1 \\ 0 \end{bmatrix}, \quad \mathbf{A} = \begin{bmatrix} \beta_2 & \lambda^{-1} \beta_3 \\ \beta_4 & -\beta_3 \end{bmatrix}, \quad \mathbf{F} = \begin{bmatrix} \alpha [1 - \lambda^{-1} \omega] J_{app} \\ \alpha \omega J_{app} \end{bmatrix}, \\ \mathbf{C}(0) &= \mathbf{C}_0, \end{aligned} \quad (7)$$

where $\boldsymbol{\beta} = [\beta_1, \beta_2, \beta_3, \beta_4] \in \mathbb{R}^4$ are the parameters of the relaxation dynamics, and $\omega = \omega(C_1, C_2)$ and $\alpha \in \mathbb{R}$ are the unknown parameters and functions for the excitation dynamics of the cell. There are five scalar parameters and one constitutive relation given in terms of a function of two variables to be determined using inverse modeling. It is notable that the concentrations of different Li phases obtained from NMR spectroscopy experiments do not have a physical unit due to the nature of this methodology and the complexities of the computational post-processing of its data. Hence, it is impossible to directly match the concentrations of the physical model i.e., $C_1(t)$ and $C_2(t)$, to the Li content obtained from NMR spectroscopy. The inverse modeling approach will thus need to be designed so as to account for the conversion between the physical variables in the model and the quantities measured in the experiments.

4. Inverse modeling

The system of equations in (7) is not closed due to the dependence of ω on the state variables, which is unknown. To address this challenge, one can explore the relationship between ω and the two state variables C_1 and C_2 through data-driven calibration techniques with the function $\omega(C_1, C_2)$ determined through either a parametric or a non-parametric approach. In the parametric approach, the functional form describing the dependence of ω on the state variables is assumed

and its parameters are calibrated using data. Conversely, in the non-parametric approach, this relationship can be inferred without explicitly assuming any functional form describing how the constitutive relation ω depends on the state variables. The only assumptions imposed on the constitutive relation are the regularity of the function $\omega(C_1, C_2)$ and its behavior at the boundaries of the domain. The latter technique is superior, as it removes the assumptions about the underlying functional form of the constitutive relation. We thus focus here on the latter approach.

The inverse problem will be defined as follows: given a set of time-dependent measurements of the state variables, $\tilde{C}_1(t)$ and $\tilde{C}_2(t)$, within the time window $t \in [0, T]$, cf. Figure 2, we seek to reconstruct the constitutive relation $\omega = \omega(C_1, C_2)$ such that the solution to the ODE system (7) will best fit the experimental measurements. Note that in this formulation, no *a priori* assumption regarding the functional form of the constitutive relation is made other than its regularity and behavior for limiting values of the state variables. The dynamics of the system is split into two parts: (i) the relaxation dynamics and (ii) the excitation dynamics. In Section 4.1 we present the formulation of the inverse problem for the relaxation dynamics with details deferred to Appendix D due to their similarity to the approach used for the excitation dynamics presented in full in Section 4.2. Finally, in Section 4.3 a more robust framework is introduced for the inverse problem.

4.1. Relaxation Dynamics

In this section, we aim to calibrate model (7) for the relaxation dynamics only. When the cell is set to rest, the applied current is zero, and the excitation term $\mathbf{F}(J_{app}(t))$ on the right-hand-side of the model vanishes. Hence, the problem reduces to finding β and one can formulate a suitable inverse problem to calibrate each of the parameters in β using the cell data by minimizing a cost functional $\mathcal{J}_1 : \mathbb{R}^4 \rightarrow \mathbb{R}$ defined as

$$\begin{aligned} \mathcal{J}_1(\beta) &= \frac{1}{2} \int_0^T \left\| \mathbf{W} \mathbf{r}(t; \beta) \right\|_2^2 dt, \quad \text{where} \\ \mathbf{r}(t; \beta) &= \mathbf{C}(t; \beta) - \tilde{\mathbf{C}}(t), \quad \mathbf{C}(t; \beta) = \begin{bmatrix} C_1(t; \beta) \\ C_2(t; \beta) \end{bmatrix}, \quad \tilde{\mathbf{C}}(t) = \begin{bmatrix} \tilde{C}_1(t) \\ \tilde{C}_2(t) \end{bmatrix}, \quad \mathbf{W} = \begin{bmatrix} 1 & 0 \\ 0 & \sqrt{w} \end{bmatrix}, \end{aligned} \quad (8)$$

in which \mathbf{W} is a weight matrix, T is the final time of the cycle, $\|\cdot\|_2$ represents the Euclidean norm, and the dependence of the state variables (C_1 and C_2) on the parameters β is governed by Eq. (7). As the typical magnitudes of the two state variables differ by one order of magnitude, the weight matrix \mathbf{W} is designed to introduce a suitable normalization. Optimal parameter values $\bar{\beta}$ can be found by solving the minimization problem

$$\bar{\beta} = \arg \min_{\beta \in \mathbb{R}^4} \mathcal{J}_1(\beta). \quad (9)$$

For the purpose of solving this problem, a gradient-based optimization approach can be used, defined by the iterative procedure (Nocedal and Wright, 2002)

$$\begin{aligned} \beta^{(n+1)} &= \beta^{(n)} - \tau^{(n)} \nabla_{\beta} \mathcal{J}_1(\beta^{(n)}), \quad n = 1, 2, \dots, \\ \nabla_{\beta} \mathcal{J}_1(\beta^{(n)}) &= \left[\frac{\partial}{\partial \beta_1} \mathcal{J}_1(\beta^{(n)}) \quad \frac{\partial}{\partial \beta_2} \mathcal{J}_1(\beta^{(n)}) \quad \frac{\partial}{\partial \beta_3} \mathcal{J}_1(\beta^{(n)}) \quad \frac{\partial}{\partial \beta_4} \mathcal{J}_1(\beta^{(n)}) \right], \end{aligned} \quad (10)$$

where n refers to the iteration number, $\tau^{(n)}$ is the step length along the descent direction at each iteration, and $\nabla_{\beta} \mathcal{J}_1(\beta)$ the gradient of the cost functional (8) with respect to the vector of the

unknown parameters. Following the steps presented in [Appendix D](#), it is obtained as

$$\nabla_{\beta} \mathcal{J}_1 = \left[-\int_0^T \mathbf{C}^{*\top} \mathbf{I}_0 dt \quad -\int_0^T \mathbf{C}^{*\top} \mathbf{I}_2 \tilde{\mathbf{C}} dt \quad -\int_0^T \mathbf{C}^{*\top} \mathbf{I}_3 \tilde{\mathbf{C}} dt \quad -\int_0^T \mathbf{C}^{*\top} \mathbf{I}_4 \tilde{\mathbf{C}} dt \right]. \quad (11)$$

Now that the gradient is computed, we can use the iterative scheme [\(10\)](#) to minimize the cost functional to find the optimal parameter values $\bar{\beta}$. The computational framework is summarized as Stage I in Algorithm [1](#). When solving problem [\(9\)](#), we use the part of each cycle corresponding to the relaxation dynamics as data $\tilde{\mathbf{C}}(t)$, cf. [\(8\)](#).

4.2. Excitation Dynamics

In this section, we assume that the optimal parameter values of the linear dynamics corresponding relaxation dynamics are determined and given in $\bar{\beta}$. What is left to calibrate is the nonlinear excitation dynamics consisting of the constitutive relation $\omega(C_1, C_2)$ (representing the competition between intercalation and plating), and the scalar parameter α . Before introducing the optimization framework, we need to define two intervals on which the state variables are defined:

- $\mathcal{I} := \left[C_1, C_2 \in \mathbb{R} \mid C_1 \in [C_1^\alpha, C_1^\beta], C_2 \in [C_2^\alpha, C_2^\beta] \right]$ is referred to as the "identifiability interval", which is the region of state space spanned by the solution of Eq. [\(7\)](#); note that this interval is a function of iterations in Algorithm [1](#),
- $\mathcal{L} := \left[C_1, C_2 \in \mathbb{R} \mid C_1 \in [C_1^a, C_1^b], C_2 \in [C_2^a, C_2^b] \right]$, where $C_1^a \leq C_1^\alpha, C_1^b \geq C_1^\beta, C_2^a \leq C_2^\alpha$ and $C_2^b \geq C_2^\beta$; this will be the interval we seek to reconstruct the constitutive relation on, which is generally larger than the identifiability region, i.e., $\mathcal{I} \subseteq \mathcal{L}$; the aim is to reconstruct the constitutive relation on this larger interval than the one spanned by the solution of the ODE system in order to make it possible to reconstruct the constitutive relation on a fixed domain.

Note that the function ω depends on *two* state variables which, as will be evident below, makes it significantly more complicated than the analogous problems considered by [Bukshynov and Protas \(2013\)](#); [Bukshynov et al. \(2011\)](#); [Protas et al. \(2014\)](#); [Sethurajan et al. \(2015\)](#) where the constitutive relation was a function of one state variable only. Hence, to simplify the present problem, we will assume that the constitutive relation depending on two state variables has a separable form, i.e.,

$$\omega(C_1, C_2) = \omega_1(C_1) \cdot \omega_2(C_2). \quad (12)$$

Consequently, one can reconstruct each of these factors separately, and then merge the results using [\(12\)](#). The functions $\omega_1(C_1)$ and $\omega_2(C_2)$, and the parameter α need to be inferred from data by solving a suitable inverse problem to minimize the mismatch between the experimental measurements and the predictions of the model [\(7\)](#) by defining the cost functional $\mathcal{J}_2 : \mathbb{R} \times \mathcal{X} \times \mathcal{X} \rightarrow \mathbb{R}$ as

$$\begin{aligned} \mathcal{J}_2(\alpha, \omega_1, \omega_2) &= \frac{1}{2} \int_0^T \left\| \mathbf{W} \mathbf{r}(t; \alpha, \omega_1, \omega_2) \right\|_2^2 dt, \\ \mathbf{r}(t; \alpha, \omega_1, \omega_2) &= \mathbf{C}(t; \alpha, \omega_1, \omega_2) - \tilde{\mathbf{C}}(t), \quad \mathbf{C}(t; \alpha, \omega_1, \omega_2) = \begin{bmatrix} C_1(t; \alpha, \omega_1, \omega_2) \\ C_2(t; \alpha, \omega_1, \omega_2) \end{bmatrix}, \end{aligned} \quad (13)$$

where the dependence of the state variables (C_1 and C_2) on the constitutive relation ω is governed by system [\(7\)](#) and \mathcal{X} denotes a suitable Hilbert function space ω_1 and ω_2 belong to. The optimal

reconstructions of the constitutive relations are obtained by solving the minimization problem

$$[\bar{\omega}_1, \bar{\omega}_2, \bar{\alpha}] = \arg \min_{\omega_1 \in \mathcal{X}, \omega_2 \in \mathcal{X}, \alpha \in \mathbb{R}} \mathcal{J}_2(\alpha, \omega_1, \omega_2). \quad (14)$$

We claim that this formulation is in fact very general since there are no assumptions on the form of the functions $\omega_1(C_1)$ and $\omega_2(C_2)$. In particular, these functions are sought as elements of the Hilbert space \mathcal{X} and as such are not subject to any a priori ansatz. The only assumptions we will make concern the regularity (smoothness) of these functions, which will be encoded in a suitable definition of the space \mathcal{X} , and their behavior for limiting values of the arguments C_1 and C_2 . These assumptions are "minimal", in the sense that they do not presuppose any particular "physics" and are only needed to make model (7) mathematically well defined.

Since the cost functional $\mathcal{J}_2(\alpha, \omega_1, \omega_2)$ is a function of two constitutive relations and a parameter, gradient-based solution of problem (14) is facilitated by decoupling optimization with respect to each of these quantities into a separate subproblem in which the remaining two quantities are held fixed, i.e.,

$$\begin{aligned} \omega_1^{(n+1)} &= \omega_1^{(n)} - \tau_1^{(n)} \nabla_{\omega_1}^{\mathcal{X}} \mathcal{J}_2(\alpha^{(n)}, \omega_1^{(n)}, \omega_2^{(n)}), \\ \omega_2^{(n+1)} &= \omega_2^{(n)} - \tau_2^{(n)} \nabla_{\omega_2}^{\mathcal{X}} \mathcal{J}_2(\alpha^{(n)}, \omega_1^{(n+1)}, \omega_2^{(n)}) \quad n = 1, 2, \dots, \\ \alpha^{(n+1)} &= \alpha^{(n)} - \tau_3^{(n)} \frac{\partial}{\partial \alpha} \mathcal{J}_2(\alpha^{(n)}, \omega_1^{(n+1)}, \omega_2^{(n+1)}), \end{aligned} \quad (15)$$

where $\tau_i^{(n)}, i \in \{1, 2, 3\}$, refers to the step length along the descent direction at iteration n , $\nabla_{\omega_1}^{\mathcal{X}} \mathcal{J}_2(\alpha, \omega_1, \omega_2)$ and $\nabla_{\omega_2}^{\mathcal{X}} \mathcal{J}_2(\alpha, \omega_1, \omega_2)$ represent the gradients of cost functional with respect to each of the two factors ω_1 and ω_2 , and $\frac{\partial}{\partial \alpha} \mathcal{J}_2(\alpha, \omega_1, \omega_2)$ is the partial derivative of the cost functional with respect to the unknown parameter α . Note that relation (15) represents the steepest-descent optimization algorithm, however, in practice, one can use more sophisticated techniques such as the conjugate-gradients method. The Polak-Ribiere conjugate-gradient formulation has been used for this study. In all cases, the key ingredient of the optimization algorithm (15) are the gradients of the cost functional with respect to the constitutive relation.

Note that the constitutive relation $\omega(C_1, C_2)$ is assumed to be a continuous function of the state variables over \mathcal{L} , hence the gradients $\nabla_{\omega_1}^{\mathcal{X}} \mathcal{J}_2(\alpha, \omega_1, \omega_2)$ and $\nabla_{\omega_2}^{\mathcal{X}} \mathcal{J}_2(\alpha, \omega_1, \omega_2)$ are infinite-dimensional sensitivities of the cost functional to perturbations of the factors ω_1 and ω_2 . In order to compute these gradients in a convenient manner, adjoint sensitivity analysis is leveraged (Bukshynov and Protas, 2013; Bukshynov et al., 2011; Protas et al., 2014). Application of such techniques to the reconstruction of constitutive relations in electrochemistry is also discussed by Sethurajan et al. (2015). In order to ensure the continuity of the constitutive relation with respect to C_1 and C_2 , one needs to reconstruct each of the factors $\omega_1(C_1)$ and $\omega_2(C_2)$ in (12) as an element of the Sobolev space $H^1(\mathcal{L})$ of functions with square-integrable (weak) derivatives. Thus, the gradient needs to be obtained with respect to the corresponding inner product. However, to simplify the derivation, we will first obtain the gradient in the space $\mathcal{X}(\mathcal{I}) = L^2(\mathcal{I})$ of square-integrable functions and will then use it to find the required Sobolev gradient. The following derivation focuses on the gradient of the cost functional with respect to ω_1 , $\nabla_{\omega_1}^{\mathcal{X}} \mathcal{J}_2(\alpha, \omega_1, \omega_2)$, with the derivation of the expressions for $\nabla_{\omega_2}^{\mathcal{X}} \mathcal{J}_2(\alpha, \omega_1, \omega_2)$ and for $\frac{\partial}{\partial \alpha} \mathcal{J}_2(\alpha, \omega_1, \omega_2)$ following a similar process.

We begin by computing the Gateaux (directional) derivative with respect to perturbations of

ω_1 as

$$\begin{aligned}\mathcal{J}'_2(\alpha, \omega_1, \omega_2; \omega'_1) &= \lim_{\epsilon \rightarrow 0} \epsilon^{-1} [\mathcal{J}_2(\alpha, \omega_1 + \epsilon \omega'_1, \omega_2) - \mathcal{J}_2(\alpha, \omega_1, \omega_2)] \\ &= \int_0^T (\mathbf{w} \mathbf{r}(t; \alpha, \omega_1, \omega_2))^\top \mathbf{C}'(\alpha, \omega_1, \omega_2; \omega'_1) dt, \\ \mathbf{C}'(\alpha, \omega_1, \omega_2; \omega'_1) &= \begin{bmatrix} C'_1(\alpha, \omega_1, \omega_2; \omega'_1) \\ C'_2(\alpha, \omega_1, \omega_2; \omega'_1) \end{bmatrix},\end{aligned}\quad (16)$$

where $\mathbf{C}'(\alpha, \omega_1, \omega_2; \omega'_1)$ is a solution of the system of perturbation equations. In order to obtain this system, the state variables are perturbed with respect to ω_1 as

$$\mathbf{C}(\alpha, \omega_1, \omega_2) = \widehat{\mathbf{C}}(\widehat{\alpha}, \widehat{\omega}_1, \widehat{\omega}_2) + \epsilon [\mathbf{C}'(\alpha, \omega_1, \omega_2; \omega'_1)] + \mathcal{O}(\epsilon^2). \quad (17)$$

The constitutive relations are perturbed with respect to ω_1 as (with the arguments dropped for brevity)

$$\begin{aligned}\omega_1 &= \widehat{\omega}_1 + \epsilon \left[\omega'_1 + \frac{d\omega_1}{dC_1} C'_1 \right] + \mathcal{O}(\epsilon^2), \\ \omega_2 &= \widehat{\omega}_2 + \epsilon \left[\frac{d\omega_2}{dC_2} C'_2 \right] + \mathcal{O}(\epsilon^2).\end{aligned}\quad (18)$$

Note that a perturbation of one constitutive relation will affect both concentrations as C_1 and C_2 are not decoupled. The corresponding perturbation of the constitutive relation then takes the form

$$\omega = \widehat{\omega}_1 \widehat{\omega}_2 + \epsilon \left[\widehat{\omega}_2 \omega'_1 + \widehat{\omega}_2 \frac{d\omega_1}{dC_1} C'_1 + \widehat{\omega}_1 \frac{d\omega_2}{dC_2} C'_2 \right] + \mathcal{O}(\epsilon^2). \quad (19)$$

Substituting (17) and (19) into (7), and collecting terms proportional to ϵ , we arrive at the system of perturbation equations corresponding to ω'_1

$$\frac{d}{dt} \mathbf{C}'(t) = \mathbf{A} \mathbf{C}'(t) + \mathbf{D} \mathbf{C}'(t) + \widehat{\omega}_2 \widehat{\alpha} \boldsymbol{\rho} \omega'_1, \quad (20a)$$

$$\mathbf{C}'(0) = \mathbf{0}, \quad (20b)$$

$$\mathbf{D} = \begin{bmatrix} -\widehat{\alpha} \lambda^{-1} J_{app} \widehat{\omega}_2 \frac{d\omega_1}{dC_1} & -\widehat{\alpha} \lambda^{-1} J_{app} \widehat{\omega}_1 \frac{d\omega_2}{dC_2} \\ \widehat{\alpha} J_{app} \widehat{\omega}_2 \frac{d\omega_1}{dC_1} & \widehat{\alpha} J_{app} \widehat{\omega}_1 \frac{d\omega_2}{dC_2} \end{bmatrix}, \quad (20c)$$

$$\boldsymbol{\rho} = \begin{bmatrix} -\lambda^{-1} J_{app} \\ J_{app} \end{bmatrix}. \quad (20d)$$

Note that the first term on the right-hand-side of (20a) represents the relaxation dynamics, cf. (6), whereas the second and third terms correspond to the excitation dynamics. Following a similar procedure, the systems of perturbation equations corresponding to ω'_2 and α' are obtained (all sharing the same matrices \mathbf{A} and \mathbf{D}).

The gradient can be extracted from the directional derivative (16) of the cost functional by invoking the Riesz representation theorem (Luenberger, 1969)

$$\mathcal{J}'_2(\alpha, \omega_1, \omega_2; \omega'_1) = \langle \nabla_{\omega_1}^{\mathcal{X}} \mathcal{J}_2, \omega'_1 \rangle_{\mathcal{X}(\mathcal{L})} \quad (21)$$

and similarly for $\mathcal{J}'_2(\alpha, \omega_1, \omega_2; \omega'_2)$, where $\langle \cdot, \cdot \rangle_{\mathcal{X}(\mathcal{L})}$ represents the inner product in the Hilbert space $\mathcal{X}(\mathcal{L})$ of functions defined over the interval \mathcal{L} . In the case when differentiation is performed with

respect to the scalar parameter α , the Riesz representer reduces to the partial derivative in a finite-dimensional Euclidean space, namely, $\mathcal{J}'_2(\alpha, \omega_1, \omega_2; \alpha') = \frac{\partial \mathcal{J}_2}{\partial \alpha} \cdot \alpha'$. Assuming $\mathcal{X}(\mathcal{L}) = L^2(\mathcal{L})$, the directional derivative will be expressed in terms of the L^2 inner product as

$$\mathcal{J}'_2(\alpha, \omega_1, \omega_2; \omega'_1) = \int_{C_1^a}^{C_1^b} \nabla_{\omega_1}^{L^2} \mathcal{J}_2 \cdot \omega'_1 ds. \quad (22)$$

Note that the Gateaux derivative (16) is not consistent with the Riesz form (22), as the expression for the perturbation of the constitutive relation ω'_1 is hidden in equation (20) governing the perturbations of the state variables $C'_1(\alpha, \omega_1, \omega_2; \omega'_1)$ and $C'_2(\alpha, \omega_1, \omega_2; \omega'_1)$. In addition, the expression for the Gâteaux differential in (16) is defined in terms of an integral with respect to time, whereas the Riesz form (22) involves the state variable as the integration variable. In order to tackle the first issue (introducing an explicit dependence on the perturbations ω'_1 and ω'_2 in the Gateaux differential, as in (22)), we will employ adjoint analysis, in which a suitable adjoint problem is defined to transform (16) into the Riesz form (22). Whereas, to overcome the latter issue (inconsistency of the integration variable), a change of variables is used.

The behavior of the Sobolev gradients on the boundaries of the domain \mathcal{L} needs to be specified via suitable boundary conditions. Dictated by physical considerations, in the present problem, the homogeneous Neumann boundary condition is adopted which preserves the values of the derivatives of the functions $\omega_1(C_1)$ and $\omega_2(c_2)$ at the boundaries while allowing the gradient to modify their values at the boundary. Another possibility would be to impose homogeneous Dirichlet boundary conditions, which would preserve the values of $\omega_1(C_1)$ and $\omega_2(C_2)$ at the boundaries, but would make it possible to modify their derivatives.

We begin with the adjoint analysis. Multiplying (20) by the vector of adjoint variables $\mathbf{C}^*(t) = [C_1^*(t), C_2^*(t)]^\top$, and integrating in time, we obtain

$$\int_0^T \mathbf{C}^{*\top} \frac{d}{dt} \mathbf{C}' dt - \int_0^T \mathbf{C}^{*\top} \mathbf{A} \mathbf{C}' dt - \int_0^T \mathbf{C}^{*\top} \mathbf{D} \mathbf{C}' dt - \int_0^T \mathbf{C}^{*\top} \widehat{\omega}_2 \widehat{\alpha} \boldsymbol{\rho} \omega'_1 dt = 0. \quad (23)$$

Performing integration by parts for the first term and applying the initial conditions of the perturbation system (20), we get

$$-\mathbf{C}^{*\top}(T) \mathbf{C}'(T) + \int_0^T \frac{d}{dt} \mathbf{C}^{*\top} \mathbf{C}' dt + \int_0^T \mathbf{C}^{*\top} \mathbf{A} \mathbf{C}' dt + \int_0^T \mathbf{C}^{*\top} \mathbf{D} \mathbf{C}' dt + \int_0^T \mathbf{C}^{*\top} \widehat{\omega}_2 \widehat{\alpha} \boldsymbol{\rho} \omega'_1 dt = 0, \quad (24)$$

and then factoring out \mathbf{C}'

$$-\mathbf{C}^{*\top}(T) \mathbf{C}'(T) + \int_0^T \left[\frac{d}{dt} \mathbf{C}^{*\top} + \mathbf{C}^{*\top} \mathbf{A} + \mathbf{C}^{*\top} \mathbf{D} \right] \mathbf{C}' dt + \int_0^T \mathbf{C}^{*\top} \widehat{\omega}_2 \widehat{\alpha} \boldsymbol{\rho} \omega'_1 dt = 0. \quad (25)$$

We judiciously define the adjoint system as

$$\begin{aligned} \frac{d}{dt} \mathbf{C}^*(t) + \mathbf{A}^\top \mathbf{C}^*(t) + \mathbf{D}^\top \mathbf{C}^*(t) &= \mathbf{w} \mathbf{r}(t; \omega_1, \omega_2), \\ \mathbf{C}^*(T) &= \mathbf{0}. \end{aligned} \quad (26)$$

With this definition of the adjoint system, expression (25) becomes

$$\int_0^T (\mathbf{w} \mathbf{r})^\top \mathbf{C}' dt = - \int_0^T \mathbf{C}^{*\top} \widehat{\omega}_2 \widehat{\alpha} \boldsymbol{\rho} \omega'_1 dt, \quad (27)$$

and the directional derivative with respect to ω'_1

$$\mathcal{J}'_2(\alpha, \omega_1, \omega_2; \omega'_1) = - \int_0^T \widehat{\omega}_2 \widehat{\alpha} \mathbf{C}^{*\top} \boldsymbol{\rho} \omega'_1 dt \quad (28)$$

due to the choice of the source term in the adjoint system (26). Likewise, following analogous steps, the directional differentials with respect to ω'_2 and α' can be expressed as

$$\mathcal{J}'_2(\alpha, \omega_1, \omega_2; \omega'_2) = - \int_0^T \widehat{\omega}_1 \widehat{\alpha} \mathbf{C}^{*\top} \boldsymbol{\rho} \omega'_2 dt, \quad (29a)$$

$$\mathcal{J}'_2(\alpha, \omega_1, \omega_2; \alpha') = - \int_0^T \widehat{\omega}_1 \widehat{\omega}_2 \mathbf{C}^{*\top} \boldsymbol{\varrho} \alpha' dt, \quad (29b)$$

where

$$\boldsymbol{\varrho} = \begin{bmatrix} (\widehat{\omega}^{-1} - \lambda^{-1}) J_{app} \\ J_{app} \end{bmatrix}.$$

We note that the expressions for the Gâteaux differentials (28), (29a) and (29b) of the objective functional with respect to ω_1 , ω_2 and α are expressed in terms of solution of the same adjoint system (26), which is however post-processed in different ways.

Evidently, the Gateaux differentials (28), (29a) and (29b) are expressed in terms of perturbations of the constitutive relation, which is consistent with the Riesz form (22). However, the integration variable (time t) in these relations is different from the integration variable in the Riesz form (the state variable C_1 or C_2). To address this inconsistency, a change of variables must be used

$$dt = \frac{dC_1}{\beta_1 + \beta_2 C_1 + \lambda^{-1} \beta_3 C_2 + \widehat{\alpha}(1 - \lambda^{-1} \widehat{\omega}) J_{app}} = \frac{dC_2}{\beta_4 C_1 - \beta_3 C_2 + \widehat{\alpha} \widehat{\omega} J_{app}}, \quad (30)$$

which is obtained by a rearrangement of the governing equation (7) noting that the mapping from the time to the state variable, $t \mapsto \{C_1(t), C_2(t)\}, t \in [0, T]$, is uniquely defined. Moreover, the integral over the trajectory $\mathcal{K} := \{\cup_{t \in [0, T]} [C_1(t), C_2(t)]\}$ can be expressed as a definite integral over the interval \mathcal{L} , such that we obtain

$$\begin{aligned} \mathcal{J}'_2(\alpha, \omega_1, \omega_2; \omega'_1) &= - \int_{C_1^\alpha}^{C_1^\beta} \frac{\widehat{\omega}_2 \widehat{\alpha} \mathbf{C}^{*\top} \boldsymbol{\rho}}{\beta_1 + \beta_2 C_1 + \lambda^{-1} \beta_3 C_2 + \widehat{\alpha}(1 - \lambda^{-1} \widehat{\omega}) J_{app}} \omega'_1 ds, \\ \mathcal{J}'_2(\alpha, \omega_1, \omega_2; \omega'_2) &= - \int_{C_2^\alpha}^{C_2^\beta} \frac{\widehat{\omega}_1 \widehat{\alpha} \mathbf{C}^{*\top} \boldsymbol{\rho}}{\beta_4 C_1 - \beta_3 C_2 + \widehat{\alpha} \widehat{\omega} J_{app}} \omega'_2 ds, \\ \mathcal{J}'_2(\alpha, \omega_1, \omega_2; \alpha') &= \left[- \int_0^T \widehat{\omega}_1 \widehat{\omega}_2 \mathbf{C}^{*\top} \boldsymbol{\varrho} dt \right] \cdot \alpha', \end{aligned} \quad (31)$$

where we note that α' is independent of time and can be pulled out of the integral. Hence, the L^2 gradients and the partial derivative with respect to α are given by

$$\begin{aligned} \nabla_{\omega_1}^{L^2} \mathcal{J}_2 &= - \frac{\widehat{\omega}_2 \widehat{\alpha} \mathbf{C}^{*\top} \boldsymbol{\rho}}{\beta_1 + \beta_2 C_1 + \lambda^{-1} \beta_3 C_2 + \widehat{\alpha}(1 - \lambda^{-1} \widehat{\omega}) J_{app}}, \\ \nabla_{\omega_2}^{L^2} \mathcal{J}_2 &= - \frac{\widehat{\omega}_1 \widehat{\alpha} \mathbf{C}^{*\top} \boldsymbol{\rho}}{\beta_4 C_1 - \beta_3 C_2 + \widehat{\alpha} \widehat{\omega} J_{app}}, \\ \frac{\partial \mathcal{J}_2}{\partial \alpha} &= - \int_0^T \widehat{\omega}_1 \widehat{\omega}_2 \mathbf{C}^{*\top} \boldsymbol{\varrho} dt. \end{aligned} \quad (32)$$

As already noted in earlier studies (Bukshtynov and Protas, 2013; Bukshtynov et al., 2011; Protas et al., 2014), the L^2 gradients are not a suitable choice for reconstruction of constitutive relations as they are generally discontinuous and are undefined outside the identifiability region \mathcal{I} . Thus, to ensure their minimum regularity and that constitutive relations are well-defined over the domain \mathcal{L} , we will employ Sobolev gradients to reconstruct both factors ω_1 and ω_2 in (15). Since the constitutive relation in the governing system (7) depends on their product (12), an optimization formulation in which these two factors are determined independently as in (14) is underdetermined, because the mean of the product $\omega_1 \cdot \omega_2$ can be changed by the mean value of each of the factors, which can lead to numerical complications. We will therefore amend the formulation such that the mean value of one of the factors is fixed (without the loss of generality, we will assume $\int_{C_2^a}^{C_2^b} \omega_2(s) ds = 0$) leaving the factor $\omega_1(C_1)$ to capture the mean value of the entire constitutive relation (12). We will thus use two Sobolev spaces: $\mathcal{X} = H^1(\mathcal{L})$ and $\mathcal{X} = H_0^1(\mathcal{L})$, where the subscript 0 means the function space consists of zero-mean functions. They are both endowed with the inner product

$$\langle z_1, z_2 \rangle_{H^1} = \int_{C_1^a}^{C_1^b} \left(z_1 z_2 + l^2 \frac{dz_1}{ds} \frac{dz_2}{ds} \right) ds, \quad \forall z_1, z_2 \in H^1(\mathcal{L}) \quad (33)$$

in which $0 < l < \infty$ is a "length-scale" parameter controlling the degree of smoothness of the gradients. Clearly, setting $l = 0$ recovers the L^2 inner product, cf. (22).

Invoking the Riesz theorem (Luenberger, 1969), we obtain

$$\mathcal{J}'_2(\alpha, \omega_1, \omega_2; \omega'_1) = \left\langle \nabla_{\omega_1}^{L^2} \mathcal{J}_2, \omega'_1 \right\rangle_{L^2(\mathcal{L})} = \left\langle \nabla_{\omega_1}^{H^1} \mathcal{J}_2, \omega'_1 \right\rangle_{H^1(\mathcal{L})} \quad (34)$$

and after performing integration by parts with respect to s , we arrive at

$$\int_{C_1^a}^{C_1^b} \nabla_{\omega_1}^{L^2} \mathcal{J}_2 \cdot \omega'_1 ds = \int_{C_1^a}^{C_1^b} \left(\nabla_{\omega_1}^{H^1} \mathcal{J}_2 \cdot \omega'_1 - l^2 \frac{d^2 \nabla_{\omega_1}^{H^1} \mathcal{J}_2}{ds^2} \omega'_1 \right) ds + \frac{d \nabla_{\omega_1}^{H^1} \mathcal{J}_2}{ds} \omega'_1 \Big|_{C_1^a}^{C_1^b}. \quad (35)$$

Noting that the perturbation ω'_1 is arbitrary and imposing the Neumann boundary conditions on the Sobolev gradient at the endpoints $s = C_1^a, C_1^b$, we obtain the following inhomogeneous elliptic boundary-value problems defining the smoothed H^1 Sobolev gradient based on the L^2 gradient

$$\begin{aligned} \nabla_{\omega_1}^{H^1} \mathcal{J}_2 - l^2 \frac{d^2 \nabla_{\omega_1}^{H^1} \mathcal{J}_2}{ds^2} &= \nabla_{\omega_1}^{L^2} \mathcal{J}_2, & \text{for } s \in (C_1^a, C_1^b), \\ \frac{d \nabla_{\omega_1}^{H^1} \mathcal{J}_2}{ds} &= 0, & \text{at } s = C_1^a, C_1^b. \end{aligned} \quad (36)$$

As regards extraction of the gradient $\nabla_{\omega_2}^{H^1} \mathcal{J}_2$, for which we have $\int_{C_2^a}^{C_2^b} \nabla_{\omega_2}^{H^1} \mathcal{J}_2(s) ds = 0$, we proceed by identifying $\mathcal{J}'_2(\alpha, \omega_1, \omega_2; \omega'_2)$ with an expression analogous to (34), but with $\nabla_{\omega_2}^{H^1} \mathcal{J}_2$ replaced with $\mathbb{P}_0 \nabla_{\omega_2}^{H_0^1} \mathcal{J}_2$ where the operator $\mathbb{P}_0 : H^1 \rightarrow H_0^1$ represents the orthogonal, with respect to the inner product (33), projection onto the subspace of zero-mean functions defined as $\mathbb{P}_0 u = u - \bar{u}$, where $\bar{u} = \frac{1}{C_2^b - C_2^a} \int_{C_2^a}^{C_2^b} u(s) ds$. Following analogous steps as above, cf. (35), we arrive at the

boundary-value problem below defining the zero-mean Sobolev gradient $\nabla_{\omega_2}^{H^1} \mathcal{J}_2$

$$\begin{aligned} \nabla_{\omega_2}^{H_0^1} \mathcal{J}_2 - \frac{1}{C_2^b - C_2^a} \int_{C_2^a}^{C_2^b} \nabla_{\omega_2}^{H_0^1} \mathcal{J}_2 \, ds - l^2 \frac{d^2 \nabla_{\omega_2}^{H_0^1} \mathcal{J}_2}{ds^2} &= \nabla_{\omega_2}^{L^2} \mathcal{J}_2, \quad \text{for } s \in (C_2^a, C_2^b), \\ \frac{d \nabla_{\omega_2}^{H_0^1} \mathcal{J}_2}{ds} &= 0, \quad \text{at } s = C_2^a, C_2^b. \end{aligned} \quad (37)$$

Thus, when used in iterations (15), the gradient $\nabla_{\omega_2}^{H^1} \mathcal{J}_2$ will not modify the mean value of $\omega_2(C_2)$.

The computational framework for the solution of optimization problems (10) and (15) is summarized in Algorithm 1. It is implemented in MATLAB with the ODE problems solved using the `ode45` routine with tolerances suitably adjusted to deal with the stiff nature of these problems.

Algorithm 1 Computational Framework for Optimal Reconstruction of Constitutive Relations

Inputs:

$\beta^{(0)}, \alpha^{(0)}, \omega_1^{(0)}, \omega_2^{(0)}$ — Initial guesses for parameters and constitutive relations
 N — Maximum iteration number
 TOL — Tolerance

Outputs:

$\bar{\beta}, \bar{\alpha}, \bar{\omega}(C_1, C_2)$ — Optimally constructed parameters and constitutive relations

Stage I: Optimal Reconstruction of β :

```

 $n \leftarrow 0$ 
set  $\beta^{(0)}$  as initial guess
repeat
    •  $n \leftarrow n + 1$ 
    • solve forward problem (7) based on prior estimation of  $\hat{\beta}$  to obtain  $C_1(t; \beta^{(n-1)})$  and  $C_2(t; \beta^{(n-1)})$ , assuming  $J_{app} = 0$ 
    • solve adjoint problem (D.7) to obtain  $C_1^*(t; \beta^{(n-1)})$  and  $C_2^*(t; \beta^{(n-1)})$ 
    • compute gradient of cost functional with respect to parameters,  $\nabla_{\beta} \mathcal{J}_1$  via (11)
    • determine step length  $\tau^{(n)}$  of optimization iterative scheme (10) via Brent's line search scheme as outlined by Press et al. (1986)
    • compute the updated parameters for  $\beta^{(n)}$  via (10) as the posterior estimation of  $\hat{\beta}$ 
until  $\frac{\mathcal{J}_1(\beta^{(n)})}{\mathcal{J}_1(\beta^{(n-1)})} < TOL$  or  $n > N$ 

```

Stage II: Optimal reconstruction of α, ω_1 and ω_2 :

```

 $n \leftarrow 0$ 
 $\beta \leftarrow \bar{\beta}$ 
set  $\alpha^{(0)}, \omega_1^{(0)}(C_1)$  and  $\omega_2^{(0)}(C_2)$  as initial guesses
repeat
    •  $n \leftarrow n + 1$ 
    • solve forward problem (7) to obtain  $C_1(t; \alpha^{(n-1)}, \omega_1^{(n-1)}, \omega_2^{(n-1)})$  and  $C_2(t; \alpha^{(n-1)}, \omega_1^{(n-1)}, \omega_2^{(n-1)})$ 
    • solve adjoint problem (26) to obtain  $C_1^*(t; \alpha^{(n-1)}, \omega_1^{(n-1)}, \omega_2^{(n-1)})$  and  $C_2^*(t; \alpha^{(n-1)}, \omega_1^{(n-1)}, \omega_2^{(n-1)})$ 
    • compute  $L^2$  gradients of cost functional with respect to constitutive relations,  $\nabla_{\omega_1}^{L^2} \mathcal{J}$  and  $\nabla_{\omega_2}^{L^2} \mathcal{J}$ , and  $\frac{\partial \mathcal{J}}{\partial \alpha}$  via (32)
    • solve the boundary-value problems (36) and (37) to obtain Sobolev gradients of cost functionals  $\nabla_{\omega_1}^{H^1} \mathcal{J}$  and  $\nabla_{\omega_2}^{H^1} \mathcal{J}$ 
    • determine step length  $\tau^{(n)}$  of optimization iterative scheme (15) via Brent's line search scheme as outlined by Press et al. (1986)
    • compute the updated relations for  $\alpha^{(n)}, \omega_1^{(n)}$  and  $\omega_2^{(n)}$  via (15)
until  $\frac{\mathcal{J}_2(\alpha^{(n)}, \omega_1^{(n)}, \omega_2^{(n)})}{\mathcal{J}_2(\alpha^{(n-1)}, \omega_1^{(n-1)}, \omega_2^{(n-1)})} < TOL$  or  $n > N$ 
Compute  $\bar{\omega}(C_1, C_2) = \bar{\omega}_1^{(n)} \cdot \bar{\omega}_2^{(n)}$ 

```

4.3. Formulation with Aggregated Data

The computational framework outlined in Algorithm 1 can be utilized to train models for both relaxation and excitation dynamics based on a single cycle of the cell. Each dataset $\mathcal{D}_i, i \in$

$\mathcal{C}, \mathcal{C} = \{\text{C3, C2, 1C, 2C, 3C}\}$, can be used to reconstruct the parameters and constitutive relations in the model. However, it is known that such an approach is usually not robust, since models tend to exhibit acceptable performance only over a limited range of cycles (C-rates) close to the cycle where they were calibrated, cf. Section 5.2. To enhance the robustness of the proposed framework, one can train the model on a wider range of C-rates using an ensemble of datasets corresponding to different C-rates, i.e., $\mathcal{D}_t = \bigoplus_i \mathcal{D}_i, i \in \mathcal{C}$. In this scenario, the cost functional is defined as a sum of expressions corresponding to each dataset for relaxation dynamics, namely, $\mathcal{J}_1(\boldsymbol{\beta}; \mathcal{D}_t^{ocv}) = \sum_{i \in \mathcal{C}} \mathcal{J}_1(\boldsymbol{\beta}; \mathcal{D}_i^{ocv})$, where $\mathcal{J}_1(\boldsymbol{\beta}; \mathcal{D}_i^{ocv})$ denotes the cost functional computed based on \mathcal{D}_i^{ocv} . The cost functional for the excitation dynamics will then be defined as $\mathcal{J}_2(\alpha, \omega_1, \omega_2; \mathcal{D}_t^j) = \sum_{i \in \mathcal{C}} \mathcal{J}_2(\alpha, \omega_1, \omega_2; \mathcal{D}_i^j)$, where $j \in \{ch, dch\}$. Since the cost functional gradients depend linearly on the data, the gradient of an aggregated cost functional is computed as a sum of the gradients of the cost functionals corresponding to each dataset \mathcal{D}_i . More precisely, for the relaxation dynamics, we have $\nabla_{\boldsymbol{\beta}} \mathcal{J}_1(\boldsymbol{\beta}; \mathcal{D}_t^{ocv}) = \sum_{i \in \mathcal{C}} \nabla_{\boldsymbol{\beta}} \mathcal{J}_1(\boldsymbol{\beta}; \mathcal{D}_i^{ocv})$, and for the excitation dynamics $\nabla_{\omega_1} \mathcal{J}_2(\alpha, \omega_1, \omega_2; \mathcal{D}_t^j) = \sum_{i \in \mathcal{C}} \nabla_{\omega_1} \mathcal{J}_2(\alpha, \omega_1, \omega_2; \mathcal{D}_i^j)$, where $j \in \{ch, dch\}$, and similarly for $\nabla_{\omega_2} \mathcal{J}_2(\alpha, \omega_1, \omega_2; \mathcal{D}_t^j)$ and $\frac{\partial}{\partial \alpha} \mathcal{J}_2(\alpha, \omega_1, \omega_2; \mathcal{D}_t^j)$. Other elements of Algorithm 1 remain unchanged.

5. Results

In this section, we first present the results for the relaxation dynamics obtained as outlined in Section 4.1. Once the parameters $\boldsymbol{\beta}$ of the relaxation dynamics are determined, we solve the inverse problem to compute the optimal forms of the constitutive relations and parameters for the excitation dynamics, namely, ω_1 , ω_2 and α , using the approach from Section 4.2. The computational framework is validated in Appendix E where a solution of an inverse problem with synthetic data is also presented.

5.1. Relaxation Dynamics

The computational framework outlined as Stage I of Algorithm 1 is used to find optimal parameter values of the relaxation dynamics of the cell. The parameters used to initialize the optimization algorithm are chosen as $\boldsymbol{\beta}^{(0)} = [-0.1, -0.1, -0.1, -0.1]$, $N = 500$, and $TOL = 10^{-6}$. The interval \mathcal{L} for the optimization framework is $(C_1, C_2) \in [-0.5, 1.5] \times [-0.2, 0.5]$ and this choice has been made based on the magnitude of the state variables in different cycles. Also, the optimization framework with aggregated data, cf. Section 4.3, has been used here with the training data $\mathcal{D}_t = \bigoplus_i \mathcal{D}_i, i \in \mathcal{C}$. The relative decay of the cost functional in the iterative scheme, cf. (8), is shown in Figure 4. As can be observed, the cost functional value is decaying significantly relative to its initial value, but the rate of decay slows at later iterations. The optimal solution is $\bar{\boldsymbol{\beta}} \approx [0.85, -1.85, 0.55, -0.02]$ such that the matrices in system (6) become

$$\mathbf{B} = \begin{bmatrix} 0.85 \\ 0 \end{bmatrix}, \quad \mathbf{A} = \begin{bmatrix} -1.85 & 0.003 \\ -0.02 & -0.55 \end{bmatrix}. \quad (38)$$

Note that matrix \mathbf{A} has two real negative eigenvalues as $\sigma(\mathbf{A}) = \{-1.85, -0.55\}$. This implies that the linear part of the system corresponding to the relaxation dynamics has the form of an exponential decay toward an equilibrium point, which is consistent with the behavior of the cell in the relaxation mode, cf. Figure 2. The results of predicting the evolution of concentrations for different cycles of the cell using the optimal parameter values $\bar{\boldsymbol{\beta}}$ are shown in Figure 5. As can be observed, the model performs relatively well on a wide range of C-rates. The optimal parameter

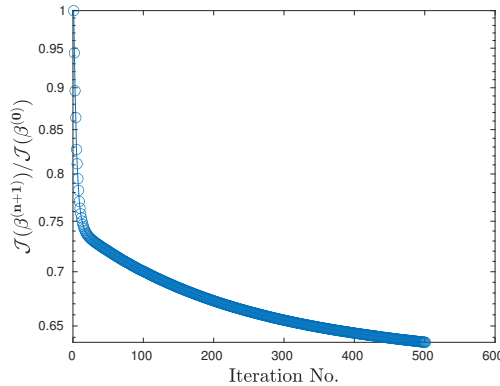


Figure 4: Cost functional history $\mathcal{J}(\boldsymbol{\beta})$ relative to its initial value as a function of iteration number.

values for the relaxation dynamics will be used when solving the optimization problem for excitation dynamics which is described next.

5.2. Excitation Dynamics

We begin by fitting the unknown constitutive relations and parameter in (7) describing the excitation dynamics to the data corresponding to individual cycles, namely, $\mathcal{D}_i^j, i \in \mathcal{C}, j \in \{ch, dch\}$. There are two different regimes, namely, charge and discharge, and a separate instance of inverse problem (14) is solved in each of them with the results compared. In order to initialize Stage II in Algorithm 1, the initial guesses for the constitutive relations dictated by our knowledge of the physics of the cell are $\omega_1^{(0)}(C_1) = 0.25, \omega_2^{(0)}(C_2) = 0.25, \alpha^{(0)} = 5$ such that the constitutive relation $\omega(C_1, C_2)$ (defining the competition between intercalation and plating) has a value closer to the bottom bracket of the interval $[0, 1]$ reflecting the dominating role of the intercalation process. As mentioned in Section 4.2, the function $\omega_1(C_1)$ is reconstructed in the space H^1 and the function $\omega_2(C_2)$ in H_0^1 such that its mean is fixed. Algorithm 1 is allowed to run for a maximum of $N = 30$ iterations and the smoothing parameter in the H^1 inner product (33) is $l = 1$. The interval \mathcal{L} is set as $(C_1, C_2) \in [-0.5, 1.5] \times [-0.2, 0.5]$, where the choice of relatively wide bounds for both state variables ensures that the effect of the somewhat arbitrary boundary conditions imposed on the Sobolev gradients, cf. (36)–(37), has little effect on the behavior of these gradients for the concentrations of interest. In other words, if the bounds on the interval \mathcal{L} were chosen too close to the bounds of the identifiability interval \mathcal{I} , the behavior of the function at the end points of the identifiability interval would be affected by the choice of these boundary conditions.

The results obtained by solving optimization problem (14) for the charge and discharge regimes of the 1C cycle are presented in Figure 6. As can be observed, the large-scale details of the measurement data $\tilde{C}_1(t)$ and $\tilde{C}_2(t)$ are well captured by the model equipped with the optimally reconstructed constitutive relations. The fine details in the data result from the noise in the NMR measurements, and hence it is preferable for the model not to resolve such features. The optimal constitutive relations and parameters obtained as a result of calibrating the model in (7) based on individual cycles are not presented here for brevity, as they reveal little difference.

In order to systematically assess the prediction capability of the calibrated models, we test them on "unseen" data from other cycles. Individual models are therefore trained on each of the five cycles for charge and discharge regimes and then used to assess the performance, in terms of the

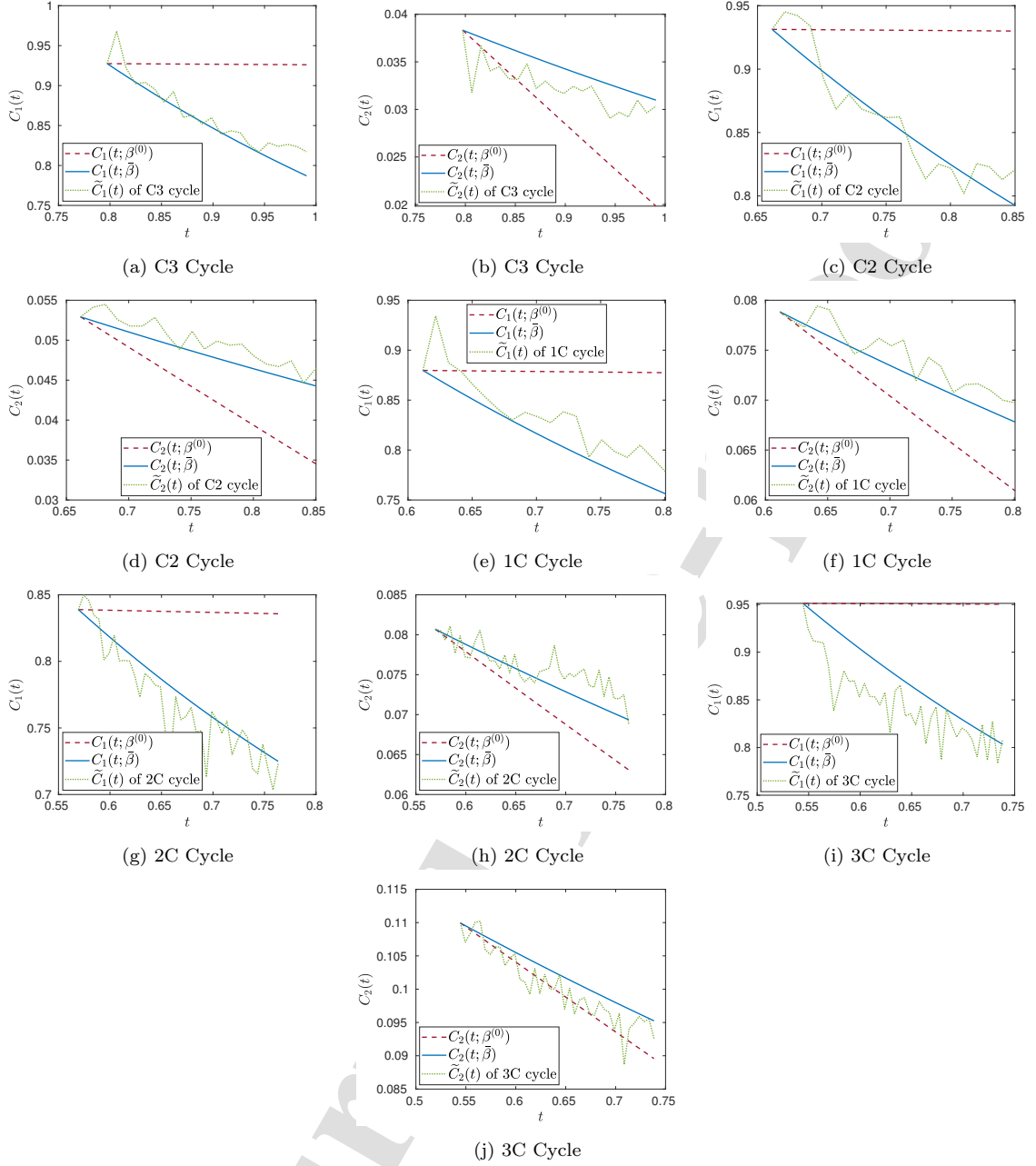


Figure 5: Dependence of the concentrations $C_1(t)$ and $C_2(t)$ on time for different cycles of the cell, using the initial guess for parameters $\beta^{(0)}$ (dashed red line), and the optimal values of parameters $\bar{\beta}$ (solid blue line). The experimental concentrations $\tilde{C}_1(t)$ and $\tilde{C}_2(t)$ for each cycle are shown as dotted green lines.

error functional $\mathcal{J}_2(\bar{\alpha}, \bar{\omega}_1, \bar{\omega}_2)$, on the data from other cycles. Additionally, in order to obtain a more robust model that can generalize well to a range of charge and discharge rates, the model is calibrated using the framework introduced in Section 4.3. The data comprising all cycles \mathcal{D}_t^{ch} will be used for training such a robust model in the charging regime and a similar calibration procedure

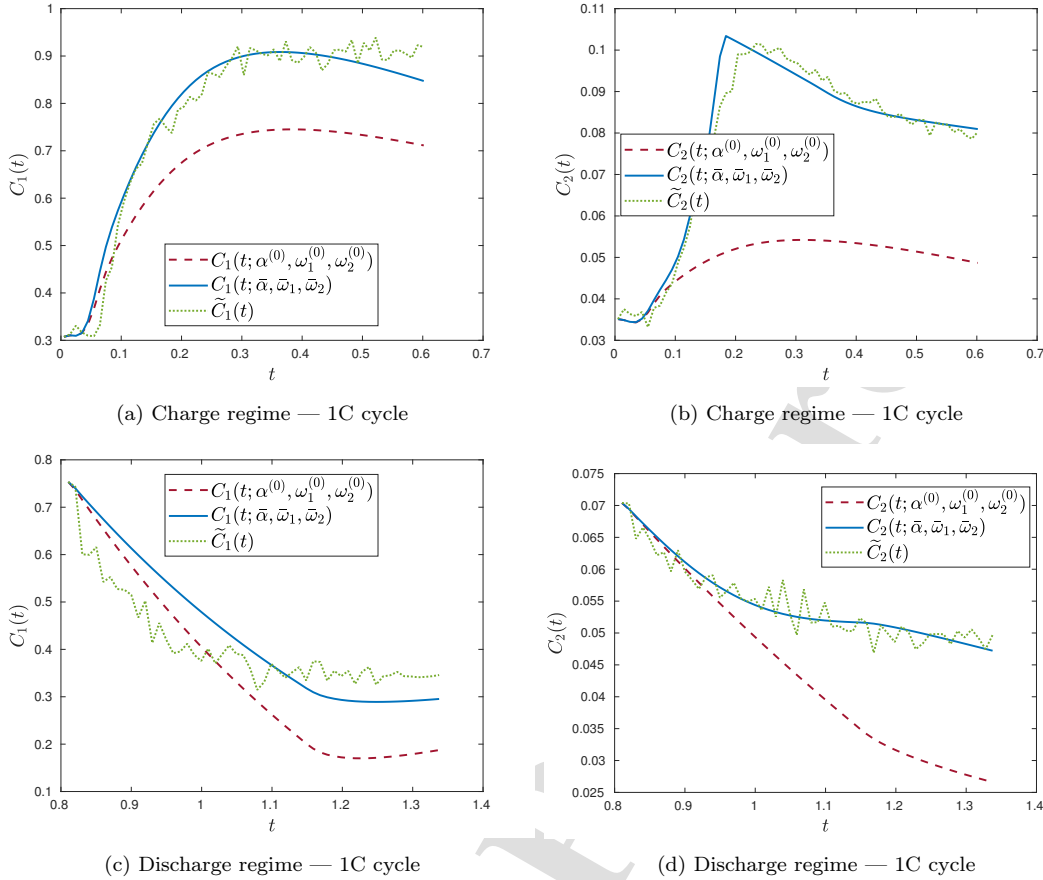


Figure 6: The dependence of concentrations $C_1(t)$ and $C_2(t)$ on time for the charge regime of the 1C cycle (a,b), and the discharge regime of the 1C cycle (c,d), corresponding to the initial guess for the parameter and constitutive relations $(\alpha^{(0)}, \omega_1^{(0)}, \omega_2^{(0)})$ (dashed red line), and the optimal parameter and constitutive relations $(\bar{\alpha}, \bar{\omega}_1, \bar{\omega}_2)$ (solid blue line) obtained by solving the inverse problem (14) with the data for the charge and discharge regimes of the 1C cycle, i.e., \mathcal{D}_{1C}^{ch} and \mathcal{D}_{1C}^{dch} , respectively. The experimental concentrations \tilde{C}_1 and $\tilde{C}_2(t)$ are shown with green dotted lines.

will be followed in the discharge regime by fitting the model to \mathcal{D}_t^{dch} . Also, in an attempt to find a robust model based on a minimal amount of experimental data, system (7) will be calibrated based on measurements in the charging cycles C3 and 3C only, i.e., $\bigoplus_i \mathcal{D}_i^{ch}, i \in \{C3, 3C\}$, again using the optimization framework from Section 4.3. A similar procedure will also be followed in order to calibrate system (7) based on measurements in the discharge regime, namely, using $\bigoplus_i \mathcal{D}_i^{dch}, i \in \{C3, 3C\}$. The results of this analysis are presented in Figure 7. As can be observed, each trained model performs best in the vicinity of the cycle (C-rate) used for its calibration, and the performance deteriorates as one deviates from this C-rate. Also, the model calibrated based on the data from all cycles shows an overall better and more robust performance in comparison to models that are trained based on individual cycles. In most cycles shown in Figure 7, the model calibrated based on all cycles outperforms most other models on each cycle. Moreover, the model calibrated based on the data from the C3 and 3C cycles only shows an overall good agreement with the model trained based on the data from all cycles, both for the charge and the discharge regimes.

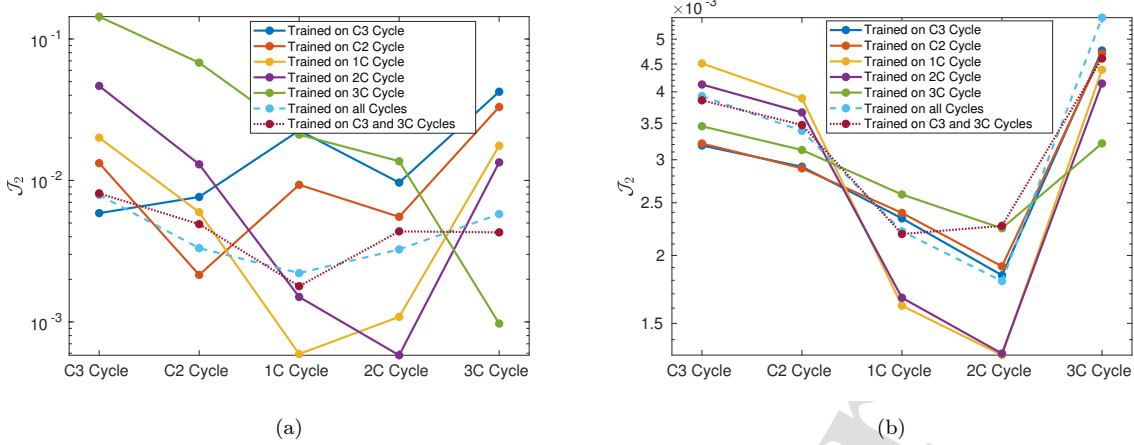


Figure 7: Dependence of the least-squares error $J_2(\bar{\alpha}, \bar{\omega}_1, \bar{\omega}_2; \mathcal{D}_i^{ch})$ between the experimental data from different cycles $i \in \mathcal{C}$, and the predictions of model (7) using the optimally reconstructed parameter and constitutive relations $(\bar{\alpha}, \bar{\omega}_1, \bar{\omega}_2)$ obtained by solving inverse problem (14) using the data corresponding to a given cycle, for the charge regime (a) and the discharge regime (b). For each line in the plots, model (7) is calibrated with Algorithm 1 using the data from the cycle indicated in the legend and then tested against data from all other cycles (indicated on the horizontal axis). The performance of the model calibrated using aggregated data \mathcal{D}_t^{ch} for (a) and \mathcal{D}_t^{dch} for (b) is shown with the dashed line, whereas the performance of model (7) calibrated based on the data from the C3 and 3C cycles only, i.e., $\bigoplus_i \mathcal{D}_i^{ch}, i \in \{C3, 3C\}$ for (a) and $\bigoplus_i \mathcal{D}_i^{dch}, i \in \{C3, 3C\}$ for (b), is shown with dotted lines.

The agreement between these two robust models indicates that a small amount of measurement data may be sufficient to calibrate our model without sacrificing accuracy, provided the measurement cycles used correspond to well-separated C-rates.

The optimal constitutive relations reconstructed by solving the inverse problem (14) using all cycles as training data for the charge (\mathcal{D}_t^{ch}) and discharge regimes (\mathcal{D}_t^{dch}) are shown in Figure 8. The optimal constitutive relations found by fitting model (7) to individual cycles for the charge and discharge regimes show a similar behavior and are not presented here for brevity. We note that the magnitude of the function ω is in both cases of the order of 0.1, highlighting the dominating effect of the intercalation/deintercalation relative to plating/stripping. It is also evident from Figure 8 that the optimal reconstructions of the constitutive relations and the parameter α are slightly different between the charge and discharge regimes. More specifically, the reconstructed functions ω_2 for the two regimes show similar behavior, however, the functions ω_1 and the parameter α reveal different behavior. This is somewhat unexpected and could potentially be due to one of the following reasons.

1. The dynamical behavior of the system in the charge and discharge regimes might show irreversibility. Note that the function ω is defined as a balance between Li plating and Li intercalation. This would imply that the competition between the side reaction and intercalation is different in the charge and discharge regimes. More specifically, at a particular state of the cell, charging might result in an intercalation-plating competition that is different from the deintercalation-stripping competition during discharging at the same state of the cell. This would indicate that Li metal is not stripped in exactly the same manner as it is plated. One possibility is that some plated Li loses electrical connectivity with the negative particles and consequently becomes electrochemically inactive. In other words, not all plated Li may be recoverable, giving rise to a different behavior of the function ω for stripping in comparison to plating.

2. The experimental conditions between the charge and discharge regimes might have slightly changed, hence, giving rise to different cell behavior for each regime.
3. The noise in the experimental data could be a factor that affects the calibration process resulting in a slightly different behavior between the charge and discharge regimes. As the inverse problem tends to be ill-posed, the effect of noise could be nonnegligible.

The time dependence of the concentrations obtained by solving problem (7) equipped with the constitutive relations and parameters α and β reconstructed optimally based on aggregated data from all cycles, cf. Section 4.3, are shown in Figures 9 and 10. The optimal constitutive relations and parameters used correspond to the dashed lines in Figure 7. As can be observed, the concentrations predicted by the model for all cycles follow the overall behavior of the experimental data. To quantify these observations, the deviation of the model predictions from the experimental concentrations is summarized in Table 1, where the values of the error functional $\mathcal{J}_2(\bar{\alpha}, \bar{\omega}_1, \bar{\omega}_2)$ and the corresponding Mean Absolute Error $MAE = \frac{1}{T} \int_0^T |C_1(t) - \tilde{C}_1(t)| dt$ are reported for different cycles. This data confirms that the reconstruction errors are indeed small relative to the magnitude of the concentrations, cf. Figure 6, and, interestingly, the MAEs for the plated Li are smaller by roughly one order of magnitude than for the intercalated Li. The deviations reported in Table 1 are not significant and can be attributed to the following reasons.

Metric / Cycle	C3	C2	1C	2C	3C	Mean
$\mathcal{J}_2(\bar{\alpha}, \bar{\omega}_1, \bar{\omega}_2)$	0.0104	0.0060	0.0048	0.0076	0.0088	0.0075
MAE for intercalated Li	0.0880	0.0653	0.0498	0.0426	0.0872	0.0666
MAE for plated Li	0.0031	0.0051	0.0067	0.0105	0.0061	0.0063

Table 1: Measures of deviations of the concentrations obtained by solving the forward model (7) using the optimal constitutive relations $\bar{\omega}_1, \bar{\omega}_2$ and parameters $\bar{\alpha}, \bar{\beta}$ reconstructed based on aggregated data from the experimental concentrations for different cycles. The last column represents the averages over all cycles.

1. The noise in the NMR measurements may be one source of inconsistency between the predictions of the mathematical model and the measured concentrations.
2. The computational framework relies on the assumed separability of the constitutive relation in terms of two factors depending on C_1 and C_2 , cf. (12), which is only an approximation and might not be true in practice. This issue could be addressed by reformulating inverse problem (14) with the help of the Kolmogorov-Arnold approximation theorem allowing one to represent a function of two variables, here $\omega(C_1, C_2)$, in terms of a suitable superposition of univariate functions which can be reconstructed as shown in Section 4.2.
3. The model does not take into account other undesired processes in the cell that might consume some of the interfacial current density, such as the secondary SEI growth. In other words, it is assumed that the current density applied to the cell is entirely consumed by the intercalation/deintercalation and plating/stripping processes.
4. Model (7) is calibrated based on a collection of data from a range of C-rates, while it is known that the dynamics of Li-ion cells highly depends on the C-rate. Different simplified models have been developed to describe the dynamics of the cell at different C-rates, e.g., Marquis et al. (2019); Richardson et al. (2020).

5. The optimization problems (9) and (14) are non-convex and may therefore admit multiple local minima. We cannot guarantee that the solutions we found with the gradient-based approach correspond to global minimizers.

Thus, it appears unlikely the optimal solutions presented in this section could be improved without redesigning the model. As can be observed in Figure 10, the experimental concentrations of plated Li demonstrate a partial recovery (stripping) which implies that some of the plated Li is inactive, and hence the calibrated constitutive relation should also take this phenomenon into account.

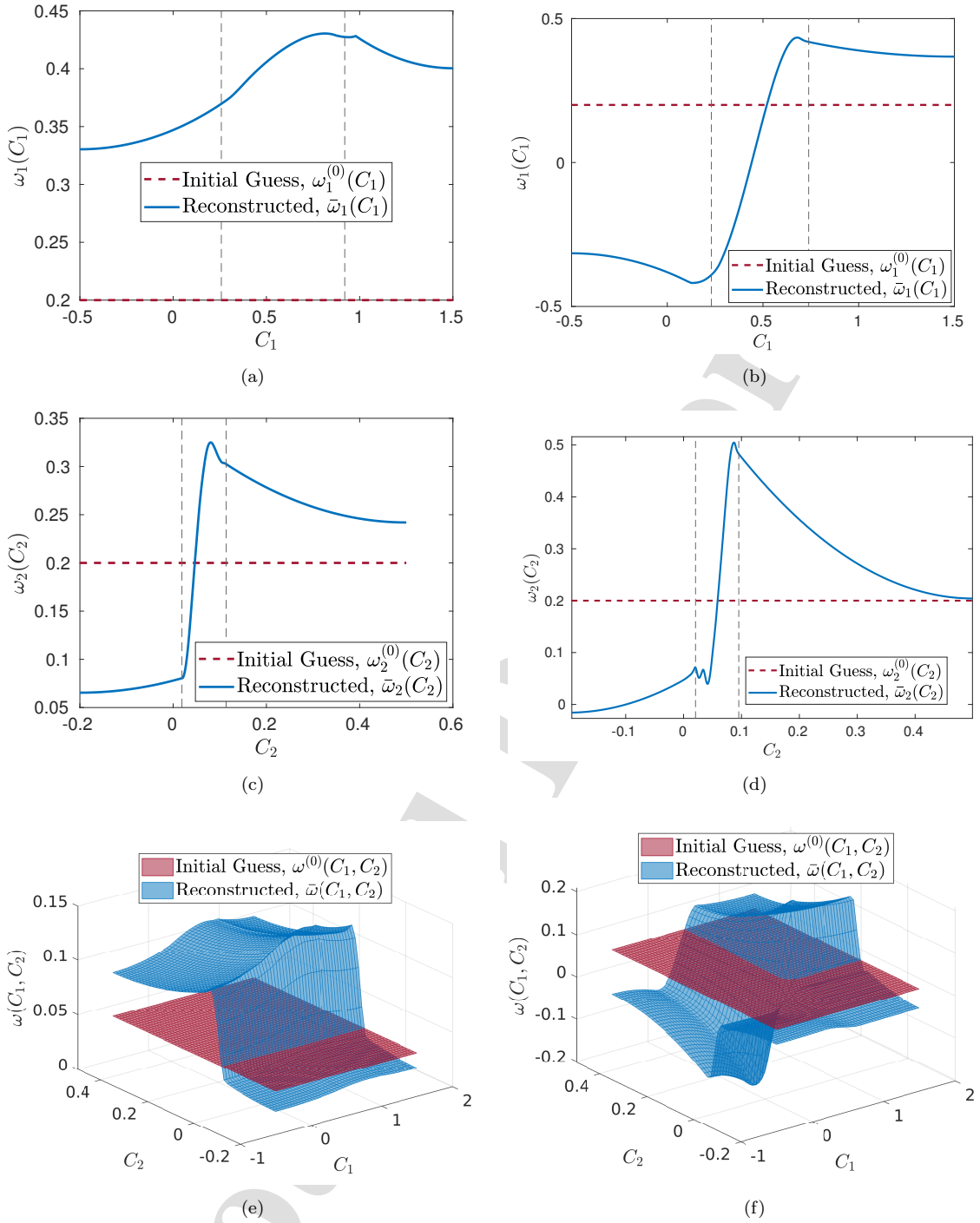


Figure 8: The initial guess for the constitutive relations $\omega_1^{(0)}(C_1)$, $\omega_2^{(0)}(C_2)$, and $\omega^{(0)}(C_1, C_2)$ (red), and the optimal form of the reconstructed constitutive relations $\bar{\omega}_1(C_1)$, $\bar{\omega}_2(C_2)$, and $\bar{\omega}(C_1, C_2)$ (blue) where model (7) is calibrated with stage II of Algorithm 1 using aggregated data for the charge regime \mathcal{D}_t^{ch} (a,c,e), and discharge regime \mathcal{D}_t^{dch} (b,d,f). The factors $\omega_1(C_1)$ and $\omega_2(C_2)$ are shown in panels, respectively, (a,b) and (c,d), whereas panels (e,f) show their product (12).

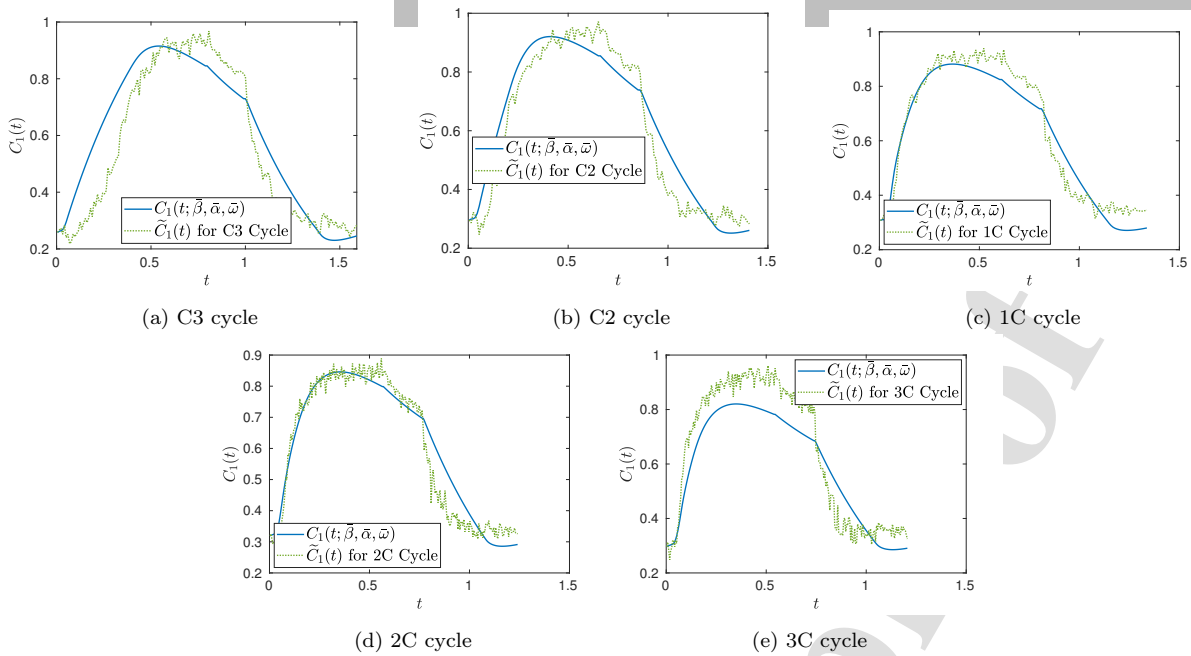


Figure 9: The dependence of the state variable $C_1(t)$ on time in the solution of the forward problem (7) using the optimal parameters values and optimal forms of the constitutive relation $(\bar{\beta}, \bar{\alpha}, \bar{\omega})$ reconstructed by calibrating system (7) using aggregated data \mathcal{D}_t for charge, discharge and OCV regimes, cf. Section 4.3. The dashed green and the solid blue lines represent the experimental concentrations and the solution of the forward problem (7) using optimal parameters and constitutive relations, respectively.

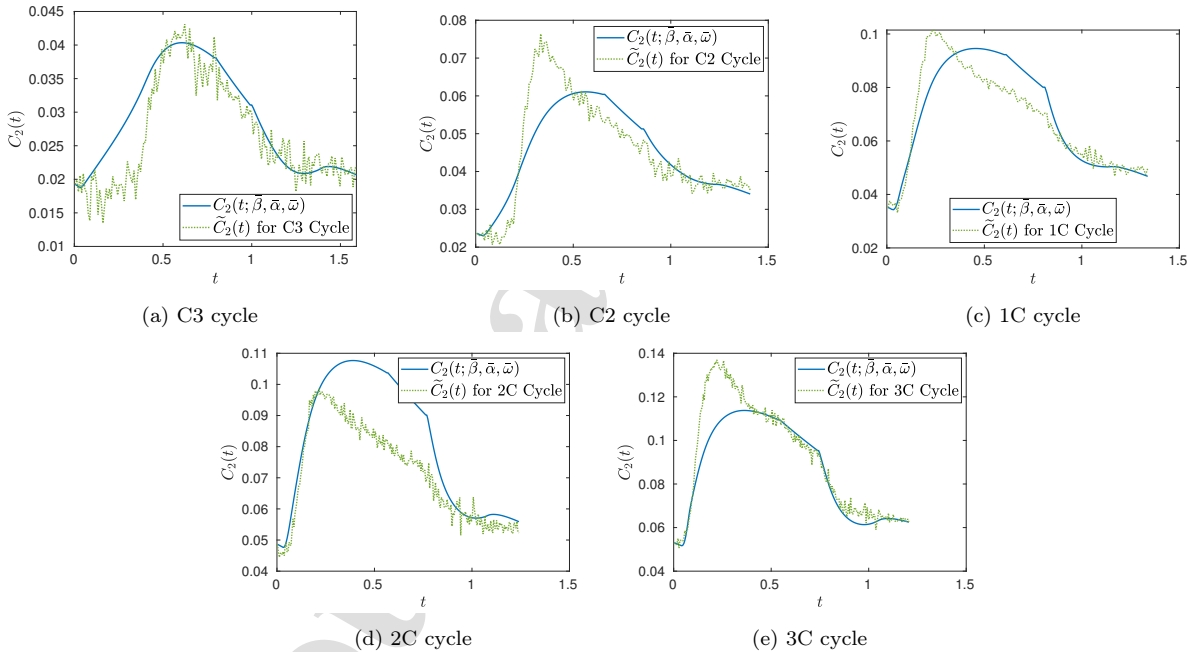


Figure 10: The dependence of the state variable $C_2(t)$ on time in the solution of the forward problem (7) using the optimal parameters values and optimal forms of the constitutive relation $(\bar{\beta}, \bar{\alpha}, \bar{\omega})$ reconstructed by calibrating system (7) using aggregated data \mathcal{D}_t for charge, discharge and OCV regimes, cf. Section 4.3. The dashed green and the solid blue lines represent the experimental concentrations and the solution of the forward problem (7) using optimal parameters and constitutive relations, respectively.

6. Discussion and Conclusions

In this study, Li plating was investigated as one of the main degradation mechanisms in Li-ion cells using mathematical and computational tools. Physical modeling was employed in order to model the physical and chemical processes in the cell. Starting with the DFN model, we employed a variety of techniques, including asymptotic reduction and averaging, in order to simplify it to an SP model with side reactions, tailored to our experimental data. The resulting model tracks the evolution of two lumped concentrations: the intercalated Li and plated Li in the cell. Notably, the model has the following properties: (i) concentrations are averaged over their corresponding spatial domains to eliminate spatial dependence from the model, (ii) the model takes the form of an ODE system describing the evolution of the averaged quantities, circumventing the need to solve for the potential distribution in the cell, as is done in the DFN models, due to the simplifying assumptions of the proposed framework, (iii) the model accounts for both relaxation and excitation dynamics in the cell, with excitation being dominant, and (iv) the model accounts for both plating and stripping processes in the cell, allowing for the recovery of some of the plated Li. These properties make the model a good candidate for online state estimation and monitoring of the cells. From the physical modeling perspective, the study by [Planella and Widanage \(2023\)](#) bears the closest resemblance to this work, although it does not account for Li stripping. [Sahu and Foster \(2023\)](#) consider more interactions between different phases of Li in the cell and develop a more comprehensive mathematical model capable of predicting both plating and stripping. Our resulting physical model involves a number of physical parameters and a constitutive relation that require calibration using experimental data. Inverse modeling and optimization techniques are employed for this purpose in order to determine the optimal value of parameters and the optimal form of constitutive relations, aiming to minimize discrepancies between model outputs and experimental data. To our knowledge, this study represents the first instance of using inverse modeling to optimally predict Li plating and stripping in Li-ion cells. In relying on the calculus of variations, the proposed approach represents an alternative with respect to machine learning techniques which have recently gained popularity.

We note that the negative electrode material utilized in this study is silicon. This material experiences significant volume variations during charge/discharge cycles of the cell, a phenomenon linked to its high charge density. These volume changes may influence the model performance, as we have not explicitly accounted for this phenomenon. Nonetheless, the calibrated parameters and constitutive relations of the model may implicitly account for this effect. It is important to note that the modeling framework developed in this study (combining physical modeling, asymptotic reduction and averaging with inverse modeling based on adjoint-based optimization) can be extended to other negative electrode materials such as graphite without any significant changes. However, one cannot expect that a model calibrated using experimental data from a battery cell built with a different material would yield a constitutive relation similar to the one inferred in this study. The significant volume changes associated with silicon anodes may influence the calibration process and lead to different optimal parameters and constitutive relations compared to cells with other chemistries. Understanding this aspect remains an open question for future investigation.

An important consideration is the range of validity of the Li-plating model. As highlighted by [Marquis et al. \(2019\)](#), the SP model remains valid up to a C-rate of 1C, beyond which it begins to diverge from the DFN model. In this study, we have also developed a variant of the SP model that accounts for Li-plating as a side reaction. Consequently, it is important to investigate the range of validity of this model. As is evident in Figures [9](#) and [10](#), the model calibrated based on

data from a range of C-rates demonstrates the ability to predict intercalation/deintercalation and plating/stripping behavior in an overall good manner. Due to the fact that the mathematical model is calibrated using real data, its fidelity may extend beyond 1C rate. Figure 7 suggests that a model calibrated based on data for a specific C-rate performs well in its proximity, and its performance gradually deteriorates as the C-rate deviates from the C-rate used for training. Thus, the range of validity of the model may depend on the training process used to calibrate the model, which, in turn, is determined by the specific application of the model and availability of the data.

We remark that measurement uncertainty may propagate through the inverse modeling process, thereby affecting the inferred constitutive relations. First, it influences the accuracy with which one can evaluate the error functionals (8) and (13). Second, in Algorithm 1, the adjoint system (26) is solved at each iteration and depends on the difference between model predictions and experimental measurements. Therefore, measurement uncertainty can influence the solution of the adjoint system, which in turn impacts the calculation of the L^2 gradients via (32), owing to the dependence of the gradients on the adjoint variables. Consequently, the accuracy of the computed optimal constitutive relations and parameters can be compromised by measurement noise. However, it is important to note that the method introduced in Section 4.3 partially addresses this issue by solving the inverse problem using aggregated data from multiple cycles. Furthermore, enforcement of the regularity of the constitutive relations by reconstructing them in a suitable Sobolev space, which can be viewed as a form of low-pass filtering (Protas et al., 2004), reduces the sensitivity of the optimal solution to small-scale noise in the measurements.

The proposed physical modeling and computational framework can also be extended to differentiate between different phases of Li within the cell, particularly non-recoverable Li and recoverable Li. In the current study, these two phases are not distinguished as the experimental data for inactive Li is not available. While the present framework solely focuses on Li plating, it can be readily expanded to include other degradation mechanisms.

Acknowledgments

The authors thank Jamie Foster for helpful discussions. This research was supported by a Collaborative Research & Development grant # CRD494074-16 from Natural Sciences & Engineering Research Council of Canada.

Conflict of interest

The authors declare no potential conflict of interests.

Appendix A. DFN Model

For completeness, different components of the DFN model are discussed below.

Appendix A.1. Charge Conservation in the Solid Phase

This sub-model describes charge conservation within the solid phase of the negative electrode. The charge conservation is stated in the macroscale in Ω_n and the corresponding potential profile

is obtained by solving the following equation

$$\begin{aligned} \frac{\partial J_n}{\partial x} &= -a_n J_{n,tot}, \\ J_n &= -\sigma_n \frac{\partial \phi_n}{\partial x}, \\ J_n &= J_{app}, \quad \text{at } x = 0, \\ J_n &= 0, \quad \text{at } x = L_n, \end{aligned} \tag{A.1}$$

where $\phi_n[V]$ is the electrostatic potential in the solid phase, $J_n[\frac{A}{m^2}]$ is the current density in the solid phase, $\sigma_n[S/m]$ is the effective conductivity of the solid particles, $J_{n,tot}[\frac{A}{m^2}]$ is the source/sink term representing the total current density flux at the solid-electrolyte interface of the negative electrode due to intercalation and side reactions, $J_{app}[\frac{A}{m^2}]$ denotes the current density applied to the cell, and $a_n = \frac{3}{R_n} [\frac{1}{m}]$ is the effective surface area of the anode particles per unit volume. Similarly, the charge conservation in the solid phase for the positive electrode is expressed as

$$\begin{aligned} \frac{\partial J_p}{\partial x} &= -a_p J_{p,tot}, \\ J_p &= -\sigma_p \frac{\partial \phi_p}{\partial x}, \\ J_p &= 0, \quad \text{at } x = L - L_p, \\ J_p &= J_{app}, \quad \text{at } x = L. \end{aligned} \tag{A.2}$$

Note that the total current density is a source/sink term that is present in the model for the negative electrode and positive electrode only and vanishes in the separator

$$J_{tot} = \begin{cases} J_{n,tot} = J_{n,int} + J_{n,sr} & 0 \leq x \leq L_n, \\ 0 & L_n \leq x \leq L - L_p, \\ J_{p,tot} = J_{p,int} & L - L_p \leq x \leq L, \end{cases} \tag{A.3}$$

where $J_{n,int}$, $J_{n,sr}$ and $J_{p,int}$ represent the intercalation and side reaction current densities at the solid-electrolyte interface of the negative electrode and the intercalation current density at the solid-electrolyte interface of the positive electrode, respectively. No side reaction is assumed on the positive electrode.

Appendix A.2. Li Ion Transport in the Solid Phase

This sub-model describes the slow diffusion of Li ions inside the solid phase. The diffusion equation for Li transport in the solid phase is stated in the microscale in the spherical coordinates for a representative particle (assuming uniformity along all particles) as

$$\begin{aligned} \frac{\partial C_n}{\partial t} &= \frac{1}{r^2} \frac{\partial}{\partial r} \left(r^2 D_n \frac{\partial C_n}{\partial r} \right), \quad r \in (0, R_n), \\ \frac{\partial C_n}{\partial r} &= 0, \quad \text{at } r = 0, \\ -D_n \frac{\partial C_n}{\partial r} &= \frac{J_{n,tot}}{F}, \quad \text{at } r = R_n, \\ C_n &= C_{n_i}(r), \quad \text{at } t = 0, \end{aligned} \tag{A.4}$$

where $C_n = C_n(r, t) [\frac{mol}{m^3}]$, $D_n [\frac{m^2}{s}]$, $C_{n_i}(r)$ are the Li concentration, the diffusion coefficient, and initial concentration profile, respectively. The Li flux on the surface of the anode particle is $-J_{n,tot}/F$, where $J_{n,tot} [\frac{A}{m^2}]$ is the current density flux at the interface (obtained from the Butler-Volmer relation to be described in [Appendix A.5](#) below), and $F [\frac{A \cdot s}{mol}]$ is Faraday's constant. Note that, to also account for side reactions, the interfacial current density $J_{n,tot}$ will be replaced with the intercalation current density $J_{n,int}$ in [Section 3.2](#). Similarly, Li transport in the solid phase of the positive particles is governed by

$$\begin{aligned} \frac{\partial C_p}{\partial t} &= \frac{1}{r^2} \frac{\partial}{\partial r} \left(r^2 D_p \frac{\partial C_p}{\partial r} \right), & r \in (0, R_p), \\ \frac{\partial C_p}{\partial r} &= 0, & \text{at } r = 0, \\ -D_p \frac{\partial C_p}{\partial r} &= -\frac{J_{p,tot}}{F}, & \text{at } r = R_p, \\ C_p &= C_{p_i}(r), & \text{at } t = 0. \end{aligned} \quad (\text{A.5})$$

Appendix A.3. Charge Conservation in the Electrolyte Phase

This sub-model describes charge conservation within the electrolyte phase. The corresponding continuity equation is defined in the macroscale in Ω in terms of the potential profile and has the form

$$\begin{aligned} \frac{\partial}{\partial x} J_e &= a J_{tot}, \\ J_e &= -\sigma_e B(x) \left[\frac{\partial}{\partial x} \phi_e - 2(1-t^+) \frac{RT}{F} \frac{\partial}{\partial x} \log C_e \right], \\ \frac{\partial}{\partial x} \phi_e &= 2(1-t^+) \frac{RT}{F} \frac{\partial}{\partial x} \log C_e, & \text{at } x = 0, L, \end{aligned} \quad (\text{A.6})$$

where J_e is the current density in the electrolyte phase, ϕ_e is the potential in electrolyte phase, σ_e is the electrolyte conductivity, $B = B(x, t)$ is the permeability, and $t^+ = t^+(C_e)$ is the transference number.

Appendix A.4. Li Ion Transport in the Electrolyte Phase

This sub-model describes the transport of Li ions within the electrolyte phase at macroscale, with the corresponding continuity equation stated on Ω in terms of the concentration profile of Li ions as

$$\begin{aligned} \frac{\partial}{\partial t} (\epsilon C_e) &= -\frac{\partial}{\partial x} N_e + \frac{a}{F} J_{tot}, \\ N_e &= -D_e B(x) \frac{\partial}{\partial x} C_e + \frac{t^+}{F} J_e, \\ \frac{\partial}{\partial x} C_e &= \frac{1}{D_e B(x)} \frac{t^+}{F} J_e, & \text{at } x = 0, L, \\ C_e &= C_{e_i}, & \text{at } t = 0. \end{aligned} \quad (\text{A.7})$$

where $\epsilon = \epsilon(x, t)$ is the porosity of the domain, $C_e = C_e(x, t)$ is the Li ion concentration in the electrolyte, $D_e = D_e(C_e)$ is the diffusion coefficient in the electrolyte phase, and J_e is the current density vector in the electrolyte phase.

Appendix A.5. Interfacial Dynamics

Interfacial processes in the cell are usually modeled based on the well-known Butler-Volmer (BV) relations for electrochemical kinetics. They describe how the current density at the solid-electrolyte interface depends on the potential difference between the electrode surface and the neighboring electrolyte. Several variants of these semi-empirical relations exist in the literature as surveyed by [Suresh and Rengaswamy \(2018\)](#) and [Dickinson and Wain \(2020\)](#). Depending on the nature of the problem and the required level of complexity, a suitable BV relation can be used. In particular, Lithium plating and stripping can also be modeled as interfacial processes by adding an extra BV equation for each side reaction to represent its rate as a function of overpotential, as first introduced by [Arora et al. \(1999\)](#) and later expanded by [Yang et al. \(2018\)](#). The BV relations representing interfacial phenomena at the solid-electrolyte interface are ([Arora et al., 1999](#); [Yang et al., 2018](#))

$$\begin{aligned} J_{n,int} &= j_{int} [\exp(\alpha_{a,int} f \eta_{int}) - \exp(-\alpha_{c,int} f \eta_{int})], \\ J_{n,sr} &= j_{sr} [\exp(\alpha_{a,sr} f \eta_{sr}) - \exp(-\alpha_{c,sr} f \eta_{sr})], \\ \eta_{int} &= \phi_n - \phi_e - U_n, \\ \eta_{sr} &= \phi_n - \phi_e - U_{sr}, \\ j_{int} &= k_{a,int}^{\alpha_{c,int}} k_{c,int}^{\alpha_{a,int}} C_n^{\alpha_{c,int}} C_e^{\alpha_{a,int}} (C_{max} - C_n)^{\alpha_{a,int}}, \\ j_{sr} &= k_{a,sr}^{\alpha_{c,sr}} k_{c,sr}^{\alpha_{a,sr}} C_e^{\alpha_{a,sr}}, \end{aligned} \tag{A.8}$$

where j_{int} and j_{sr} are the exchange current densities for the intercalation and side reactions, respectively, η_{int} and η_{sr} are the overpotentials at the solid-electrolyte interface for the intercalation and side reactions, respectively, U_n and U_{sr} are equilibrium potentials, $k_{c,int}$, $k_{a,int}$, $k_{c,sr}$, $k_{a,sr}$ are the reaction rates for cathodic and anodic currents of intercalation and cathodic and anodic currents of side reaction, respectively, C_{max} is the saturation concentration of Li in solid phase, and $C_n = C_n|_{r=R_n}$ refers to solid phase concentration on the surface of the particle. On the other hand, [Escalante et al. \(2020\)](#) use a more sophisticated technique for modeling side reaction in the cell, where one BV relation is used to represent both Li intercalation/deintercalation and plating/stripping as

$$j_{int} = k_0 C_n^{0.5} C_e^{0.5} (C_{max} - C_n)^{0.5} \tanh \left(\gamma \frac{C_{max} - C_n}{C_{max}} \right),$$

where the intercalation exchange current density is multiplied by a factor γ describing how the total current is divided between the intercalation and side reactions, hence, reducing the formulations for exchange current densities. Thus, the two equations for exchange current density of intercalation and side reaction are replaced with one, with a significantly lower number of parameters. As can be observed, the exchange current densities are concentration-dependent, and most authors have used similar functional forms to model this dependency. [Daniels et al. \(2023\)](#) leverage a data-driven approach in order to optimally construct the exchange current density as a function of concentration, without assuming any *a priori* functional form for this function. In our modeling approach, we employ a combination of the aforementioned techniques: we use separate BV relations (A.8) in order to account for the side reaction and introduce a variable to represent the ratio of the exchange current densities in the intercalation and plating processes that reflects the competition between the intercalation versus plating, cf. Section 3.2. This key variable is concentration-dependent and its optimal functional form will be determined using data-driven inverse modeling techniques. Before we start this analysis, in the next section we present a dimensionless version of our model.

Appendix B. Dimensionless Variables

The model introduced in (A.1)–(A.7) can be rescaled to a dimensionless form that will facilitate its asymptotic reduction. First, the independent and dependent variables are rescaled as follows

$$\begin{aligned} x &= L\hat{x}, & L_n &= Ll_n, & L_p &= Ll_p, & r &= R_n\hat{r}_n, & r &= R_p\hat{r}_p, \\ J_k &= J_t\hat{J}_k, & J_K &= J_t\hat{J}_K, & j_{int} &= J_t\hat{j}_{int}, & j_{sr} &= J_t\hat{j}_{sr}, & \phi_n &= \phi_t\hat{\phi}_n, \\ \phi_e &= \frac{1}{f}\hat{\phi}_e, & U_n &= \phi_t\hat{U}_n, & \eta_{int} &= \frac{1}{f}\hat{\eta}_{int}, & \eta_{sr} &= \frac{1}{f}\hat{\eta}_{sr}, & \sigma_e &= \sigma_e^{\text{typ}}\hat{\sigma}_e, \\ C_n &= C_n^{\max}\hat{C}_n, & C_p &= C_p^{\max}\hat{C}_p, & C_e &= C_e^{\max}\hat{C}_e, & C_{sr} &= C_n^{\max}\hat{C}_{sr}, & t &= \tau\hat{t}, \\ N_e &= \frac{D_e^{\text{typ}}C_e^{\max}}{L}\hat{N}_e, & D_n &= D_n^{\text{typ}}\hat{D}_n, & D_e &= D_e^{\text{typ}}\hat{D}_e, & D_p &= D_p^{\text{typ}}\hat{D}_p, \end{aligned}$$

where $\hat{x} \in [0, l]$, $l = 1$, $k \in \{n, e, p\}$, $K \in \{\text{tot}, \text{int}, \text{sr}, \text{app}\}$, $f = \frac{F}{RT}$, J_t is the typical current density in the cell, ϕ_t is the typical potential in the cell components, D_k^{typ} the typical diffusion coefficient, σ_e^{typ} the typical conductivity, C_k^{\max} the maximum concentration of Lithium in the corresponding domain, and $\tau = \frac{FC_n^{\max}L}{J_t}$ is the discharge time scale. Note that $\frac{1}{f} = \frac{RT}{F}$ has the unit of Volts and is defined as the thermal voltage of the cell. The dimensionless parameters are then defined as

$$\begin{aligned} \lambda &= \phi_t f, & \Xi_n &= \frac{\sigma_n}{fLJ_t}, & \Xi_e &= \frac{\sigma_e^{\text{typ}}}{fLJ_t}, & \Xi_p &= \frac{\sigma_p^{\text{typ}}}{fLJ_t}, & \mathcal{K}_n &= \frac{R_n^2}{\tau D_n^{\text{typ}}}, \\ \mathcal{K}_e &= \frac{L^2}{\tau D_e^{\text{typ}}}, & \mathcal{K}_p &= \frac{R_p^2}{\tau D_p^{\text{typ}}}, & \gamma_n &= \frac{\tau J_t}{R_n F C_n^{\max}}, & \gamma_e &= \frac{\tau J_t}{L F C_e^{\max}}, & \gamma_p &= \frac{\tau J_t}{R_p F C_p^{\max}}. \end{aligned}$$

The system of dimensionless equations is presented in full in (1)–(2).

Appendix C. Derivation of Asymptotic Reduction

In this section, we use asymptotic reduction to derive the simplified model. We start by applying this technique to different equations in system (1)–(2).

Electrode Potential. We start with the equations for the negative electrode potential. Averaging (1a) over the negative electrode domain, using the fundamental theorem of calculus, and applying boundary conditions (2e) and (2f) we get

$$\begin{aligned} \frac{1}{l_n} \int_0^{l_n} \frac{\partial}{\partial x} J_n dx &= -\frac{1}{l_n} \int_0^{l_n} a_n L J_{n,tot} dx = 0 - J_{app}, \\ \bar{J}_{n,tot} &= \frac{J_{app}}{a_n L l_n}, \quad \bar{J}_{n,tot} := \frac{1}{l_n} \int_0^{l_n} J_{n,tot} dx, \end{aligned} \tag{C.1}$$

where $\bar{J}_{n,tot}$ is the total current density averaged over the domain of the negative electrode. Hence, by averaging over the spatial domain the partial differential equation for the charge conservation in the solid phase reduces to an algebraic equation. This algebraic equation states that all the current applied to the anode during charge/discharge will be consumed at the solid-electrolyte interface for intercalation/deintercalation or side reactions, and acts as a constraint on the system

of equations. Performing similar analysis for the positive electrode using (1d), (2g) and (2h) results in $\bar{J}_{p,tot} = -\frac{J_{app}}{a_p L l_p}$. Asymptotic reduction of (1b) at the leading-order leads to

$$\frac{\partial \phi_{n,0}}{\partial x} = 0, \quad 0 < x < l_n. \quad (\text{C.2})$$

Thus, $\phi_{n,0} = \phi_{n,0}(t)$, and the leading-order potential is homogeneous in space. Also, at the first-order, we have

$$J_{n0} = -\Xi_n \frac{\partial \phi_{n,1}}{\partial x}. \quad (\text{C.3})$$

Interfacial Kinetics. In the next step, we simplify the BV relations introduced in (1k) and (1l). For this purpose, we first linearize the BV relation, and secondly, we also linearize the relations between the equilibrium potentials and concentrations. Using assumption A1, the BV relation (1k) can be linearized as

$$J_{int} \cong j_{int}(\alpha_{a,int} + \alpha_{c,int})\eta_{int},$$

and similarly for (1l). Invoking assumption A2, they can be further simplified to

$$J_{int} = j_{int}\eta_{int}, \quad (\text{C.4a})$$

$$J_{sr} = j_{sr}\eta_{sr}. \quad (\text{C.4b})$$

The overpotentials in the BV relations involve terms related to the equilibrium potentials of intercalation and side reaction. As stipulated by assumption A4, the equilibrium potentials are expanded as

$$U_n(C_n) = U_n|_{C_{n,0}} + \lambda^{-1} \frac{dU_n}{dC_n}|_{C_{n,0}} C_{n,1} + \dots, \quad (\text{C.5a})$$

$$U_{sr}(C_{sr}) = U_{sr}|_{C_{sr,0}} + \lambda^{-1} \frac{dU_{sr}}{dC_{sr}}|_{C_{sr,0}} C_{sr,1} + \dots, \quad (\text{C.5b})$$

where $C_{n,0}$ and $C_{sr,0}$ are the leading-order concentrations used as the reference states for linearization, and $C_{n,1}$ and $C_{sr,1}$ are the first-order approximations of concentrations i.e., $C_n \cong C_{n,0} + \lambda^{-1}C_{n,1}$ and $C_{sr} \cong C_{sr,0} + \lambda^{-1}C_{sr,1}$. Hence, performing asymptotic reduction on BV relation (C.4a), and using (1m) and (C.5a), we get

$$J_{int,0} = (j_{int,0} + \lambda^{-1}j_{int,1}) \times \\ \left(\lambda \left[\phi_{n,0} + \lambda^{-1}\phi_{n,1} - U_n|_{C_{n,0}} - \lambda^{-1} \frac{dU_n}{dC_n}|_{C_{n,0}} C_{n,1} \right] - \phi_{e,0} - \lambda^{-1}\phi_{e,1} + \dots \right).$$

Thus, at the leading-order we have

$$J_{int,0} = \underbrace{j_{int,0} \left(\phi_{n,1} - \phi_{e,0} - \frac{dU_n}{dC_n}|_{C_{n,0}} C_{n,1} \right)}_{J_n^\dagger} + \underbrace{j_{int,1} \left(\phi_{n,0} - U_n|_{C_{n,0}} \right)}_{J_n^\ddagger}, \quad (\text{C.6})$$

where J_n^\dagger and J_n^\ddagger represent (at the leading-order) the excitation and relaxation dynamics of the cell, respectively. This choice of excitation and relaxation dynamics in (C.6) is justified in two ways. First, as explained in Section 3.3, the second term is assumed to be zero in the study by Planella

and Widanage (2023). However, their assumption leads to the lack of relaxation dynamics in the positive electrode. For this reason, the second term in (C.6) is supposed to take into account the relaxation dynamics of the cell. Then, the second term represents the deviation of the leading-order potential of the negative particle from its equilibrium potential. Setting this term to zero eliminates the relaxation dynamics of the negative particle. Equation (C.6) will be used in subsequent analysis for describing $(\phi_{n,1} - \phi_{e,0})$ as

$$\phi_{n,1} - \phi_{e,0} = \frac{J_n^\dagger}{j_{int,0}} + \frac{dU_n}{dC_n}|_{C_{n,0}} C_{n,1}. \quad (\text{C.7})$$

Next, we focus our attention on the current density of side reactions. Assuming that the side reactions in the cell are weak as stipulated by assumption A3, we postulate that $j_{sr} = \lambda^{-1} \tilde{j}_{sr}$, where \tilde{j}_{sr} is of a different order of magnitude than j_{sr} . This choice allows us to capture the effect of side reactions at the order of λ^{-1} (a smaller order of magnitude than the intercalation). At the leading-order, the side reaction is not observed due to this choice reflecting the assumption that it is weak. Therefore, performing asymptotic reduction on (C.4b), and using (1n) and (C.5b), we get

$$J_{sr,0} = \lambda^{-1} \tilde{j}_{sr,0} \left(\lambda \left[\phi_{n,0} - U_{sr}|_{C_{sr,0}} \right] + \phi_{n,1} - \phi_{e,0} - \frac{dU_{sr}}{dC_{sr}}|_{C_{sr,0}} C_{sr,1} \right), \quad (\text{C.8})$$

and then by rearranging this equation

$$J_{sr,0} = \tilde{j}_{sr,0} \left(\phi_{n,0} - U_{sr}|_{C_{sr,0}} \right) + \lambda^{-1} \tilde{j}_{sr,0} \left(\phi_{n,1} - \phi_{e,0} - \frac{dU_{sr}}{dC_{sr}}|_{C_{sr,0}} C_{sr,1} \right). \quad (\text{C.9})$$

As already mentioned, the side reaction is only considered in the first-order approximation and vanishes at the leading-order. Hence, to eliminate the term of order $\mathcal{O}(1)$ in (C.9), we set $\phi_{n,0} = U_{sr}|_{C_{sr,0}}$. Therefore, $U_{sr}|_{C_{sr,0}}$ is also uniform in space (as is $\phi_{n,0}$), which recovers the underlying assumption of the SP model that the behavior of all solid particles is uniform in space at the macroscale. Note that this assumption will impose the uniformity of $U_n|_{C_{n,0}}$ in space as well. Hence, starting with particles with the same initial concentrations, they will evolve in exactly same manner. Consequently, solving for one representative particle suffices to capture the dynamics of all solid particles. Note that quantities that are concentration-dependent will then be uniform in space, and can be easily averaged. Thus, the expression for the relaxation dynamic in (C.6) becomes after averaging

$$\bar{J}_n^\dagger = j_{int,1} \left(U_{sr}|_{C_{sr,0}} - U_n|_{C_{n,0}} \right). \quad (\text{C.10})$$

By substituting (C.7) into (C.9) we get for the side reaction current density

$$J_{sr,0} = \lambda^{-1} \tilde{j}_{sr,0} \left(\frac{J_n^\dagger}{j_{int,0}} + \frac{dU_n}{dC_n}|_{C_{n,0}} C_{n,1} - \frac{dU_{sr}}{dC_{sr}}|_{C_{sr,0}} C_{sr,1} \right). \quad (\text{C.11})$$

The average current density for the side reaction $\bar{J}_{sr,0}$ can be computed by averaging (C.11) over the negative electrode domain. Note that the exchange current density is a function of the concentration at the interface, however, due to the inherent assumption in the SP model, where particles are uniform in space, the exchange current density will also be uniform in electrode domain. Also,

the excitation current density averaged over the negative electrode domain becomes $\bar{J}_n^\dagger = \frac{J_{app}}{a_n L l_n}$ according to (C.1). We can then average the expression (C.11) as

$$\bar{J}_{sr,0} = \frac{j_{sr,0}}{a L l_n j_{int,0}} J_{app} + j_{sr,0} \frac{dU_n}{dC_n} \Big|_{C_{n,0}} \bar{C}_{n,1} - j_{sr,0} \frac{dU_{sr}}{dC_{sr}} \Big|_{C_{sr,0}} \bar{C}_{sr,1}. \quad (\text{C.12})$$

Equations (C.10) and (C.12) will be used in subsequent analysis.

Conservation of Charge. The conservation of charge within the cell implies that the quantity of charge entering the cell is equivalent to the amount exiting the cell at each instance of time. This fundamental principle reflects the balance of electrical charge within the cell, ensuring that the net charge in the cell remains constant throughout the cell processes. The total current density on the negative electrode can be split into two components $J_{n,tot} = J_{n,tot,0} + \lambda^{-1} J_{n,tot,1}$, and $J_{n,tot,0} = J_{n,int,0} + J_{sr,0}$. At the leading-order $J_{sr,0}$ vanishes (due to assumption A3), and the leading-order interfacial current density is given entirely by the intercalation current density, $J_{n,tot,0} = J_{n,int,0}$. This implies that at the leading-order, the dynamics are driven merely by intercalation (and there are no side reactions). The side reaction will enter as a correction term in the first-order approximation. Also, the intercalation current density at the leading-order can be split into two components, namely, the excitation (J_n^\dagger) and relaxation dynamics (J_n^\ddagger). Hence, the total current density on the negative electrode becomes $J_{n,tot} = J_n^\dagger + J_n^\ddagger + \lambda^{-1}(J_{int,1} + J_{sr,1})$. A similar analysis can be performed for the positive electrode, yielding $J_{p,tot} = J_p^\dagger + J_p^\ddagger$. Note that in the positive electrode there is no side reaction, and hence the correction to intercalation process is absent.

The Li concentration on the interface of the electrode particle ($r = 1$) is homogeneous over the electrode spatial domain due to the macroscale uniformity of electrode particles assumed in the SP model. Hence the total current density is uniform over space and equal to its average value. Averaging each of these relations over the corresponding electrode domains, we get $\bar{J}_{n,tot} = \bar{J}_n^\dagger + \bar{J}_n^\ddagger + \lambda^{-1}(\bar{J}_{int,1} + \bar{J}_{sr,1})$, and $\bar{J}_{p,tot} = \bar{J}_p^\dagger + \bar{J}_p^\ddagger$. It is also known that the total current density driven by the excitation dynamics in each electrode is proportional to the applied current density as $\bar{J}_n^\dagger = \frac{J_{app}}{a_n L l_n}$, and $\bar{J}_p^\dagger = -\frac{J_{app}}{a_p L l_p}$. For the conservation of charge to hold in the cell, the total charge flux in the cell must be zero, namely, $\bar{J}_{n,tot} l_n + \bar{J}_{p,tot} l_p = 0$. This implies that at the leading order the current densities corresponding to the relaxation dynamics for the positive and negative electrodes should be related as $\bar{J}_p^\ddagger = -\frac{l_n}{l_p} \bar{J}_n^\ddagger$ and, in the first order approximation, as $\bar{J}_{sr,1} = -\bar{J}_{int,1}$. With this definition of relaxation dynamics for negative and positive electrodes interfacial current density, the total charge in the cell is conserved. We note that the terms representing the first-order approximation in the negative electrode serve as a correction to the intercalation process occurring at the leading-order.

Transport of Lithium in Particles. We now perform asymptotic analysis and averaging on the microscale equations describing the evolution of concentration of intercalated Li in electrode particles. Introducing the ansatz for the asymptotic expansion in (1c) and using the boundary conditions in (2a) and (2b), followed by averaging over the spherical domain, gives at the leading-order (note the boundary condition at $r_n = 1$)

$$\int_0^{r_n} \mathcal{K}_n \frac{\partial C_{n,0}}{\partial t} r^2 dr = \int_0^{r_n} \frac{1}{r^2} \frac{\partial}{\partial r} \left(r^2 D_{n0} \frac{\partial C_{n,0}}{\partial r} \right) r^2 dr, \quad t \geq 0, \quad (\text{C.13})$$

with the boundary relations

$$\begin{aligned} \frac{\partial C_{n,0}}{\partial r} &= 0, & \text{at } r = 0, \\ -D_{n0} \frac{\partial C_{n,0}}{\partial r} &= \mathcal{K}_n \gamma_n J_{n,int,0}, & \text{at } r = r_n. \end{aligned} \quad (\text{C.14})$$

Applying the fundamental theorem of calculus, the average rate of growth of concentration is obtained at the leading-order as the net flux out of the boundary, hence

$$\frac{d\bar{C}_{n,0}}{dt} = \frac{\gamma_n}{r_n} \bar{J}_{n,int,0} = \frac{\gamma_n}{r_n} (\bar{J}_n^\dagger + \bar{J}_n^\ddagger) = \frac{\gamma_n}{r_n} \left(\frac{J_{app}}{a_n L l_n} + \bar{J}_n^\ddagger \right), \quad \text{where } \bar{C}_{n,0} = \int_0^{r_n} C_{n,0} r^2 dr. \quad (\text{C.15})$$

On the other hand, at the first-order approximation we also get

$$\int_0^{r_n} \mathcal{K}_n \frac{\partial C_{n,1}}{\partial t} r^2 dr = \int_0^{r_n} \frac{1}{r^2} \frac{\partial}{\partial r} \left(r^2 D_n \Big|_{C_{n,0}} \frac{\partial C_{n,1}}{\partial r} + r^2 D'_n \Big|_{C_{n,0}} C_{n,1} \frac{\partial C_{n,0}}{\partial r} \right) r^2 dr, \quad t \geq 0, \quad (\text{C.16})$$

with the boundary relations

$$\begin{aligned} \frac{\partial C_{n,1}}{\partial r} &= 0, & \text{at } r = 0, \\ \mathcal{K}_n \gamma_n J_{int,1} &= - \left(r^2 D_n \Big|_{C_{n,0}} \frac{\partial C_{n,1}}{\partial r} + r^2 D'_n \Big|_{C_{n,0}} C_{n,1} \frac{\partial C_{n,0}}{\partial r} \right), & \text{at } r = r_n. \end{aligned} \quad (\text{C.17})$$

Note that the boundary condition on the interface of the electrode particle is computed using $J_{int,1}$. Applying the boundary conditions, the fundamental theorem of calculus and knowing that $J_{int,1} = -J_{sr,0}$, we obtain

$$\frac{d\bar{C}_{n,1}}{dt} = \frac{\gamma_n}{r_n} \bar{J}_{int,1} = - \frac{\gamma_n}{r_n} \bar{J}_{sr,0}, \quad \text{where } \bar{C}_{n,1} = \int_0^{r_n} C_{n,1} r^2 dr. \quad (\text{C.18})$$

Noting that $\bar{C}_n \approx \bar{C}_{n,0} + \lambda^{-1} \bar{C}_{n,1}$, the growth rate of Li concentration in the negative electrode is governed by

$$\frac{d\bar{C}_n}{dt} = \frac{\gamma_n}{r_n} \left(\frac{J_{app}}{a_n L l_n} + \bar{J}_n^\ddagger - \lambda^{-1} \bar{J}_{sr,0} \right), \quad (\text{C.19})$$

where the expression for $\bar{J}_{sr,0}$ is computed in (C.12).

A similar analysis can be performed for the positive particle. Introducing the ansatz for the asymptotic expansion in (1f) and using the boundary conditions (2c) and (2d), followed by averaging over the spherical domain gives at the leading-order

$$\frac{d\bar{C}_{p0}}{dt} = \frac{\gamma_p}{r_p} \bar{J}_{p,int,0} = \frac{\gamma_p}{r_p} (\bar{J}_p^\dagger + \bar{J}_p^\ddagger), \quad \text{where } \bar{C}_{p0} = \int_0^{r_p} C_{p0} r^2 dr. \quad (\text{C.20})$$

Conservation of Lithium. As the total inventory of Lithium in the cell is conserved, Li assumed to occur in four different phases (anode intercalation, anode side reaction, electrolyte, and cathode solid phase) such that the corresponding rates of change should add up to zero, namely,

$$l_n \frac{d}{dt} \bar{C}_n(t) + l_n \frac{d}{dt} \bar{C}_{sr}(t) + l \frac{d}{dt} \bar{C}_e(t) + l_p \frac{d}{dt} \bar{C}_p(t) = 0. \quad (\text{C.21})$$

This normalization condition must be satisfied by the system of equations we aim to derive. However, the computation of $\bar{C}_e(t)$ necessitates information about the concentration gradient at the boundary (after asymptotic reduction and averaging of (1g)), which is absent in the time-dependent model. Also, the amount of Lithium in the electrolyte is always conserved as noted by Planella and Widanage (2023), meaning that $\frac{d}{dt}\bar{C}_e(t) = 0$. This implies that the Li ions will enter the electrolyte at the same rate that they exit the electrolyte phase in different domains of the cell. Referring to (C.19) and (C.20), we conclude that the side reaction dynamic becomes

$$\frac{d\bar{C}_{sr,1}}{dt} = \frac{\gamma_n}{r_n} \bar{J}_{sr,0} \quad (\text{C.22})$$

in order to retain the Li conservation in the cell. The resulting simplified model is given in (3).

Appendix D. Adjoint Sensitivities in Relaxation Dynamics

In order to compute components of the gradient vector in (11), adjoint sensitivity analysis is employed (Bukshynov and Protas, 2013; Bukshynov et al., 2011; Protas et al., 2014). We begin by determining the directional derivative of the objective functional

$$\begin{aligned} \mathcal{J}'_1(\boldsymbol{\beta}; \beta'_i) &= \lim_{\epsilon \rightarrow 0} \epsilon^{-1} [\mathcal{J}_1(\boldsymbol{\beta}; \beta_i + \epsilon \beta'_i) - \mathcal{J}_1(\boldsymbol{\beta})] = \int_0^T (\mathbf{w} \mathbf{r}(t; \boldsymbol{\beta}))^\top \mathbf{C}'(\beta'_i) dt, \\ \mathbf{C}'(\beta'_i) &= \begin{bmatrix} C'_1(\boldsymbol{\beta}; \beta'_i) \\ C'_2(\boldsymbol{\beta}; \beta'_i) \end{bmatrix}, \quad \mathbf{w} = \begin{bmatrix} 1 & 0 \\ 0 & w \end{bmatrix}, \end{aligned} \quad (\text{D.1})$$

where $i \in \{1, 2, 3, 4\}$, and $\mathbf{C}'(\beta'_i)$ is the solution of a system of linear equations describing the evolution of perturbations to the state variables resulting from perturbations of each of the parameters. In order to derive this system, the parameters are perturbed, and the state variables are perturbed with respect to each of the parameters in $\boldsymbol{\beta}$ as

$$\beta_i = \hat{\beta}_i + \epsilon \beta'_i, \quad \mathbf{C}(\boldsymbol{\beta}) = \hat{\mathbf{C}}(\hat{\boldsymbol{\beta}}) + \epsilon \mathbf{C}'(\boldsymbol{\beta}; \beta'_i) + \mathcal{O}(\epsilon^2), \quad i \in \{1, 2, 3, 4\}, \quad (\text{D.2})$$

where hats represent the unperturbed variables and primes denote the perturbation. Substituting (D.2) into the system of equations (7) and collecting terms corresponding to different powers of ϵ , at the leading-order $\mathcal{O}(\epsilon^0)$ the original system of unperturbed equations $d\hat{\mathbf{C}}/dt = \hat{\mathbf{B}} + \hat{\mathbf{A}}\hat{\mathbf{C}}$ is recovered. At the first order $\mathcal{O}(\epsilon^1)$, four systems of equations are obtained each corresponding to the perturbation of one of the parameters in the vector $\boldsymbol{\beta}$, namely,

$$\begin{aligned} \frac{d}{dt} \mathbf{C}'(\beta'_i) &= \hat{\mathbf{A}} \mathbf{C}'(\beta'_i) + \mathbf{I}_i \beta'_i \hat{\mathbf{C}} + z_i \mathbf{I}_0, \\ \mathbf{I}_0 &= \begin{bmatrix} 1 \\ 0 \end{bmatrix}, \quad \mathbf{I}_1 = \begin{bmatrix} 0 & 0 \\ 0 & 0 \end{bmatrix}, \quad \mathbf{I}_2 = \begin{bmatrix} 1 & 0 \\ 0 & 0 \end{bmatrix}, \quad \mathbf{I}_3 = \begin{bmatrix} 0 & \lambda^{-1} \\ 0 & -1 \end{bmatrix}, \quad \mathbf{I}_4 = \begin{bmatrix} 0 & 0 \\ 1 & 0 \end{bmatrix}, \end{aligned} \quad (\text{D.3})$$

where $i \in \{1, 2, 3, 4\}$, $z_i = \beta'_i$, and $z_j = 0$ for $j \neq i$. Dotting these equations with the vectors of the adjoint variables $\mathbf{C}_i^*(t) = [C_1^*(t), C_2^*(t)]^\top$, and integrating with respect to time we obtain

$$\int_0^T \mathbf{C}_i^{*\top} \frac{d}{dt} \mathbf{C}'(\beta'_i) dt - \int_0^T \mathbf{C}_i^{*\top} \hat{\mathbf{A}} \mathbf{C}'(\beta'_i) dt - \int_0^T \mathbf{C}_i^{*\top} \mathbf{I}_i \beta'_i \hat{\mathbf{C}} dt - \int_0^T \mathbf{C}_i^{*\top} z_i \mathbf{I}_0 dt = 0. \quad (\text{D.4})$$

Note that four different adjoint vectors are required, each corresponding to one system in (D.3). Performing integration by parts on the first term, and applying initial conditions, we get

$$\begin{aligned} -\mathbf{C}_i^{*\top}(T)\mathbf{C}'(\beta'_i)(T) + \int_0^T \frac{d}{dt} \mathbf{C}_i^{*\top} \mathbf{C}'(\beta'_i) dt + \int_0^T \mathbf{C}_i^{*\top} \widehat{\mathbf{A}} \mathbf{C}'(\beta'_i) dt + \\ \int_0^T \mathbf{C}_i^{*\top} \mathbf{I}_i \beta'_i \widehat{\mathbf{C}} dt + \int_0^T \mathbf{C}_i^{*\top} z_i \mathbf{I}_0 dt = 0. \end{aligned} \quad (\text{D.5})$$

Factoring out \mathbf{C}' then results in

$$-\mathbf{C}_i^{*\top}(T)\mathbf{C}'(\beta'_i)(T) + \int_0^T \left[\frac{d}{dt} \mathbf{C}_i^{*\top} + \mathbf{C}_i^{*\top} \widehat{\mathbf{A}} \right] \mathbf{C}'(\beta'_i) dt = - \int_0^T \mathbf{C}_i^{*\top} \mathbf{I}_i \beta'_i \widehat{\mathbf{C}} dt - \int_0^T \mathbf{C}_i^{*\top} z_i \mathbf{I}_0 dt. \quad (\text{D.6})$$

Thus, we define the adjoint system in a judicious manner to provide a convenient expression for the directional derivative as

$$\begin{aligned} \frac{d}{dt} \mathbf{C}^{*\top} + \mathbf{C}^{*\top} \widehat{\mathbf{A}} &= (\mathbf{w} \mathbf{r}(t; \boldsymbol{\beta}))^\top, \\ \mathbf{C}^*(T) &= \mathbf{0}. \end{aligned} \quad (\text{D.7})$$

The adjoint systems defined for each vector $\mathbf{C}_i^*, i \in \{1, 2, 3, 4\}$, are in fact identical and hence the subscript i is removed. Consequently, with this definition, (D.6) reduces to

$$\mathcal{J}'_1(\boldsymbol{\beta}; \beta'_i) = - \int_0^T \mathbf{C}^{*\top} \mathbf{I}_i \beta'_i \widehat{\mathbf{C}} dt - \int_0^T \mathbf{C}^{*\top} z_i \mathbf{I}_0 dt. \quad (\text{D.8})$$

Noting that the directional derivative can be expressed as $\mathcal{J}'_1(\boldsymbol{\beta}; \beta'_i) = \partial \mathcal{J}_1 / \partial \beta_i \cdot \beta'_i$, the gradient of cost functional is finally obtained as

$$\nabla_{\boldsymbol{\beta}} \mathcal{J}_1 = \left[- \int_0^T \mathbf{C}^{*\top} \mathbf{I}_0 dt \quad - \int_0^T \mathbf{C}^{*\top} \mathbf{I}_2 \widehat{\mathbf{C}} dt \quad - \int_0^T \mathbf{C}^{*\top} \mathbf{I}_3 \widehat{\mathbf{C}} dt \quad - \int_0^T \mathbf{C}^{*\top} \mathbf{I}_4 \widehat{\mathbf{C}} dt \right]. \quad (\text{D.9})$$

Evaluation of the gradient thus requires solution of a single adjoint system (D.7). It is therefore both more efficient and accurate than numerical differentiation using finite differences. We add that adjoint system (D.7) is a terminal-value problem and needs to be integrated backwards in time.

Appendix E. Validation of the Computational Framework

Appendix E.1. Validation of Gradients

The construction of the L^2 and H^1 gradients of the constitutive relations is illustrated in Figure E.11 where, to fix attention, we focus on the the first iteration of Algorithm 1, with $\omega_1^{(0)} = \omega_2^{(0)} = 0.7$ and $\alpha^{(0)} = 3$ used as the initial guess and the \mathcal{L} interval discretized with $N = 5000$ grid points. In this experiment we set $\boldsymbol{\beta} = [-0.1, -0.1, -0.1, -0.1]$. As it can be observed in Figure E.11, the L^2 gradients are discontinuous and vanish outside the identifiability interval (the discontinuity occurs on the boundary of this region). On the other hand, the H^1 Sobolev gradients behave well outside the identifiability interval where their behavior is determined by the choice of the boundary conditions in (36) and (37), whereas their smoothness is controlled by the parameter l in the definition of the H^1 inner product (33). A Neumann boundary condition and a smoothing parameter of $l = 1$ is used for this experiment.

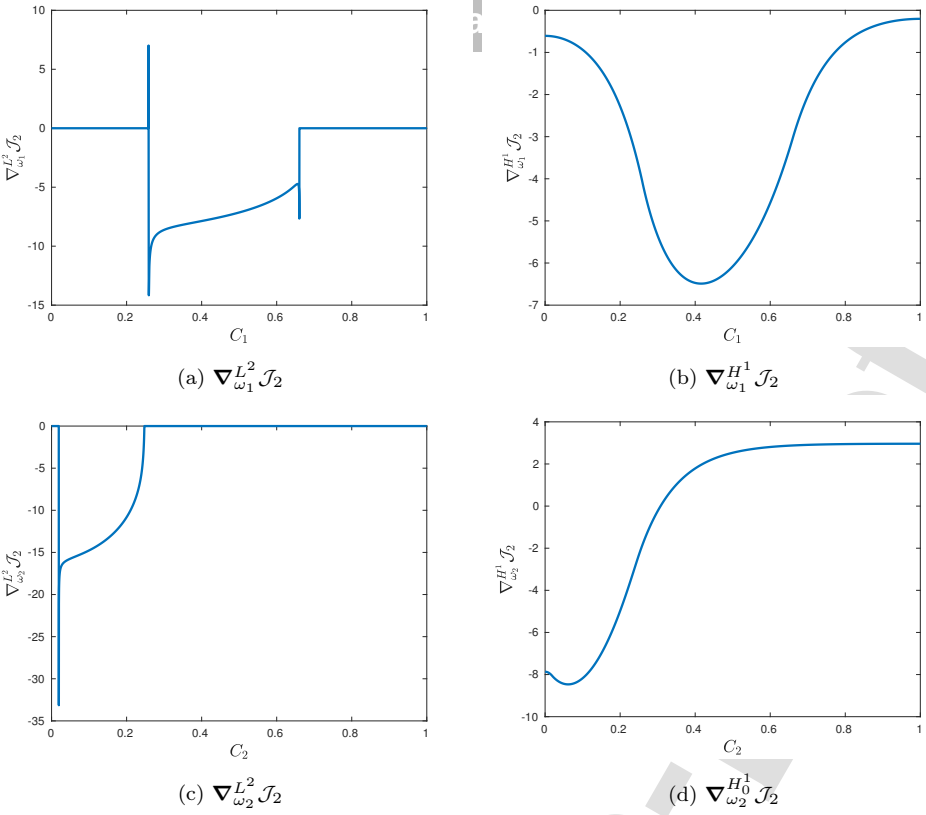


Figure E.11: $\nabla_{\omega_1}^{L^2} \mathcal{J}_2$ (a), $\nabla_{\omega_2}^{L^2} \mathcal{J}_2$ (c), $\nabla_{\omega_1}^{H^1} \mathcal{J}_2$ (b), and $\nabla_{\omega_2}^{H^1} \mathcal{J}_2$ (d) at the first iteration of Algorithm 1. Note the mean of the gradient in (d), as it is reconstructed in H_0^1 space.

To validate the derivation and computation of the gradients obtained using adjoint analysis, we will compare the expression for the Gateaux differential (22) and (32) deduced in this way with finite-difference approximations of the differentials. We thus define ratios of these quantities as

$$\begin{aligned}\kappa_1(\epsilon) &= \frac{\epsilon^{-1} [\mathcal{J}_2(\alpha, \omega_1 + \epsilon \omega'_1, \omega_2) - \mathcal{J}_2(\alpha, \omega_1, \omega_2)]}{\int_{C_1^\alpha}^{C_1^\beta} \nabla_{\omega_1}^{L^2} \mathcal{J}_2 \cdot \omega'_1 ds}, \\ \kappa_2(\epsilon) &= \frac{\epsilon^{-1} [\mathcal{J}_2(\alpha, \omega_1, \omega_2 + \epsilon \omega'_2) - \mathcal{J}_2(\alpha, \omega_1, \omega_2)]}{\int_{C_2^\alpha}^{C_2^\beta} \nabla_{\omega_2}^{L^2} \mathcal{J}_2 \cdot \omega'_2 ds}, \\ \kappa_3(\epsilon) &= \frac{\epsilon^{-1} [\mathcal{J}_2(\alpha + \epsilon \alpha', \omega_1, \omega_2) - \mathcal{J}_2(\alpha, \omega_1, \omega_2)]}{\frac{\partial \mathcal{J}_2}{\partial \alpha} \cdot \alpha'}.\end{aligned}\quad (\text{E.1})$$

We note that in the light of the Riesz identity (21) either functional space, L^2 or H^1 , could be used to evaluate the expressions in the denominator and for simplicity we choose the L^2 space here. When the gradients are approximated correctly, the quantities κ_1 , κ_2 and κ_3 should be close to unity for a broad range of ϵ values. However, these quantities deviate from the unity for very small or very large values of ϵ due to round-off and truncation errors in finite differencing, respectively, which are well-understood effects.

The dependence of $\log_{10} |\kappa_i(\epsilon) - 1|$, $i = 1, 2, 3$, on ϵ is shown in Figure E.12, where two different discretization of the interval \mathcal{L} are used when evaluating $\kappa_i(\epsilon)$. We see that, as expected, when the discretization N of the state interval \mathcal{L} is refined, the quantities $\kappa_1(\epsilon)$ and $\kappa_2(\epsilon)$ approach unity for a broad range of values of epsilon ϵ . This trend is absent from Figure E.12c, since approximation of the derivative (32) does not depend on the discretization of the interval \mathcal{L} .

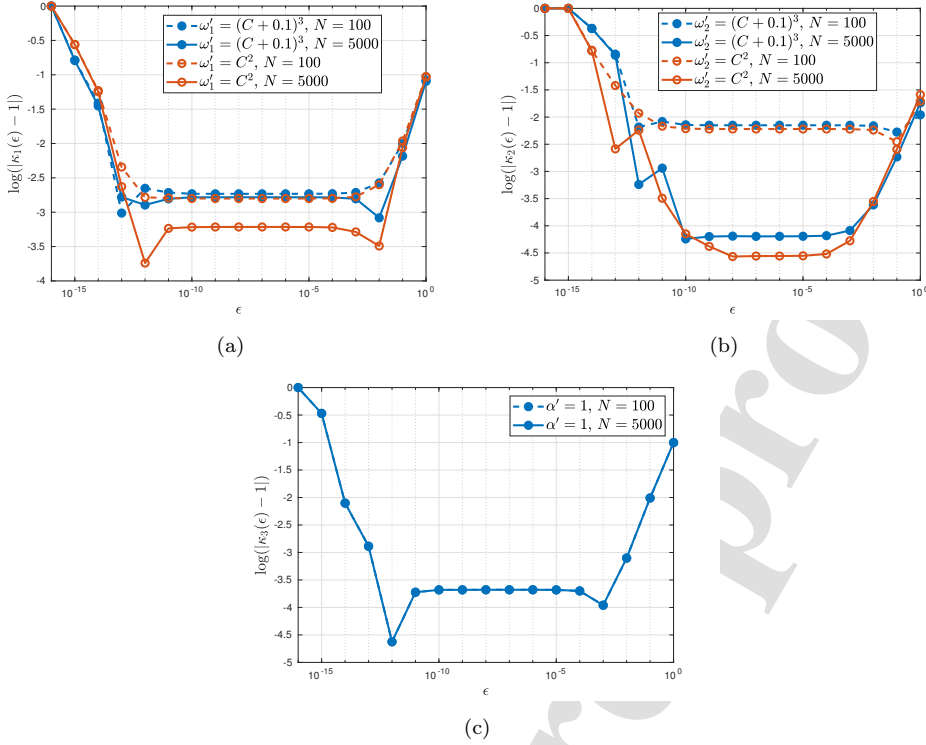


Figure E.12: The behavior of $\kappa_1(\epsilon)$ (a), $\kappa_2(\epsilon)$ (b), and $\kappa_3(\epsilon)$ (c), over a wide range of ϵ values, by using $\omega_1^{(0)} = \omega_2^{(0)} = 0.7$, $\alpha^{(0)} = 3$ as the starting point, and using different perturbations of constitutive relations and parameters. Two different discretizations of the interval \mathcal{L} are used, namely, $N = 100$ (dashed lines) and $N = 5000$ (solid lines). Note that discretization of the state interval \mathcal{L} does not affect the quantity $\kappa_3(\epsilon)$, as its partial derivative (32) is computed without discretizing the state space \mathcal{L} . Note that $\beta = [-0.1, -0.1, -0.1, -0.1]$ in this experiment.

Appendix E.2. Validation Based on a Manufactured Solution

In order to validate the entire computational framework, one can manufacture synthetic "experimental" data using some assumed forms of the constitutive relations and parameter values, and then seek to reconstruct them using Algorithm 1 starting from some initial guesses. By comparing the reconstructed relations to their assumed forms, this process allows for validation of the methodology and ensures its effectiveness under controlled conditions. Here we only present validation results for the adjoint analysis of the excitation dynamics (stage II of Algorithm 1) as it is computationally more complex. Analogous tests have also been performed for the relaxation dynamics, but are omitted here due to the simpler nature of the problem. Figure E.13 shows the assumed functional forms of the factors determining the constitutive relation via (12). The "true" value of the parameter was chosen as $\alpha = 5$. Based on the assumed forms of the constitutive relations in Figure E.13, the corresponding concentrations were "manufactured" by solving system (7) with some arbitrary initial conditions. These concentration profiles, shown in Figure E.14, are then used as the "true" data when solving inverse problem (14).

The results of the optimal reconstruction of the constitutive relations are presented in Figure E.13, along with their assumed "true" forms. In this test the initial guesses were chosen as $\omega_1^{(0)} = 0.4$, $\omega_2^{(0)} = 0.85$ and $\alpha^{(0)} = 10$ and Algorithm 1 was terminated when the relative decrease of the

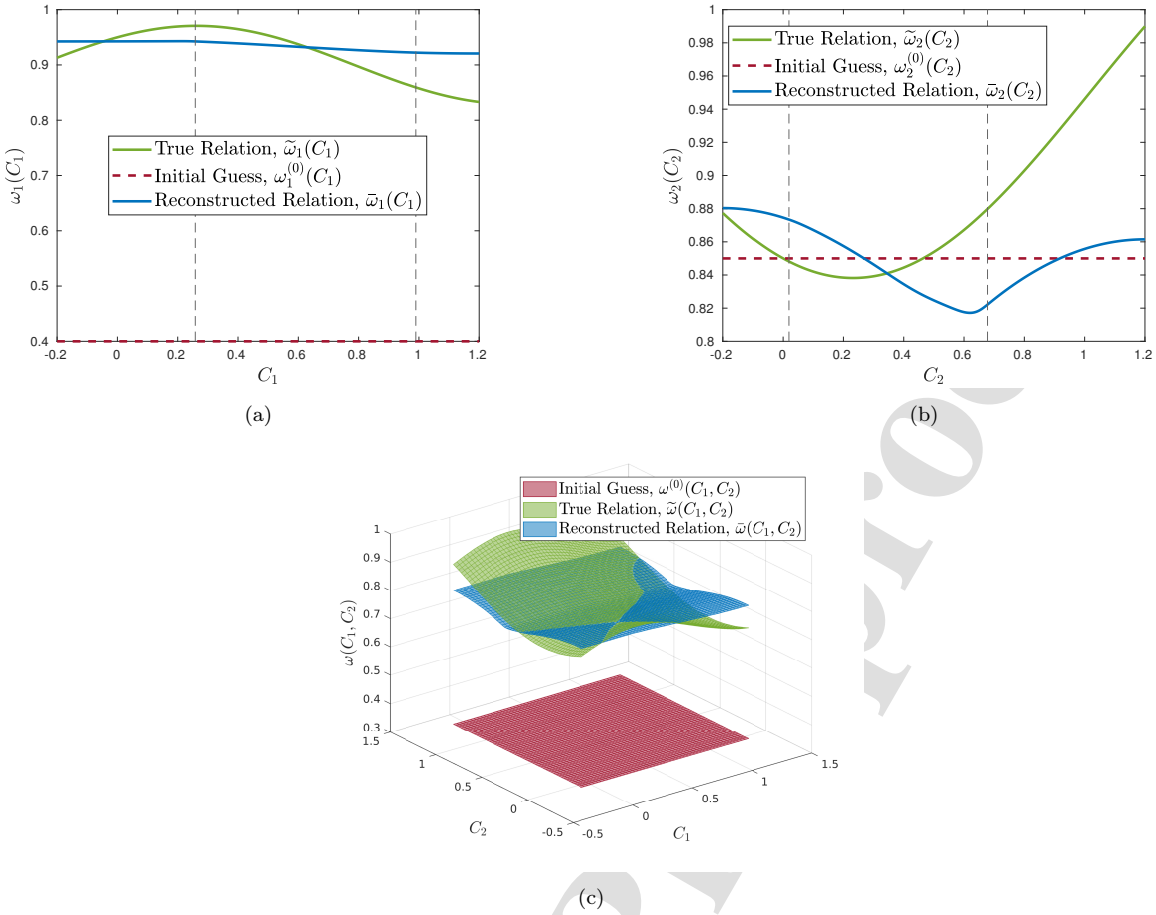


Figure E.13: Constitutive relations (a) $\omega_1(C_1)$, (b) $\omega_2(C_2)$, and (c) $\omega(C_1, C_2)$. Optimally reconstructed constitutive relations $\bar{\omega}$ (blue), along with the initial guess of relations $\omega^{(0)}$ (red) and the true relations $\tilde{\omega}$ (green) are shown. The grey vertical lines in panels (a) and (b) denote the identifiability region for the last iteration of the Algorithm 1.

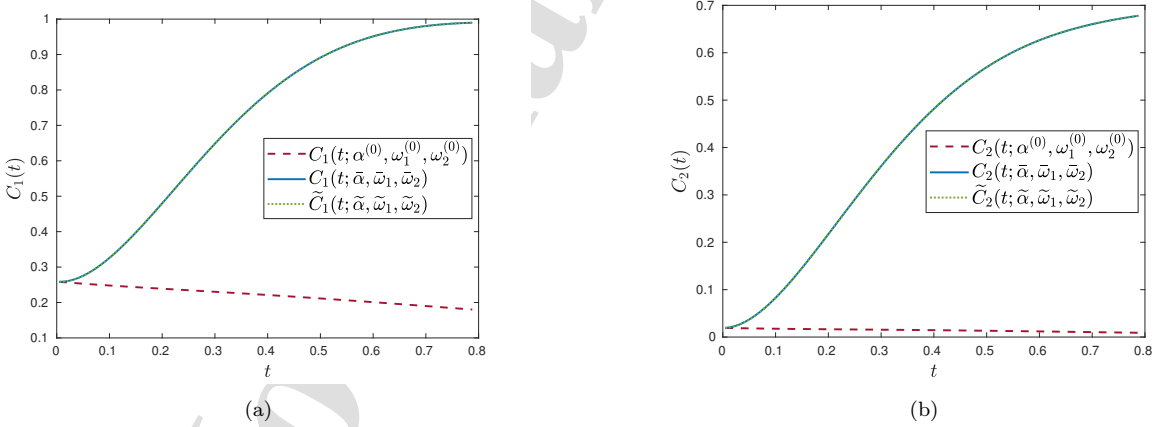


Figure E.14: Time history of concentrations $C_1(t)$ (a) and $C_2(t)$ (b) obtained using the true parameter and constitutive relations (dotted green line), the initial guess of parameter and relations (dashed red line), and the optimal reconstructed parameter and relations (solid blue line).

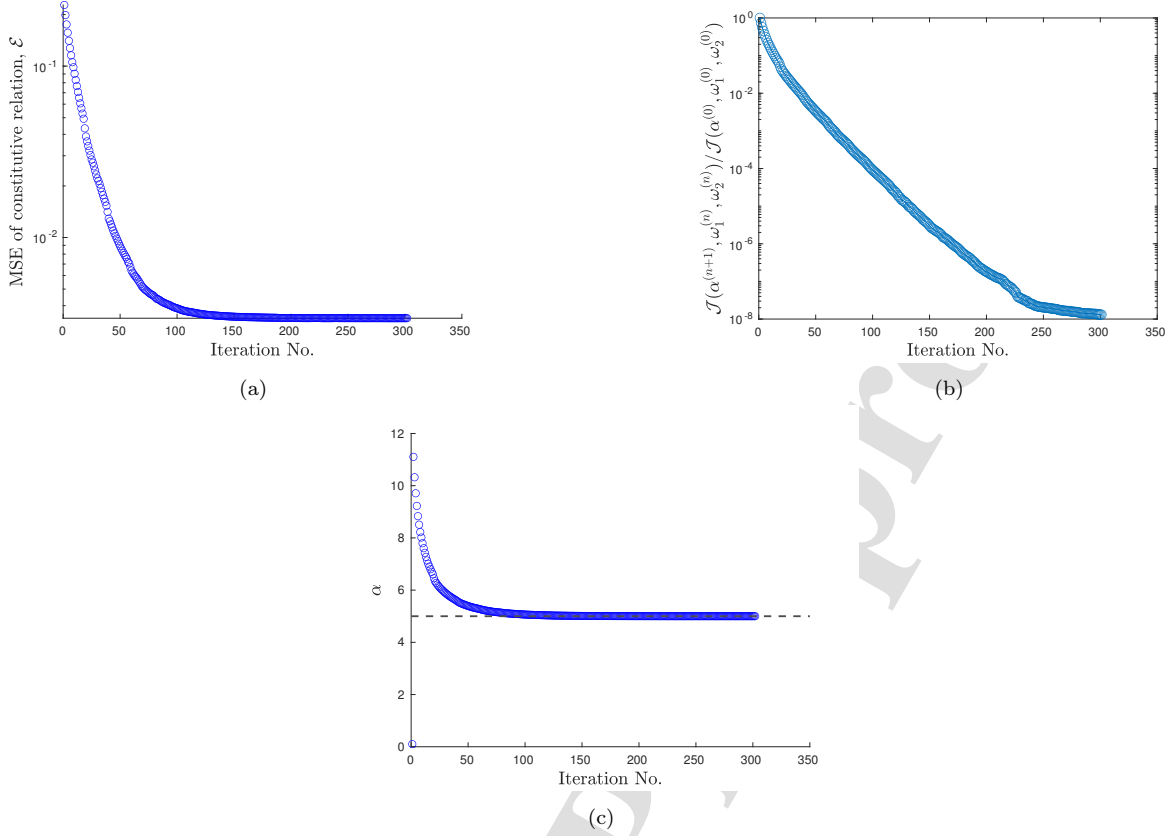


Figure E.15: Dependence on the number of iterations of (a) the mean squared error (E.2), (b) the relative decay of cost functional with respect to its initial value and (c) of the parameter α .

objective functional between two consecutive iterations became smaller than a prescribed tolerance ($TOL = 10^{-6}$) or the maximum number of iterations ($N = 300$) has been exceeded. The mean squared error between the true and reconstructed constitutive relation is defined as

$$\mathcal{E}(\omega) = \frac{1}{(C_1^b - C_1^a)(C_2^b - C_2^a)} \int_{C_1^a}^{C_1^b} \int_{C_2^a}^{C_2^b} [\omega(C_1, C_2) - \tilde{\omega}]^2 dC_2 dC_1. \quad (\text{E.2})$$

The performance of the algorithm is illustrated in Figure E.15, in which the mean squared error (E.2), the relative decay of cost functional with respect to its initial value and the evolution of the parameter α are plotted as functions of the number of iterations. As can be observed, the parameter α is approaching to its true value, $\alpha = 5$.

The time histories of the concentrations corresponding to the true constitutive relations $[\tilde{C}_1(t; \tilde{\alpha}, \tilde{\omega}_1, \tilde{\omega}_2)$ and $\tilde{C}_2(t; \tilde{\alpha}, \tilde{\omega}_1, \tilde{\omega}_2)]$, corresponding to the initial guess for the constitutive relations $[C_1(t; \alpha^{(0)}, \omega_1^{(0)}, \omega_2^{(0)})$ and $C_2(t; \alpha^{(0)}, \omega_1^{(0)}, \omega_2^{(0)})]$, and corresponding to the optimal reconstructions of the constitutive relations $[C_1(t; \bar{\alpha}, \bar{\omega}_1, \bar{\omega}_2)$ and $C_2(t; \bar{\alpha}, \bar{\omega}_1, \bar{\omega}_2)]$ are shown in Figure E.14. As can be observed, model (7) equipped with the optimally reconstructed constitutive relations and parameters can very well predict the time evolution of concentrations.

The optimal reconstruction of the constitutive relation is shown in Figure E.13 revealing some

differences with respect to its "true" form, especially, as regards the factor $\omega_2(C_2)$. There are two reasons for this. First, we note that, as is evident from Figure E.14, the time evolution of the concentrations predicted by the model with the optimally reconstructed constitutive relation $\bar{\omega}$ matches the manufactured data extremely well, demonstrating weak sensitivity of the predicted concentrations to modifications of the constitutive relation in the model (7). This is a consequence of an ill-posedness of inverse problem (14), which is a common feature of such problems (Tarantola, 2005). Second, the factors $\bar{\omega}_1(C_1)$ and $\bar{\omega}_2(C_2)$ are partially defined for concentrations C_1 and C_2 outside the identifiability interval \mathcal{I} , meaning there is no sensitivity information available for these concentration values and the Sobolev gradients are extended there by continuity only. This however should be viewed as an inherent aspect of the inverse problem considered here rather than a deficiency of the proposed solution approach.

Bibliography

- Arora, P., Doyle, M., White, R.E., 1999. Mathematical modeling of the lithium deposition overcharge reaction in lithium-ion batteries using carbon-based negative electrodes. *J. Electroch. Soc.* 146, 3543. doi:[10.1149/1.1392512](https://doi.org/10.1149/1.1392512).
- Atlung, S., West, K., Jacobsen, T., 1979. Dynamic aspects of solid solution cathodes for electrochemical power sources. *J. Electroch. Soc.* 126, 1311. doi:[10.1149/1.2129269](https://doi.org/10.1149/1.2129269).
- Bhadriraju, B., Kwon, J.S.I., Khan, F., 2023. An adaptive data-driven approach for two-timescale dynamics prediction and remaining useful life estimation of Li-ion batteries. *Comput. Chem. Eng.* 175, 108275. doi:<https://doi.org/10.1016/j.compchemeng.2023.108275>.
- Birkl, C.R., Roberts, M.R., McTurk, E., Bruce, P.G., Howey, D.A., 2017. Degradation diagnostics for lithium ion cells. *J. Power Sources* 341, 373–386. doi:<https://doi.org/10.1016/j.jpowsour.2016.12.011>.
- Bugga, R.V., Smart, M.C., 2010. Lithium plating behavior in lithium-ion cells. *ECS Trans.* 25, 241. doi:[10.1149/1.3393860](https://doi.org/10.1149/1.3393860).
- Bukshtynov, V., Protas, B., 2013. Optimal reconstruction of material properties in complex multiphysics phenomena. *J. Comput. Phys.* 242, 889 – 914. doi:<https://doi.org/10.1016/j.jcp.2013.02.034>.
- Bukshtynov, V., Volkov, O., Protas, B., 2011. On optimal reconstruction of constitutive relations. *Phys. D: Nonlinear Phenom.* 240, 1228 – 1244. doi:<https://doi.org/10.1016/j.physd.2011.04.006>.
- Daniels, L., Sahu, S., Sanders, K.J., Goward, G.R., Foster, J.M., Protas, B., 2023. Learning optimal forms of constitutive relations characterizing ion intercalation from data in mathematical models of lithium-ion batteries. *J. Phys. Chem. C* 127, 17508–17523. doi:[10.1021/acs.jpcc.3c02915](https://doi.org/10.1021/acs.jpcc.3c02915).
- Dickinson, E.J., Wain, A.J., 2020. The Butler-Volmer equation in electrochemical theory: Origins, value, and practical application. *J. Electroanal. Chem.* 872, 114145. doi:<https://doi.org/10.1016/j.jelechem.2020.114145>.
- Edge, J.S., O’Kane, S., Prosser, R., Kirkaldy, N.D., Patel, A.N., Hales, A., Ghosh, A., Ai, W., Chen, J., Yang, J., et al., 2021. Lithium ion battery degradation: what you need to know. *Phys. Chem. Chem. Phys.* 23, 8200–8221. doi:[10.1039/D1CP00359C](https://doi.org/10.1039/D1CP00359C).
- Escalante, J.M., Ko, W., Foster, J.M., Krachkovskiy, S., Goward, G., Protas, B., 2020. Discerning models of phase transformations in porous graphite electrodes: Insights from inverse modelling based on MRI measurements. *Electrochimica Acta* 349, 136290. doi:<https://doi.org/10.1016/j.electacta.2020.136290>.
- Fang, Y., Smith, A.J., Lindström, R.W., Lindbergh, G., Furó, I., 2022. Quantifying lithium lost to plating and formation of the solid-electrolyte interphase in graphite and commercial battery components. *Appl. Mater. Today* 28, 101527. doi:<https://doi.org/10.1016/j.apmt.2022.101527>.
- Fuller, T.F., Doyle, M., Newman, J., 1994. Simulation and Optimization of the Dual Lithium Ion Insertion Cell. *J. Electroch. Soc.* 141, 1–10. doi:[10.1149/1.2054684](https://doi.org/10.1149/1.2054684).
- Guo, Y., Smith, R.B., Yu, Z., Efetov, D.K., Wang, J., Kim, P., Bazant, M.Z., Brus, L.E., 2016. Li intercalation into graphite: direct optical imaging and Cahn–Hilliard reaction dynamics. *J. Phys. Chem. Lett.* 7, 2151–2156. doi:[10.1021/acs.jpcllett.6b00625](https://doi.org/10.1021/acs.jpcllett.6b00625).
- Lee, H., Sitapure, N., Hwang, S., Kwon, J.S.I., 2021. Multiscale modeling of dendrite formation in lithium-ion batteries. *Comput. Chem. Eng.* 153, 107415. doi:<https://doi.org/10.1016/j.compchemeng.2021.107415>.
- Lin, X., Khosravinia, K., Hu, X., Li, J., Lu, W., 2021. Lithium plating mechanism, detection, and mitigation in lithium-ion batteries. *Prog. Energy Combust. Sci.* 87, 100953. doi:<https://doi.org/10.1016/j.pecs.2021.100953>.

- Luenberger, D., 1969. Optimization by Vector Space Methods. John Wiley and Sons.
- Marquis, S.G., Sulzer, V., Timms, R., Please, C.P., Chapman, S.J., 2019. An asymptotic derivation of a single particle model with electrolyte. *J. Electrochem. Soc.* 166, A3693. doi:[10.1149/2.0341915jes](https://doi.org/10.1149/2.0341915jes).
- Newman, J., Balsara, N.P., 2021. Electrochemical systems. John Wiley & Sons.
- Nocedal, J., Wright, S., 2002. Numerical Optimization. Springer.
- O’Kane, S.E., Ai, W., Madabattula, G., Alonso-Alvarez, D., Timms, R., Sulzer, V., Edge, J.S., Wu, B., Offer, G.J., Marinescu, M., 2022. Lithium-ion battery degradation: how to model it. *Phys. Chem. Chem. Phys.* 24, 7909–7922. doi:[10.1039/D2CP00417H](https://doi.org/10.1039/D2CP00417H).
- Ovejas, V., Cuadras, A., 2019. Effects of cycling on lithium-ion battery hysteresis and overvoltage. *Sci. Rep.* 9, 14875. doi:<https://doi.org/10.1038/s41598-019-51474-5>.
- Paul, P.P., McShane, E.J., Colclasure, A.M., Balsara, N., Brown, D.E., Cao, C., Chen, B.R., Chinnam, P.R., Cui, Y., Dufek, E.J., et al., 2021. A Review of Existing and Emerging Methods for Lithium Detection and Characterization in Li-Ion and Li-Metal Batteries. *Adv. Energy Mater.* 11, 2100372. doi:<https://doi.org/10.1002/aenm.202100372>.
- Planella, F.B., Ai, W., Boyce, A., Ghosh, A., Korotkin, I., Sahu, S., Sulzer, V., Timms, R., Tranter, T., Zyskin, M., et al., 2022. A continuum of physics-based lithium-ion battery models reviewed. *Prog. Energy* 4, 042003. doi:[10.1088/2516-1083/ac7d31](https://doi.org/10.1088/2516-1083/ac7d31).
- Planella, F.B., Widanage, W.D., 2023. A single particle model with electrolyte and side reactions for degradation of lithium-ion batteries. *Appl. Math. Model.* 121, 586–610. doi:<https://doi.org/10.1016/j.apm.2022.12.009>.
- Prada, E., Di Domenico, D., Creff, Y., Bernard, J., Sauvant-Moynot, V., Huet, F., 2012. Simplified electrochemical and thermal model of LiFePO₄-graphite Li-ion batteries for fast charge applications. *J. Electrochem. Soc.* 159, A1508. doi:[10.1149/2.064209jes](https://doi.org/10.1149/2.064209jes).
- Press, W.H., Flanner, B.P., Teukolsky, S.A., Vetterling, W.T., 1986. Numerical Recipes: the Art of Scientific Computations. Cambridge University Press.
- Protas, B., Bewley, T.R., Hagen, G., 2004. A comprehensive framework for the regularization of adjoint analysis in multiscale PDE systems. *J. Comput. Phys.* 195, 49–89.
- Protas, B., Noack, B.R., Morzynski, M., 2014. An optimal model identification for oscillatory dynamics with a stable limit cycle. *J. Nonlinear Sci.* 24, 245–275. doi:<https://doi.org/10.1007/s00332-013-9188-z>.
- Richardson, G., Korotkin, I., Ranom, R., Castle, M., Foster, J., 2020. Generalised single particle models for high-rate operation of graded lithium-ion electrodes: Systematic derivation and validation. *Electrochimica Acta* 339, 135862. doi:<https://doi.org/10.1016/j.electacta.2020.135862>.
- Sahu, S., Foster, J.M., 2023. A continuum model for lithium plating and dendrite formation in lithium-ion batteries: Formulation and validation against experiment. *J. Energy Storage* 60, 106516. doi:<https://doi.org/10.1016/j.est.2022.106516>.
- Sanders, K.J., Ciezki, A.A., Berno, A., Halalay, I.C., Goward, G.R., 2023. Quantitative Operando ⁷Li NMR Investigations of Silicon Anode Evolution during Fast Charging and Extended Cycling. *J. Am. Chem. Soc.* 145, 21502–21513. doi:[10.1021/jacs.3c07339](https://doi.org/10.1021/jacs.3c07339).
- Santhanagopalan, S., Ramadass, P., Zhang, J.Z., 2009. Analysis of internal short-circuit in a lithium ion cell. *J. Power Sources* 194, 550–557. doi:<https://doi.org/10.1016/j.jpowsour.2009.05.002>.
- Sethurajan, A.K., Foster, J.M., Richardson, G., Krachkovskiy, S.A., Bazak, J.D., Goward, G.R., Protas, B., 2019. Incorporating Dendrite Growth into Continuum Models of Electrolytes: Insights from NMR Measurements and Inverse Modeling. *J. Electrochem. Soc.* 166, A1591–A1602. doi:[10.1149/2.0921908jes](https://doi.org/10.1149/2.0921908jes).
- Sethurajan, A.K., Krachkovskiy, S.A., Halalay, I.C., Goward, G.R., Protas, B., 2015. Accurate characterization of ion transport properties in binary symmetric electrolytes using in situ NMR imaging and inverse modeling. *J. Phys. Chem. B* 119, 12238–12248. doi:[10.1021/acs.jpcb.5b04300](https://doi.org/10.1021/acs.jpcb.5b04300).
- Suresh, R., Rengaswamy, R., 2018. Modeling and control of battery systems. Part I: Revisiting Butler–Volmer equations to model non-linear coupling of various capacity fade mechanisms. *Comput. Chem. Eng.* 119, 336–351. doi:<https://doi.org/10.1016/j.compchemeng.2018.08.016>.
- Tarantola, A., 2005. Inverse Problem Theory and Methods for Model Parameter Estimation. SIAM.
- Tian, Y., Lin, C., Li, H., Du, J., Xiong, R., 2021. Detecting undesired lithium plating on anodes for lithium-ion batteries—a review on the in-situ methods. *Appl. Energy* 300, 117386. doi:<https://doi.org/10.1016/j.apenergy.2021.117386>.
- Yang, X.G., Ge, S., Liu, T., Leng, Y., Wang, C.Y., 2018. A look into the voltage plateau signal for detection and quantification of lithium plating in lithium-ion cells. *J. Power Sources* 395, 251–261. doi:<https://doi.org/10.1016/j.jpowsour.2018.05.073>.
- Zhang, G., Wei, X., Chen, S., Han, G., Zhu, J., Dai, H., 2022. Investigation the degradation mechanisms of lithium-

ion batteries under low-temperature high-rate cycling. ACS Appl. Energy Mater. 5, 6462–6471. doi:[10.1021/acsaem.2c00957](https://doi.org/10.1021/acsaem.2c00957).

Journal Pre-proof

Conflict of Interest

The authors have declared no conflict of interest

Corresponding author

Conflict of Interest

The authors have declared no conflict of interest

Corresponding author